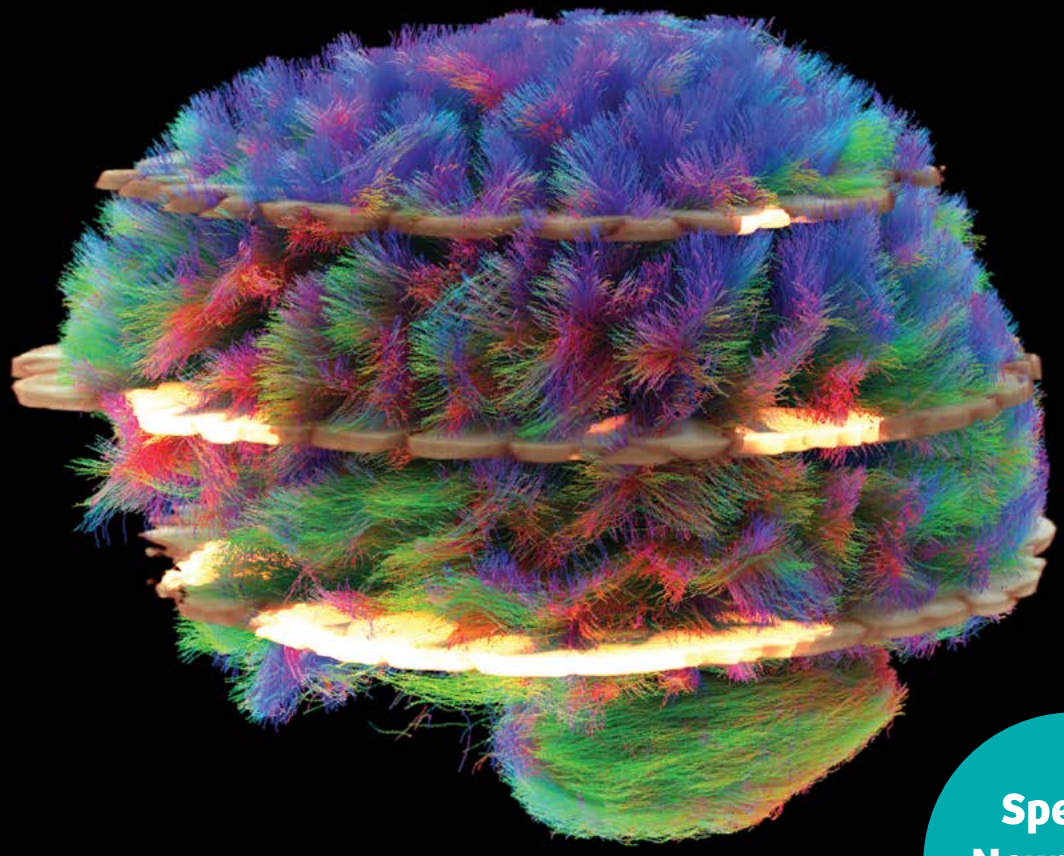

Special Neurology Edition

MAGNETOM Flash

The Magazine of MRI

usa.siemens.com/magnetom-world

SIEMENS Healthineers

Neuroradiologists remain the largest users of MRI based on volume. The prevalence and volume of scans, coupled with our changing healthcare landscape, are driving new requirements for higher efficiency and effectiveness. At the same time, aging populations and elusive disorders require innovations that could lead to better, more nimble patient care pathways. This special Neurology edition of the MAGNETOM Flash magazine comprises some of the most relevant articles for neuroradiology practices in the United States, covering topics from greater efficiency in everyday clinical practice to entirely new approaches to MRI.

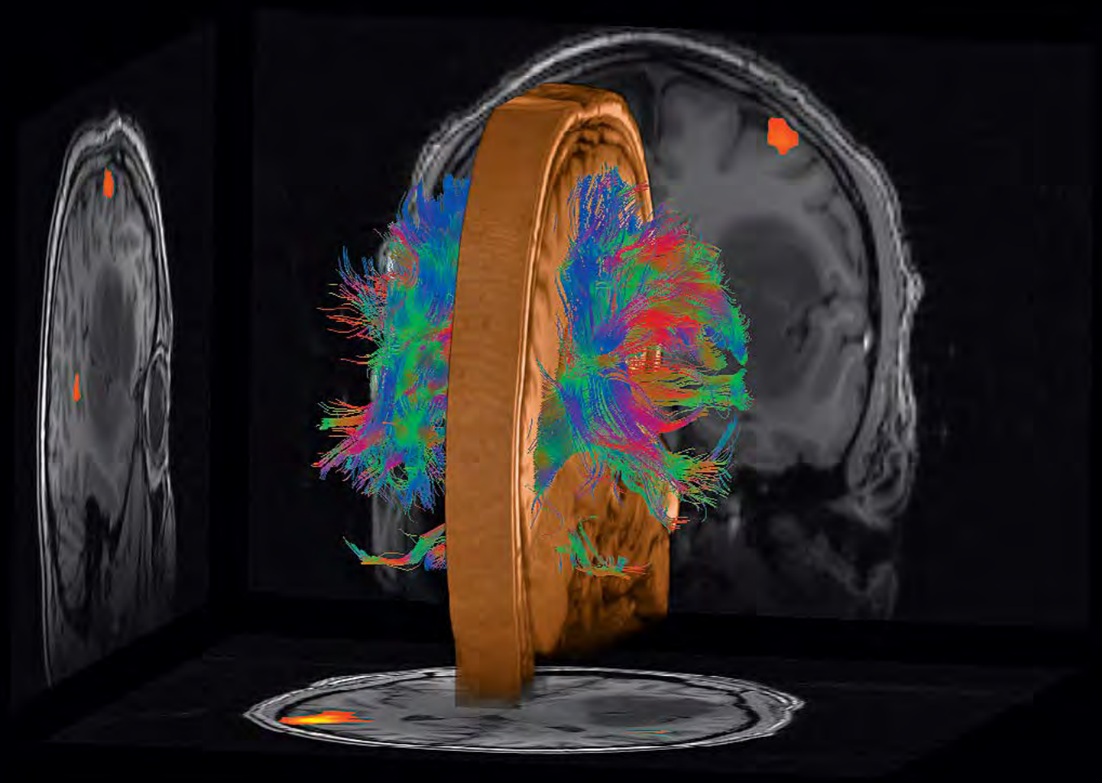

Additional Resources

Webinars: Industry experts discuss the latest trends and innovations in MRI.
usa.siemens.com/mr-webinars

Case Studies: Customers share how our MRI solutions support their success.
usa.siemens.com/mr-casestudies

Editorial Board

We appreciate your comments.
Please contact us at magnetomworld.med@siemens-healthineers.com

Review Board

Contents

Contents

GOBrain

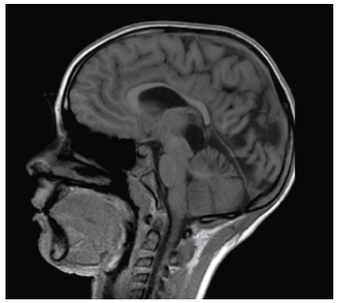

FREEZEit

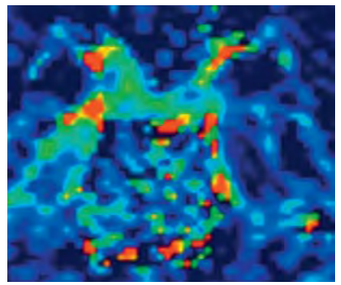

BOLD fMRI

syngo Neuro 3D

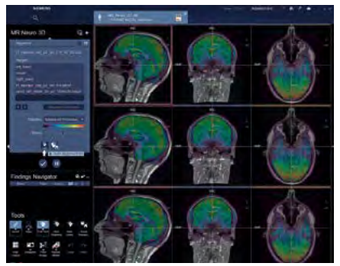

RESOLVE

Simultaneous Multi-Slice

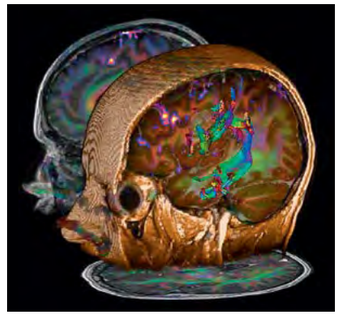

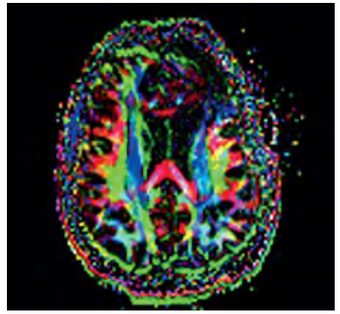

Fingerprinting

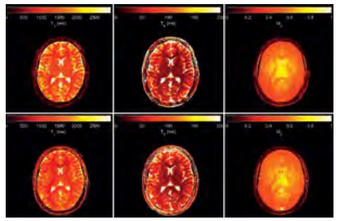

New Strategies for Protocol Optimization for Clinical MRI: Rapid Examinations and Improved Patient Care

Otto Rapalino, M.D.[1]; Keith Heberlein, Ph.D.[2]
[1]Neuroradiology Division, Department of Radiology, Massachusetts General Hospital, Boston, MA, USA
[2]Director of Neuro Applications Development, Siemens Healthcare USA

Heightened attention to healthcare costs and value based outcomes in medicine are driving revolutionary changes in the MR industry. The MR community of academics, clinicians and industry experts need to build cooperative programs to dispel the old perceptions of MR as a slow and overly expensive imaging modality. Cooperative changes can be implemented on two fronts through utilization of advanced technology, revised reading procedures, and a culture change around the standard operations of MR. Siemens MR, in cooperation with Massachusetts General Hospital (MGH) in Boston, are building such a program with the first results now being made available with the recent launch of GOBrain, a new application which enables a push-button diagnostic brain examination in 5 minutes. This article will detail the strategic approach behind the implementation of GOBrain and then discuss briefly future potential extensions to GO (Generalized Optimized) strategies to develop fast and clinically validated examinations in MR.

GOBrain is a clinically validated diagnostic brain exam which takes 5 minutes[1]. It consists of five diagnostically-important MR brain protocols [1, 2] acquired with optimized pulse sequences. Integrated with individual anatomical landmark-based AutoAlign technology providing automatic slice positioning, this push-button exam requires minimal interaction from the technologist. The included sequences are a sagittal T1-weighted, axial T2-weighted, axial T2-weighted DarkFluid, axial diffusion-weighted and an axial T2*-weighted contrast. Within the allotted five minutes for the complete exam, contrasts with stronger diagnostic utility were prioritized and afforded longer acquisition times, with the decided order of prioritization set as the DarkFluid, T2 -weighted, diffusion, T1-weighted and the T2*-weighted contrasts. The axial views cover the same field-of-view (FOV) and are acquired with identical slice thickness in order to read out multiple contrasts with synchronized display protocols (Fig. 1).

MR technologies which enabled the realization of GOBrain include parallel imaging [3] with high channel density coils [4, 5] and 3 Tesla imaging. The original expectation was that rapid exams could only be facilitated by higher field strength and high channel systems. However, during the course of the development effort, it became clear that the methodical approach towards a GO protocol optimization could also impact 1.5 Tesla systems and lower channel count head coils with some modest increase in total scan time (see Appendix for the protocols across 1.5T and 3T systems). A key driving principle behind GOBrain was to preserve the image impressions in terms of contrast and resolution for radiological reading of routine MR exams and, at the same time, finding signal-to-noise ratio (SNR) limits acceptable for diagnostic imaging. A salient correlation can be made to the recent drive towards dose reduction in computed tomography (CT). With innovative developments in CT on the technology side, (e.g. dual energy), low-dose CT protocols were also developed for targeted applications where the diagnostic quality of the images is tuned to the application. Borrowing a similar approach and strategy in MR leads to a reframing of the protocol development goal towards a scan session which is as fast as reasonably achievable while maintaining at least the same diagnostic value.

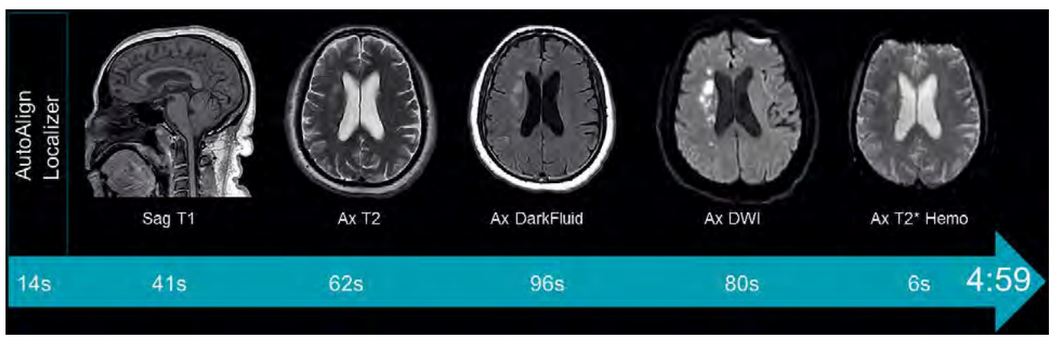

1 A schematic illustration of GOBrain with the corresponding image labels and scan times. Images acquired on a MAGNETOM Skyra 3T with the Head 32 coil.

A key step in the development of GOBrain was to establish the diagnostic equivalence of a rapid MR approach versus conventional examinations. The validation approach required two board-certified radiologists to perform double blind reads of clinical neuro exams and to score the images with regard to contrast, SNR and artifacts in 6 patient exams. To control for motion behavior in patients, the five-minute exam was placed randomly either prior to the conventional exam or after in order to average out any effects related to the order of acquisition. Additionally, both the rapid and conventional exams were read with clinical findings reported. The principle findings of the study (submitted to a peer reviewed journal for publication) [2] were that the rapid exam was

1) less prone to motion artifacts

2) of sufficient quality to make the diagnosis and

3) made no difference in the final radiological diagnosis.

These findings led to the primary conclusion that this fast examination may replace the conventional protocol, especially in motion-prone inpatient settings.

Adoption of rapid MRI protocols into the clinical service can trigger a culture change in the clinical team. Adaptations may be required to operations in terms of both workflow and training. GOBrain is a push button exam with automatic slice and orientation positioning and each sequence will run automatically one after the other. The scanner noise changes in pitch and volume during the continuously driven exam. However, if the technologists allow the scanner to run through the multiple contrasts without interaction, then the entire exam becomes a single protocol from the patient perspective. The acquisition is built with fast, individual sequences, which minimize the risk of motion artifacts. Also, if one contrast is corrupted by motion artifacts then only that single contrast needs to be reacquired. In a patient-centered approach, a rapid MR can substantially improve the patient experience at the scanner.

In the realm of personalized medicine, advanced imaging techniques will be required to address additional structural and functional markers of the disease process. The scan time requirements for acquiring enhanced imaging biomarkers need to be balanced with the increasing pressure on reducing scheduling time slots towards 30 minutes and below. A rapid MR approach for a core brain protocol opens possibilities to incorporate imaging into time-restricted scan slots. With the recent availability of Simultaneous Multi-Slice (SMS) technology [6 – 9] which can greatly accelerate diffusion and BOLD imaging, this further reduces the time required for important functional information. Other examples of GOBrain potential add-on exams are susceptibility-weighted imaging (SWI), post-contrast MPRAGE, perfusion-weighted imaging and high-resolution 3D DarkFluid. GOBrain can then be viewed as a scout exam and also function as a backup scan in cases where the high-resolution 3D protocols are corrupted by motion.

Extension of the GO protocol projects are now under consideration for other high volume MR indications. The vision is to build a comprehensive suite of fast, optimized diagnostic protocols which are clinically validated. The general structured approach for developing a GO protocol is as follows:

1) Establish the time budget for a given core exam. The scan time goal should be considered a restraint on the protocol development process and should not be revised until completion of the protocol development exercise.

2) Define the set of required contrasts for routine diagnosis and rank them in order of clinical priority based on literature evidence. Each contrast should be given an individual time budget based on their relative diagnostic importance.

3) Research the available methods for the acceleration of each sequence. Prototype and iterate on individual protocol candidates for each contrast from the protocol simulator.

4) Once candidate protocols are identified, conduct healthy volunteer scans to assess image quality in terms of tissue contrast and signal to noise levels. Several iterations may be required to finalize the protocol.

[1]Achieved on a MAGNETOM Skyra with the Head 32 coil. Total examination time can take up to 6 minutes depending on system fieldstrength and coil density.

MAGNETOM Skyra, 3T, Head/Neck 64													Total exam time: 4:36
Plane	**TR (ms)**	**TE (ms)**	**FOV (mm)**	**Phase FOV (%)**	**Slices**	**Slice (mm)**	**Gap (%)**	**Matrix**	**Phase Directions**	**iPAT factor**	**b-values**	**Directions (no)**	**TA (mins)**
AutoAlign Head Scout													
3D	3.15	1.37	260	100	128	1.6	20	160	A-P	3	NA	NA	0:14
T1 GRE FLASH													
Sag	240	2.46	220	100	35	4.0	20	256	A-P	3	NA	NA	0:34
T2 TSE													
Axial	6200	78	220	87.5	25	5.0	20	256	R-L	3	NA	NA	1:02
T2 TSE DarkFluid													
Axial	8000	114	220	87.5	25	5.0	20	256	R-L	3	NA	NA	1:20
ep2d Diffusion													
Axial	4000	65	240	100	31	5.0	12	160	A-P	3	0,800	12	1:20
ep2d T2*-weighted													
Axial	6120	30	220	100	25	5.0	20	128	A-P	1	NA	NA	0:06

MAGNETOM Skyra, 3T, Head 32													Total exam time: 4:59
Plane	**TR (ms)**	**TE (ms)**	**FOV (mm)**	**Phase FOV (%)**	**Slices**	**Slice (mm)**	**Gap (%)**	**Matrix**	**Phase Directions**	**iPAT factor**	**b-values**	**Directions (no)**	**TA (mins)**
AutoAlign Head Scout													
3D	3.15	1.37	260	100	128	1.6	20	160	A-P	3	NA	NA	0:14
T1 GRE FLASH													
Sag	240	2.46	220	100	35	4.0	20	256	A-P	2	NA	NA	0:41
T2 TSE													
Axial	6200	78	220	87.5	25	5.0	20	256	R-L	3	NA	NA	1:02
T2 TSE DarkFluid													
Axial	8000	119	220	87.5	25	5.0	20	256	R-L	2	NA	NA	1:36
ep2d Diffusion													
Axial	4000	65	240	100	31	5.0	12	160	A-P	3	0,800	12	1:20
ep2d T2*-weighted													
Axial	6120	30	220	100	25	5.0	20	128	A-P	1	NA	NA	0:06

5) Once finalized, perform head-to-head comparisons to conventional examinations in the target patient population to compare the rapid MR protocol to the conventional exam with blind reads by at least two board certified radiologists. The reports should contain a qualitative assessment of the image quality, such as contrast and presence of artifacts and diagnostic findings appropriate for the indication. Concordance between both protocols across readers then validates the clinical utility of the rapid protocol.

Appendix

The GOBrain exam consists of a localizer scout with AutoAlign functionalities and five fundamental unenhanced MRI sequences (sagittal T1-weighted, axial T2-weighted, axial DarkFluid/FLAIR, axial DWI and axial T2*-weighted MRI sequences). Depending on the field strength (1.5T and 3T) and the number of elements in the coil used for imaging, total exam time lasts between 4:36 minutes on a 3T system with the Head/Neck 64 coil to 5:56 minutes for imaging on a 1.5T system with the Head/Neck 20 coil. Protocol parameters including scan times are detailed above for each system.

References

[1]Mehan WA, Gonzales RG, Buchbinder BR, Chen JW, Copen WA, Gupta R, et al. Optimal brain MRI protocol for new neurological complaint. PLOS One 2014; 9(10): e110803. doi:10.1371/journal.pone.0110803.

[2]Prakkamakul S, Witzel T, Huang S, Boulter D, Borja MJ, Schaefer P, et al. Comparative analysis of image quality and diagnostic concordance between 5-minute and conventional magnetic resonance protocols for brain imaging. Manuscript submitted for publication 2016.

[3]Griswold MA, Jakob PM, Heidemann RM, Nittka M, Jellus V, Wang J, et al. GeneRalized Autocalibrating Partially Parallel Acqusitions (GRAPPA). Magn Reson Med 2002; 47:1202-1210.

[4]Keil B, Wald LL. Massively parallel MRI detector arrays. J Magn Reson 2013; 229: 75-89.

[5]Wiggins GC, Triantafyllou C, Potthast A, Reykowski A, Nittka M, Wald LL. 32-channel 3 Tesla receive-only phased-array head coil with soccer-ball element geometry. Magn Reson Med 2006; 56(1): 216-223.

[6]Setsompop K, Cohen-Adad J, Gagoski BA, Raij T, Yendiki A, Keil B, et al. Improving diffusion MRI using simultaneous multi-slice echo planar imaging. Neuroimage 2012; 63:569-580.

[7]Setsompop K, Cauley S, Wald L. (2015). Advancing diffusion MRI using SMS EPI. MAGNETOM Flash (Special SMS Supplement) 2015; 63:16-22.

[8]Smith SM, Beckmann CF, Andersson J, Auerbach EJ, Bijsterbosch J, Douaud G, et al. Resting state fMRI in the Human Connectome Project. Neuroimage 2013; 80:144-168.

[9]Ugurbil K, Auerbach EJ, Modeller S, Xu J, Vu A, Glasser MF, et al. Slice acceleration in the 3 Tesla component of the human connectome project. MAGNETOM Flash (Special SMS Supplement) 2015; 63:49-56.

Download the GOBrain and GOBrain+ Protocols

GOBrain+ expands GOBrain to additionally support brain imaging with contrast medium. Additional optimized sequences include an axial T1-weighted sequence administred pre- and post-contrast and a post-contrast MPRage.

Visit usa.siemens.com/gobrain-protocols to download the .exar1 files for 1.5 and 3T

Contacts
Otto Rapalino, M.D.
Phone: +1 617-726-8320

Case Series: Pediatric[1] GOBrain-5-Minute Protocol MR Imaging at 3 Tesla

Elka Miller, M.D., FRCPC[1]; Barry Smith, MRT (MR)[2]
[1]Chief and Research Director, [2]MRI Supervisor, Medical Imaging Department,
Children's Hospital of Eastern Ontario (CHEO), Ottawa, ON, Canada

Background

Fast-brain MRI was first introduced for children[1] with shunt dependent hydrocephalus[1-3] who frequently undertake serial imaging studies through life. The image studies often include a combination of both CT and MRI depending on the child's age, study time, and availability of equipment. CT scans involve exposure to radiation, which has potentially harmful effects, especially for young children[4]. The alternative to a CT scan is MRI, but brain MRI is time consuming and sensitive to motion artifacts. In young patients, MRI studies might require sedation or general anesthesia, which have their own risks of complications[5]. Therefore, fast MRI sequences can avoid the need for sedation or anesthesia, and are thus particularly useful for young and uncooperative patients. Recently, fast MRI sequences have become more popular and these are increasingly being used for non-hydrocephalic indications such as macrocephaly, intracranial cysts, screening for some structural congenital and non-congenital anomalies, and postoperative follow-up[6].

A number of 'fast MRI' protocols have been used; the most popular are modifications of T2-weighted MRI, including Half-Fourier Acquisition Single-shot Turbo Spin Echo (HASTE)[7], Single Shot Fast Spin Echo (SSFSE)[6,8], and Periodically Rotated Overlapping Parallel lines with enhanced reconstruction (PROP) FSE[2]. These protocols often use a single type of pulse sequence which carries potential pitfalls. Our previous study[9] demonstrated undetected findings in 7/50 (14%) pediatric fast brain MRI including venous sinus thrombosis (one patient), subdural hematoma (three), failure to differentiate blood products (two), and limited evaluation of extra-axial collections (one). This limitation was seen to be due to the lack of other pulse sequences to further characterize tissue and fluid. Consequently, there is a known need to improve image quality using fast MR protocols for all clinically relevant sequences; this is likely to occur when different pulse sequences and planes are used for evaluation of the brain tissues and fluids.

Table 1: Acquisition parameters and scan time for 5-minute GOBrain MRI protocols on the MAGNETOM Skyra with the Head/Neck 20 coil.

	Plane	TR (ms)	TE (ms)	FOV (mm)	Phase FOV (%)	Slices	Slice (mm)	Gap (%)	Matrix	Phase directions	iPAT factor	b-values	Directions (no)	TA (mins)
AutoAlign Head Scout	3D	3.15	1.37	260	100	128	1.6	20	160	A-P	3	NA	NA	0:14
T1 GRE FLASH	Sag	240	2.46	220	100	35	4.0	20	256	A-P	2	NA	NA	0:41
T2 TSE	Axial	6200	78	220	87.5	25	5.0	20	256	R-L	3	NA	NA	1:02
T2 TSE DarkFluid	Axial	8000	119	220	87.5	25	5.0	20	256	R-L	2	NA	NA	1:52
ep2d Diffusion	Axial	4200	72	240	100	31	5.0	12	160	A-P	2	0,800	12	1:16
ep2d T2*W	Axial	6120	30	220	100	25	5.0	20	128	A-P	1	NA	NA	0:06
													Total exam time	5:11

[1]MR scanning has not been established as safe for imaging fetuses and infants less than two years of age. The responsible physician must evaluate the benefits of the MR examination compared to those of other imaging procedures.

GOBrain[10,11] was developed as a 5-minute diagnostic brain exam and was clinically validated to be diagnostically equivalent to the longer, conventional exam. The 5-minute examination provides the basic clinical sequences including sagittal T1-weighted, axial T2-weighted, axial T2 TSE Dark Fluid (FLAIR), axial diffusion-weighted (DWI), and axial T2*-weighted sequences. Several factors, like parallel imaging with higher acceleration factors, gradient T1-weighted and EPI-GRE T2*-weighted acquisitions, have made it possible to shorten the scan time but have also alleviated EPI-related susceptibility artifacts and image distortions by reducing the EPI-factors and shortened the inter-echo spacing. The hope is that the 5-minute protocol will reach high diagnostic concordance for the diagnosis of clinically relevant findings compared to the conventional protocol, and therefore become useful in a selected group of pediatric patients that are more prone to motion and the need for anesthesia.

Case 1

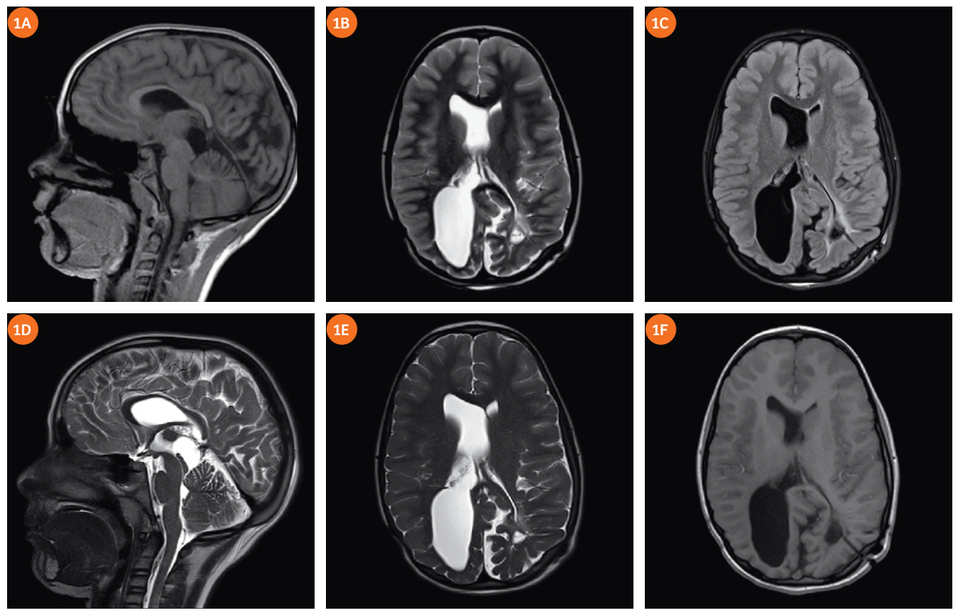

1 9-year-old female, congenital hydrocephaly with multiple shunt revisions. Top row GOBrain **(1A–C:** Sagittal T1w, axial T2 TSE, axial T2 TSE FLAIR). Bottom row, conventional fast sequences **(1D–F:** Sagittal T2w, axial T2 HASTE, axial T1 FLASH 2D). No interval change in the asymmetric size of the ventricular system or position of the shunt catheter (arrow). The studies are comparable, adding a T2 FLAIR (1C) sequence has the potential to further characterize fluid and brain findings.

Case 2

2 10-year-old female with severe traumatic brain injury. Top row GOBrain **(2A–D:** Sagittal T1w, axial T2 TSE, axial T2 FSE FLAIR, and axial T2*) obtained 3 days after the conventional MRI. Bottom row, routine sequences **(2E–H:** Sagittal T1w, axial T2w, axial FLAIR, axial DWI, and axial ADC). Findings consistent with brain contusion in the posterior parieto-occipital cerebral hemispheres and subdural bleed along the left tentorium (arrow). There is comparable conspicuity of the contusion and blood products with the routine and the GOBrain-5-minute protocol.

Case 3

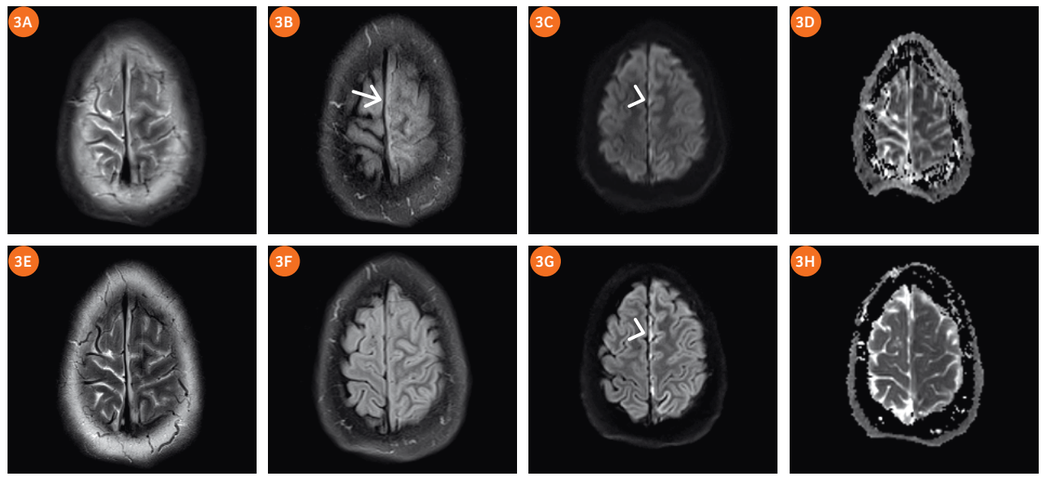

3 14-year-old male, complicated left frontal sinusitis with a left parasagittal extra-axial collection (arrow) resulting in meningitis. Top row GOBrain **(3A–D:** axial T2 TSE, axial T2 TSE FLAIR, axial DWI, and axial ADC) obtained the same day as conventional MRI. Bottom row, routine sequences **(3E–H:** axial T2w, axial FLAIR, axial DWI, and axial ADC). Diffusion restriction was appreciated in the left frontal sinus (not shown), in the left parasagittal collection (arrowhead). The cortical sulci in the left frontal and parietal lobe demonstrate mild effacement. The images exemplify the comparable image quality in the GOBrain-5-minute protocol (top row), compared to the conventional protocol (bottom row).

Case 4

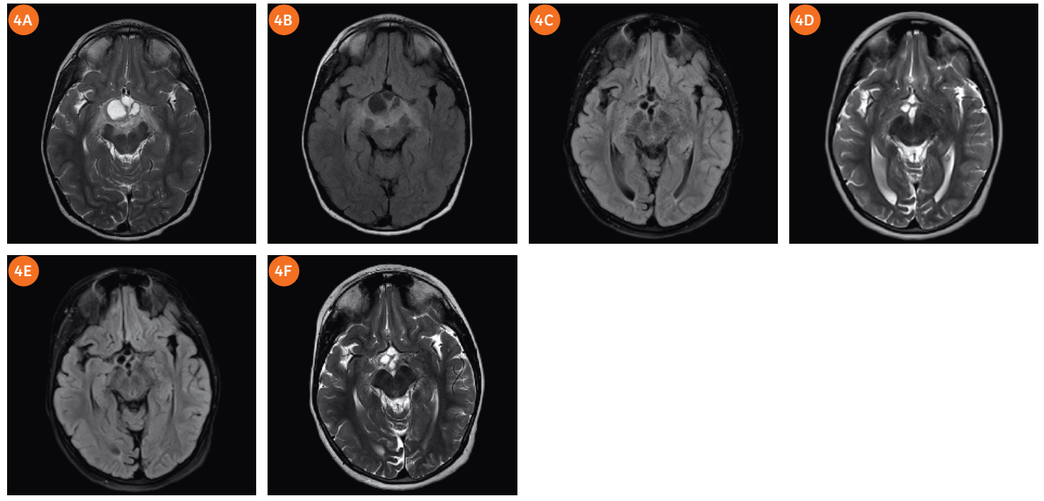

4 7-year-old female, suprasellar germinoma treated with chemotherapy and radiation. **4A, B**: baseline images before treatment. Top row GOBrain **(4C, D:** axial T2 TSE, and axial T2 TSE FLAIR). Bottom row, routine sequences **(4E, F:** axial T2w, and axial FLAIR) follow-up 2 years after treatment. The follow-up images exemplify the comparable image quality of the suprasellar residual lesion in the GOBrain-5-minute protocol (top row), compared to the conventional protocol (bottom row). Follow-up images using GOBrain and conventional protocols were obtained the same day.

Case 5

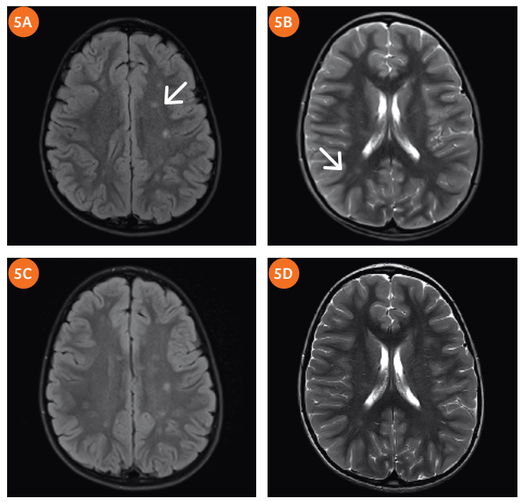

5 10-year-old male, 2 week history of morning headaches, waking up at night. History of anxiety. Suspected radiological isolated demyelinating type lesions. Top row GOBrain **(5A, B:** axial T2 TSE, and axial T2 TSE FLAIR). Bottom row, conventional sequences **(5C, D:** axial T2w, and axial FLAIR). The images exemplify the same number and size of white matter lesions (arrows) in the GOBrain-5-minute protocol (top row), compared to the conventional protocol (bottom row).

Materials and methods

All images in this case series were acquired on a 3T MAGNETOM Skyra scanner (Siemens Healthineers, Erlangen, Germany). The MRI protocol typically included the routine scan as per the radiologist's request and the additional GOBrain-5-minute sequence appended to the end of the examination (Table 1).

Conclusion

Pediatric fast imaging techniques can shorten scan times, decrease motion-related artifacts, and more importantly in children, has been shown to reduce the need for sedation[1]. In addition, they have the potential to reach diagnostic concordance of clinically relevant findings compared to the conventional protocol and therefore become useful in a selected group of pediatric patients that are more prone for motion and need of anesthesia. Improved patient throughput which decreases wait time can also be an advantage of this protocol.

Acknowledgement

We would like to acknowledge Ms. Wendy Rabbie MRT (R), Director Medical Imaging and Laboratory Medicine

References

[1] Ashley WW, Jr., McKinstry RC, Leonard JR, Smyth MD, Lee BC, Park TS. Use of rapid-sequence magnetic resonance imaging for evaluation of hydrocephalus in children. J Neurosurg. Aug 2005;103(2 Suppl):124-130.

[2] Forbes KP, Pipe JG, Karis JP, Farthing V, Heiserman JE. Brain imaging in the unsedated pediatric patient: comparison of periodically rotated overlapping parallel lines with enhanced reconstruction and single-shot fast spin-echo sequences. AJNR Am J Neuroradiol. May 2003;24(5):794-798.

[3] Miller JH, Walkiewicz T, Towbin RB, Curran JG. Improved delineation of ventricular shunt catheters using fast steady-state gradient recalled-echo sequences in a rapid brain MR imaging protocol in nonsedated pediatric patients. AJNR Am J Neuroradiol. Mar 2010;31(3):430-435.

[4] Brenner DJ. Estimating cancer risks from pediatric CT: going from the qualitative to the quantitative. Pediatr Radiol. Apr 2002;32(4):228-221; discussion 242-224.

[5] Ramaiah R, Bhananker S. Pediatric procedural sedation and analgesia outside the operating room: anticipating, avoiding and managing complications. Expert Rev Neurother. May 2011;11(5): 755-763.

[6] Missios S, Quebada PB, Forero JA, et al. Quick-brain magnetic resonance imaging for nonhydrocephalus indications. J Neurosurg Pediatr. Dec 2008;2(6):438-444.

[7] Penzkofer AK, Pfluger T, Pochmann Y, Meissner O, Leinsinger G. MR imaging of the brain in pediatric patients: diagnostic value of HASTE sequences. AJR Am J Roentgenol. Aug 2002;179(2):509-514.

[8] Iskandar BJ, Sansone JM, Medow J, Rowley HA. The use of quick-brain magnetic resonance imaging in the evaluation of shunt-treated hydrocephalus. J Neurosurg. Nov 2004;101(2 Suppl):147-151.

[9] Rozovsky K, Ventureyra EC, Miller E. Fast-brain MRI in children is quick, without sedation, and radiation-free, but beware of limitations. J Clin Neurosci. Mar 2013;20(3):400-405.

[10] Prakkamakul S, Witzel T, Huang S, Boulter D, Borja MJ, Schaefer P, et al. Ultrafast brain MRI: Clinical deployment and comparison to conventional brain MRI at 3T. J Neuroimaging 2016; 26(5): 503-150.

[11] Rapalino O, Heberlein K. New strategies for protocol optimization for clinical MRI: Rapid examiniations and improved patient care. MAGNETOM Flash 2016; 65: 22-25.

Contacts
Elka Miller, M.D., FRCPC
emiller@cheo.on.ca

Download GOBrain & GOBrain+ protocols

Heightened attention to healthcare costs and value based outcomes in medicine are driving revolutionary changes in the MR industry. Siemens MR and Massachusetts General Hospital (MGH) in Boston collaborate on strategies to develop fast and clinically validated examinations in MR.

GOBrain is a diagnostic brain exam which takes 5 minutes[1]. It consists of five diagnostically-important MR brain protocols acquired with optimized pulse sequences. Integrated with individual anatomical landmark-based AutoAlign technology providing automatic slice positioning, this push-button exam requires minimal interaction from the technologist. The included sequences are a sagittal T1-weighted, axial T2-weighted, axial T2-weighted DarkFluid, axial diffusion-weighted and an axial T2*-weighted contrast.

GOBrain+ expands GOBrain to additionally support brain imaging with contrast medium. New optimized sequences include an axial T1-weighted sequence administred pre- and post-contrast and a post-contrast MPRAGE.

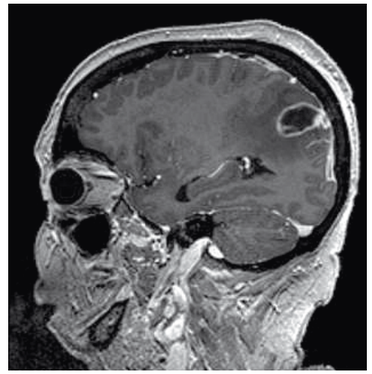

To download the .exar1 files for 1.5T with Head/Neck 20 and for 3T with Head/Neck 20, Head 32 or Head/Neck 64, visit:

usa.siemens.com/gobrain-protocols

[1]Achieved on a MAGNETOM Skyra with the Head 32 coil. Total examination time can take up to 6 minutes depending on system field strength and coil density.

FREEZEit StarVIBE: Freezing the Moving Head and Neck at a Sub-millimetric Scale

Marco Ravanelli; Davide Farina; Roberto Maroldi
Università degli Studi di Brescia, Radiologia 2, Spedali Civili Brescia, Italy

Introduction

3D sub-millimetric imaging is crucial for assessing complex anatomy and fine structures in the head and neck. That is why postcontrast 3D fat-saturated VIBE with isotropic spatial resolution of 0.5-0.8 mm has been included in all our Department's MRI protocols for head and neck lesions for around 15 years already. However, motion due to swallowing and breathing affects a high number of head and neck MR studies, and VIBE sequences are particularly prone to motion artifacts due to their long acquisition time and the underlying cartesian k-space filling scheme.

FREEZEit technology

FREEZEit with the StarVIBE sequence has been recently introduced by Siemens with the aim of reducing motion artifacts without sacrificing sub-millimetric isotropic resolution. The sequence employs an inplane stack-of-stars technique to reduce the effects of motion during phase-encoding. This has the added advantage that the center of k-space is sampled with every line, providing excellent contrast-agent sensitivity in contrast-enhanced scans. Our preliminary experience with FREEZEit in head and neck imaging demonstrates the strengths and clinical impact of this technique in selected patients.

Clinical impact

In Figure 1, the oral floor of a volunteer instructed to swallow every 20 seconds has been imaged with both conventional VIBE and StarVIBE. StarVIBE dramatically reduces motion artifacts, whilst key anatomic structures such as mandible, lingual septum, sub-lingual spaces are clearly better depicted and circumscribed. Furthermore, fat saturation is improved by reducing motion artifacts. Compared to conventional VIBE, the signal-to-noise ratio (SNR) is slightly reduced, which has been counterbalanced by using a lower matrix, slightly thicker slices and lower slice resolution, a parameter affecting the quality of multiplanar reconstructions (Table 1). An alternative strategy might be to increase the number of spikes, resulting in a longer acquisition time but uncompromised SNR.

This is why conventional cartesian VIBE is still used in our institution as the standard approach for cooperative patients. In our clinical experience of dealing with uncooperative patients, StarVIBE was effective in reducing

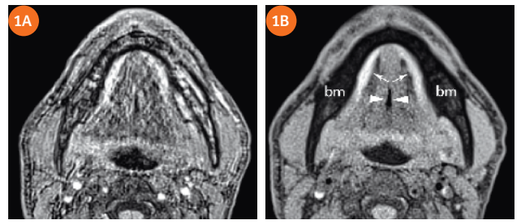

1 Conventional cartesian VIBE **(1A)** and StarVIBE **(1B)** in comparison in a moving volunteer. In the StarVIBE image, key structures of the oral cavity are well depicted despite movement: lingual septum (opposite arrowheads), extrinsic muscles, sublingual spaces (small arrows), mandible with optimal suppression of fatty bone marrow (bm). The same structures are blurred and not assessable with a sufficient diagnostic quality in the conventional VIBE image.

Table 1: Sequence parameters

	Oral cavity		Larynx (surface coils)	
	StarVIBE	conventional VIBE	StarVIBE	conventional VIBE
FOV (mm)	205 x 205	270 x 186	190 x 190	190 x 154
thickness (mm)	0.8	0.7	0.7	0.6
in-plane resolution	0.8 x 0.8	0.7 x 0.7	0.74 x 0.74	0.6 x 0.6
matrix	256 x 256	384 x 384	256 x 256	320 x 320
slice resolution	50%	72%	65%	50%
slices	176	192	88	112
phase partial Fourier	off	6/8	off	6/8
slice partial Fourier	5/8	7/8	5/8	7/8

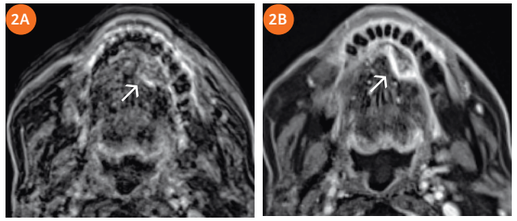

2 Conventional cartesian VIBE **(2A)** and StarVIBE **(2B)** in a patient followed for previously treated carcinoma of the right cheek. StarVIBE clearly depicted a metachronous lesion in the left anterior oral floor, which might have been missed with conventional VIBE due to motion artefact.

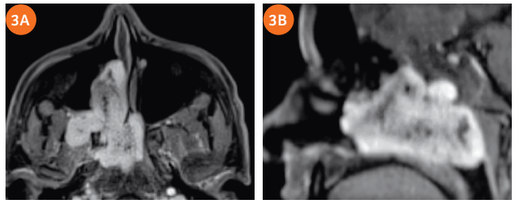

3 StarVIBE in a young uncooperative patient[1] with juvenile angiofibroma. The sequence has been acquired on axial plane and reconstructed on sagittal plane. A lack of quality in sagittal reconstruction is visible compared to axial images due to low spatial resolution along the slice selection direction (slice resolution 50%). However, both native and reconstructed images are free from motion artefacts. StarVIBE was the unique option for volumetric sequence to be acquired in such a patient.

motion artifacts in the oral cavity. A striking example is reported in Figure 2: A tumor of the anterior left oral floor was incidentally found with StarVIBE during a follow-up study for a different primary head and neck cancer. As shown in the example it is evident how the lesion conspicuity is improved with StarVIBE compared to conventional VIBE due to the substantial reduction of motion artifacts.

In the sinonasal tract and the skull base, motion artifacts are usually fewer than in anatomical areas closer to the pharynx and larynx, and therefore conventional VIBE is usually effective. However, in very uncooperative patients, StarVIBE represents the unique volumetric sequence to produce images with sufficient diagnostic quality, as in a young patient[1] affected by juvenile angio-fibroma and post-neonatal ischemic encephalopathy (Fig. 3).

Moving down from the skull base into the infrahyoid neck, the larynx is one of the regions which benefits the most from the use of StarVIBE. It is a subtle anatomical area which is subject to breathing and swallowing movements but ideally should be imaged with very high spatial resolution. We therefore apply small loop surface coils to image the larynx and hypopharynx. In this region and with these coils, StarVIBE has enough SNR to increase spatial resolution compared to e.g. the oral cavity, where we reduce the field-of-view (FOV) and slice thickness and increase the resolution. With the introduction of StarVIBE we are now able to image this particular region with sufficient suppression of motion artifacts while gaining

[1]MR scanning has not been established as safe for imaging fetuses and infants less than two years of age. The responsible physician must evaluate the benefits of the MR examination compared to those of other imaging procedures.

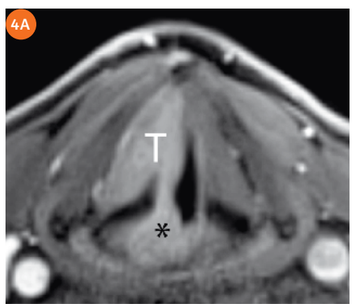

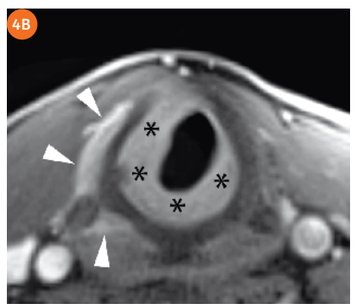

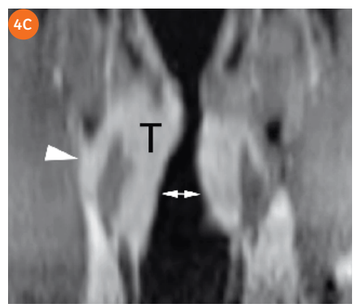

4 StarVIBE with surface coils in an uncooperative patient with T4a glottic-subglottic cancer. The sequence has been acquired on axial plane. Tumor (T) extends to posterior commissure (asterisk in **4A**) surrounding right arytenoid cartilage, Tumor circumferentially infiltrates subglottic region (asterisks in **4B**, opposite small arrows in the coronal reconstruction) and extends outside the larynx through the right inferior paraglottic space (arrowhead on **4C**) infiltrating lateral and posterior cricoarytenoid muscles (arowheads in **4B**).

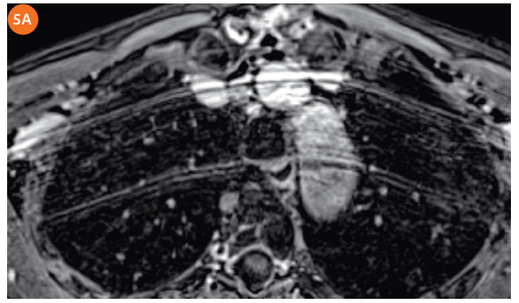

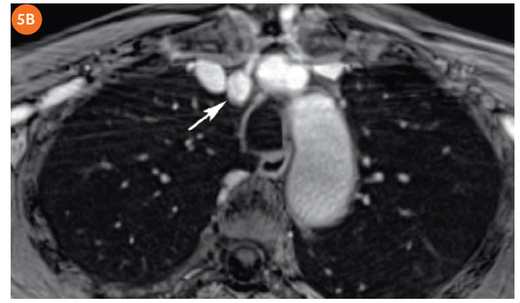

5 Conventional cartesian VIBE **(5A)** and StarVIBE **(5B)** in a patient with recurrent thyroid cancer. On the conventional VIBE image, breathing artefacts make a pathological lymph node in the upper mediastinum (arrow) not easily visible. Artifacts are almost completely suppressed with StarVIBE and the same lesion is clearly visible.

excellent SNR to apply very high spatial resolution. For this reason, in our experience StarVIBE is not only indicated in uncooperative patients but provides some advantages also in compliant patients. Therefore, StarVIBE is replacing conventional cartesian VIBE in our standard imaging protocol for imaging of the larynx and hypopharynx (Fig. 4). Furthermore, given the relatively high slice thickness, which negatively impacts 3D reconstruction capabilities, we typically acquire a second StarVIBE dataset in coronal or sagittal orientation, when postcontrast sections along these planes are clinically indicated.

Moving further down to the lower limit of the neck, StarVIBE was very effective in imaging superior mediastinal lymphadenopathies from a recurrent Tx cancer (Fig. 5), reducing breathing artifacts at the pulmonary apices.

Conclusion

StarVIBE is a helpful tool in uncooperative head and neck patients, especially when oral cavity and infrahyoid neck are studied. In compliant patients, conventional VIBE is generally preferable because of the adoption of a more efficient "SNR per acquisition time" ratio. When studying the larynx with surface coils, the surplus in SNR can be spent to increase respective resolution parameters, obtaining a spatial resolution similar to conventional VIBE, with significantly less motion artifacts. As we have demonstrated in this case series, StarVIBE can help to detect pathologies which might be mimicked in conventional scans due to severe artifacts and hence is considered to provide additional value to our daily clinical practice.

Contacts
Marco Ravanelli
marcoravanelli@hotmail.it

New Protocol for the MR Imaging of Pituitary Adenomas. Multiphase, Dynamic and Volumetric Imaging on MAGNETOM Skyra

The Importance of StarVIBE and CAIPIRINHA Sequences

Denis Gardeur, M.D.
Centre RMX, Paris, France

Introduction

The visualization of pituitary microadenomas can be a diagnostic challenge for the radiologist even with MRI. Higher spatial resolution enabled by higher field strengths (3T) has been reported to improve the visualization of small adenomas, especially those known to be most difficult to visualize, for example, the adrenocorticotropic hormone (ACTH) and growth hormone (GH) producing pituitary adenomas. Stobo et al. reported a sensitivity improvement from 54% to 85% when going from 1.5T to 3T[1]. Dynamic contrast-enhanced (DCE) MRI has also been shown to improve diagnostic performance[2,3].

Some pituitary microadenomas can be visualized without contrast media injection, seen as T2 hyperintensities in the coronal plane. However, many microadenomas are depicted in MRI only after injection of gadolinium due to different pharmacokinetics of contrast enhancement as compared to a healthy pituitary. Microadenomas typically show a delayed peak of enhancement[8] which is often less intense compared to the normal anterior pituitary (90 to 120 ms vs 60 to 80 ms). This makes them appear relatively hypointense in the series of scans performed a few seconds after the injection of gadolinium chelate (see Figure 1 for mean curves of relative enhancement of normal anterior pituitary and microadenomas).

However, not all pituitary microadenomas have the same pharmacokinetics of enhancement. Not all of them are vascularized by the hypophyseal portal system with a delay of interstitial diffusion of contrast medium compared to a normal pituitary gland. Some of them are partially or totally vascularized by pituitary arteries and may enhance earlier than the normal anterior pituitary. Others, conversely, have necrotic or hemorrhagic components which are sometimes predominant and enhance later and less intensively. In the case of a recent hemorrhagic conversion, parametric imaging and subtracted images are useful because these microadenomas might have a T1 hypersignal before the injection and become isointense compared to normal pituitary gland after injection. Some microadenomas could be cystic and difficult to differentiate compared to simple non-tumor cysts of the pars intermedia and Rathke's pouch. Here, again, dynamic studies are useful because simple cysts have no enhancement and a flat kinetic curve. ACTH microadenomas often have an enhancement kinetics that are closer to that of the anterior pituitary and are, therefore, more difficult to detect than prolactin and GH microadenomas[7].

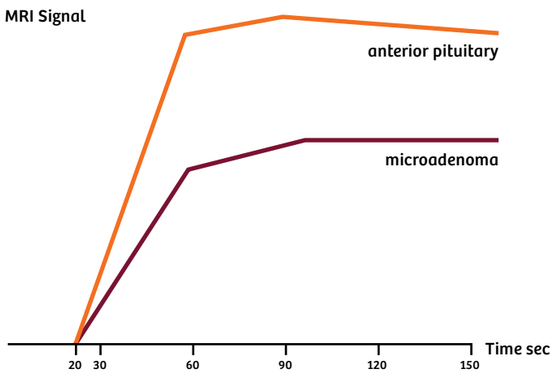

1 Pituitary microadenoma pharmacokinetic.

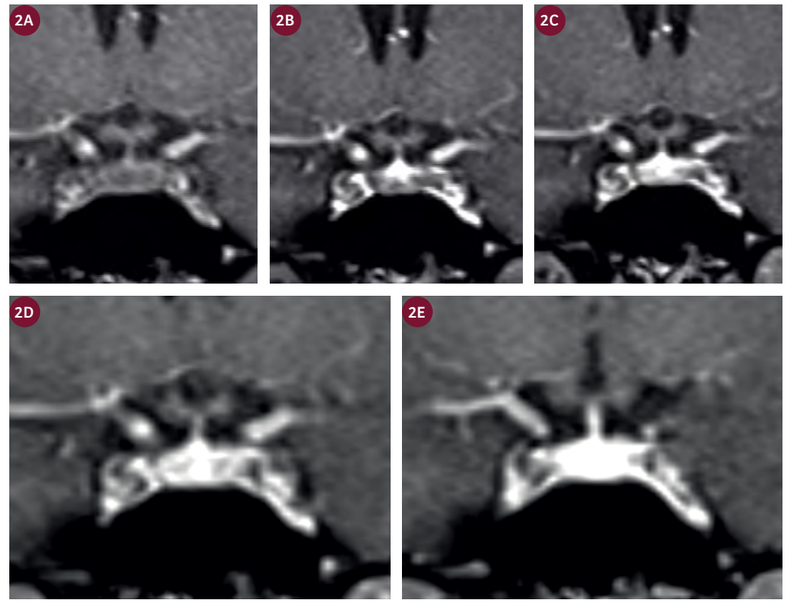

2 Normal pituitary MRI of an 18-year-old woman. Dynamic study after injection of gadolinium chelate. 3D StarVIBE series with 6 repetitions for an overall acquisition time of 150 seconds. First stage **(2A)** arrival of the bolus in the carotid.
Next step: arteriolar opacification of the posterior pituitary **(2B)**.
Next step: opacification of the pituitary stalk and of the hypophyseal portal venous system **(2C)**. Then, progressive opacification of the anterior pituitary **(2D, E)**.

New sequences, such as FREEZEit StarVIBE and CAIPIRINHA VIBE, enable high-resolution, temporal and spatial, 3D dynamic studies[4,5,8]. The 3D acquisitions allow multiplanar reformats for better visualization of very small (even sub-millimeter) lesions while the high temporal resolution imaging provides better sensitivity to display pharmacokinetic differences.

We have developed a new MRI examination for pituitary microadenomas on our 3T MAGNETOM Skyra scanner which combines high-resolution volumetric as well as a multiphase, dynamic imaging.

This examination starts with a native series of sagittal T1-weighted, coronal T2-weighted and coronal T1-weighted TSE images with thin slices (1.5 to 2 mm). We then inject contrast with a 'half dose' (7 cc at a rate of 2 cc/sec) which has been shown to be sufficient for the detection of microadenomas. We then run a dynamic series – CAIPIRINHA VIBE – with 12 slices of 2 mm thickness in 6 repetitions with a total acquisition time of 2 min 30 sec. With this acquisition, we see several stages of enhancement:

a) early stage with arterial opacification blush of post pituitary then of pituitary stalk, then

b) intermediate stage with opacification of the hypophyseal portal venous system, then

c) progressive opacification of anterior pituitary supported by the portal system.

Microadenomas usually enhance later (and often less intensely) than other portions of the anterior pituitary and appear relatively hypointense[9] during this early opacification stage of the anterior pituitary. The dynamic multi-slice protocol provides many different parameters: wash-in, wash-out, time-to-peak (TTP), area under the curve (AUC), etc. These parameters help the radiologist to improve the detectability of microadenomas, especially wash-in and AUC. In addition, this dynamic multi-slice series provides other diagnostic elements such as visualization of hypothalamic-pituitary pharmacokinetics, mass effect on pituitary stalk, diagnostic with other hypervascular intrasellar process, aneurism, intrasellar artery or vein. Some microadenomas could be hypervascular in the arterial phase and are only visible in a dynamic study [6]. In a CT dynamic study, Bonneville et al. reported that 34% of microadenomas had a partial or complete early opacification before the portal opacification stage, demonstrating a direct arterial vascularization and not only a pituitary portal as mostly observed in anterior pituitary microadenomas. It seems that such hyper-arterialized microadenomas, opacified at early time, are less often observed in MRI, but they could be visualized by these new 3D dynamic protocols with multiparametric imaging.

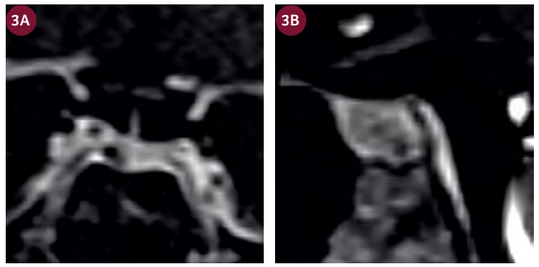

3 Prolactin microadenomas of a 29-year-old woman. Despite its small size of 1.4 mm diameter, this microadenoma – initially isointense on T1 without injection – is marked out in the dynamic VIBE series. It is relatively hypointense compared to the normal anterior pituitary, and the contrast is optimal during the phase of 75 seconds after injection of chelate gadolinium. On a second high-resolution volume series CAIPIRINHA with re-injection, the microadenoma is visualized in the 3 space plans, illustrated by this parasagittal reformation.

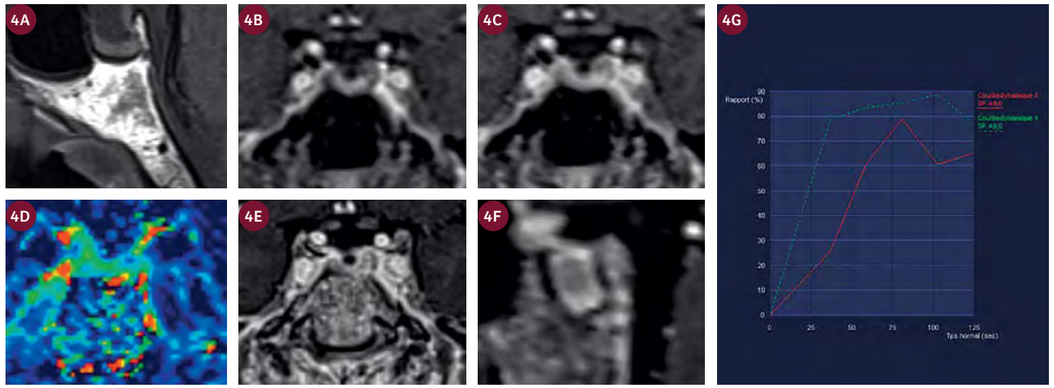

4 Hyperprolactinaemia of a 53-year-old man. Pituitary MRI without injection shows an 'empty' sella turcica with pituitary residue pressed against the sellar floor **(4A)**. VIBE multiphase dynamic series shows a lateralized lesion in left wing pituitary **(4B, C)** with a delay of relative opacification on wash-in parametric imaging **(4D)**. On a CAIPIRINHA volumetric series with re-injection, this left side microadenomas with empty sella turcica is visualized in the 3 space plans **(4E, F)**. Visualization of microadenomas on empty sella turcica is difficult with 2D TSE pituitary classic protocols. **(4G)** The comparative analysis of the pharmacokinetic curve of microadenoma opacification (red curve) and of the normal anterior pituitary (green curve) show both the delay and the lowest relative microadenoma opacification. The relative contrast (hypointensity of microadenoma) predominates between 50 and 80 seconds following the injection of contrast medium.

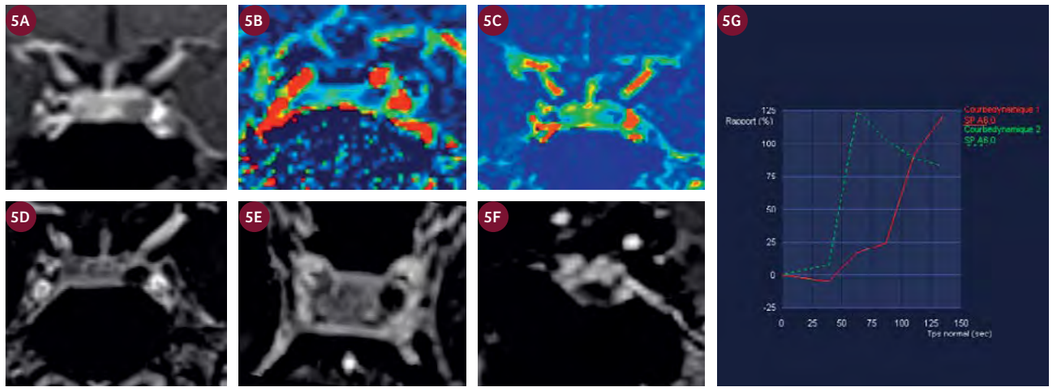

5 Prolactin microadenomas of a 57-year-old woman. Dynamic MRI StarVIBE. Opacification stage of the anterior pituitary **(5A)**, the microadenoma is hypointense compared to the rest of the anterior pituitary. Thanks to the 6 stages of this dynamic series, parametric imaging can be visualized, wash-in **(5B)** and time-to-peak **(5C)** showing the lesion of the left side portion of the pituitary gland and its relative opacification delay. In a second volume series **(5D-F)** CAIPIRINHA enables microadenomas reformations in the 3 space plans. The comparative analysis of the pharmacokinetic curve of microadenoma opacification (red curve) and of the normal anterior pituitary (green curve) show both the delay and the lowest initial microadenoma opacification. The relative contrast (hypointensity of microadenoma) predominates between 60 and 90 seconds following the injection of contrast medium **(5G)**.

However, the spatial resolution in these dynamic studies (which favors temporal resolution and series multiplication) is lower than on the conventional series (even with these new fast 3D sequences). We find it clinically useful to continue with one (or several) high-resolution scans, but there is a risk of making these scans at a pharmacokinetic stage when progressive opacification of adenoma meets or even exceeds that of the healthy pituitary, which decreases the detectability of microadenomas.

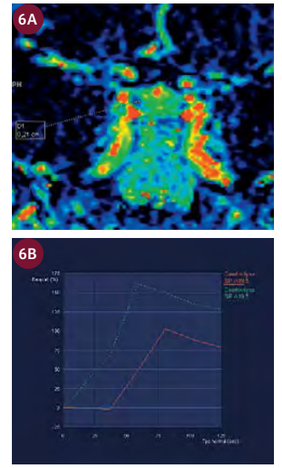

6 Prolactin microadenoma of a 27-year-old woman. It can only be visualized with a dynamic study and mainly with parametric imaging wash-in due to its delay in opacification compared to a healthy pituitary gland. It is visible at the right side next to the cavernous sinus and has a size of 2 mm. On the same coronal wash-in image the early vascularization of the hypophyseal portal system and of the pituitary stalk are visualized, shown red in the superomedian part of the pituitary gland. A comparative study of enhancement kinetics between the microadenoma (red curve) and the lateral left part of the anterior pituitary (green curve) shows the delay in opacification of the microadenoma. But in the second minute after the injection, it becomes isointense and therefore it is impossible to visualize without re-injecting contrast medium.

The new FREEZEit StarVIBE sequence has an advantage over the T1 TSE sequence as it enables a high-resolution submillimetric and isotropic volume acquisition in one acquisition (48 sections of 0.8 mm in 3 min 50 sec in our protocol) together with the ability to perform 3D multiplanar reformats. As dynamic imaging has been performed with a half dose, we inject a further half dose at a lower rate (0.5 cc/sec) for a total injected dose of 15 cc. This biphasic protocol enables us to make a volume acquisition with submillimeter slices while maintaining the best relative pharmacokinetic detectability of adenomas vs healthy anterior pituitary. Thanks to this high spatial resolution volume acquisition, (sub) millimeter microadenomas—relatively hypointense—can be visualized in 3D space. Even in the most difficult diagnostic circumstances, such as microadenomas on empty sella turcica, we are able to better visualize microadenomas.

In conclusion, this protocol combines the advantages of dynamic and anatomic studies in high resolution while using a standard gadolinium injection dose and in an exploration time substantially similar to the one of a classic protocol (with 2D TSE series). The combination of images 3D dynamic studies with high spatial and temporal resolution improves the visualization of microadenomas and contributes to better differential diagnostics, which in turn optimizes the diagnostic sensitivity and specificity of MRI for pituitary tumors.

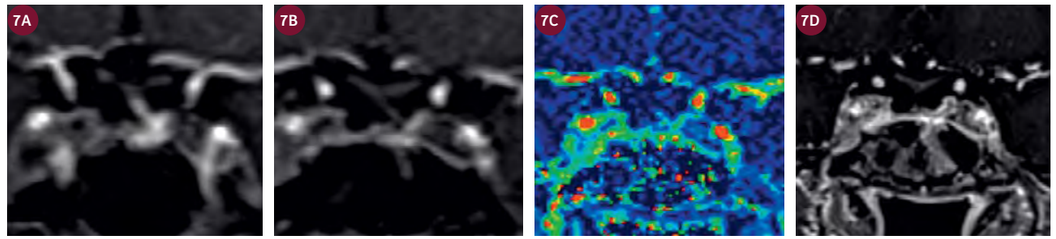

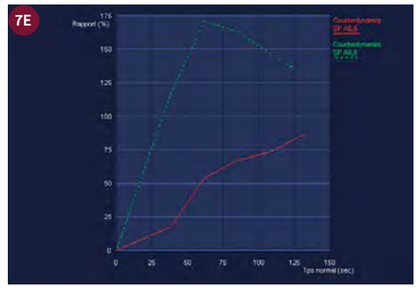

7 40-year-old woman operated 6 years ago for an ACTH pituitary adenoma and referred 2 years later to focal radiotherapy due to an invasive recurrence. Follow-up non-contrast pituitary MRI shows partial empty sella and inhomogeneous tissue adjacent to the left cavernous sinus. Dynamic contrast-enhanced MRI shows pituitary stalk deviation to the left and pituitary portal blush. The pituitary adenoma recurrence is well delineated between the portal blush and the left cavernous sinus. A delayed series **(7D)** demonstrates progressive enhancement of the adenoma. Pharmacokinetic curves **(7E)** demonstrate delayed but progressive enhancement of the adenoma. So it is not a post radiotherapy cyst or radiation necrosis (with a plateau curve) but a solid recurrence.

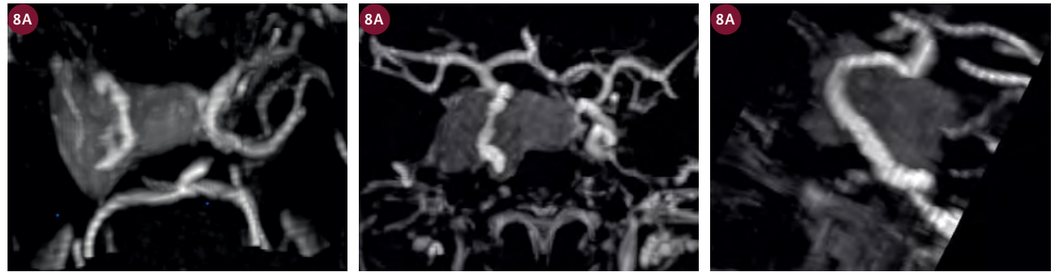

8 Invasive pituitary macroadenoma which infiltrates widely the right cavernous sinus. The dynamic MRI after injection of gadolinium does not aim at visualizing the voluminous adenoma, but at characterizing its kinetics of opacification (similar to the normal pituitary gland) and at visualizing the areas of hyperperfusion or necrosis. The main interest is the possibility of multiplanar reconstruction of the adenoma thanks to the 3D acquisition and mostly to carry out an angioMRI analysis of the stretched, infiltrated and irregular carotid artery as the adenoma covers completely the endo-cavernous carotid.

References

[1]Stobo DB et al. Initial experience of 3T versus conventional field strength MRI of small functioning pituitary tumors. Clin Endocrinology. 2011. 75:673-7.

[2]Rand T et al. Evaluation of pituitary microadenomas with dynamic MRI. EUR J Radiol 2002 41:131-5.

[3]Sakamoto Y et al. Normal and abnormal pituitary glands: gadopentate-enhanced MR imaging. Radiology 1991. 178:441-5.

[4]Rossi Espagnet MC et al. High resolution DCE MRI of the pituitary gland using radial k space acquisition with compressed sending reconstruction. AJNR. 2015. 10.3174:1-6.

[5]Fushimi Y et al. 3D dynamic pituitary MRI with CAIPIRINHA.EUR. J Radiology. 2014-83:1900-6.

[6]Bonneville JF et al. Pituitary microadenomas: early enhancement with dynamic CT, implications of arterial blood supply and potential importance. Radiology. 1993. 187:857-61.

[7]Kim B. Comparison of CAIPIRINHA VIBE, radial VIBE and conventional VIBE sequences for DCE MRI. Magnetic Resonance Imaging. 2016.38:638-644.

[8]High-Resolution DCE-MRI of the Pituitary Gland Using Radial k-Space Acquisition with Compressed Sensing Reconstruction M.C. Rossi Espagnet, L. Bangiyev, M. Haber, K.T. Block, J. Babb, V. Ruggiero, F. Boada, O. Gonen and G.M. Fatterpekar. American Journal of Neuroradiology August 2015, 36 (8) 1444-1449; DOI: https://doi.org/10.3174/ajnr.A4324.

[9]Imaging of the pituitary: Recent advances. Chaudhary V, Bano S. Indian Journal of Endocrinology and Metabolism. 2011;15(Suppl3):S216-S223. doi:10.4103/2230-8210.84871.

Contacts
Denis Gardeur, M.D.
dgimag@aol.com

For additional information and resources, please visit usa.siemens.com/magnetom-world

fMRI Made Easy with an Integrated Siemens Healthineers and NordicNeuroLab Solution

Marte Thuen, Ph.D.; Cathy Elsinger, Ph.D.
NordicNeuroLab, Bergen, Norway

BOLD fMRI is emerging as standard method of care for presurgical planning—mapping eloquent regions of the brain before brain surgery. What used to be a complicated setup available only to researchers is now available in the clinical radiology department. NordicNeuroLab provides a complete and easy-to-use fMRI solution—all necessary equipment for fMRI and nordicAktiva stimulus presentation software seamlessly integrated with the Siemens Numaris platform. This allows the user to run the paradigms directly from the Siemens Numaris interface, enhancing workflow for the MR technologist.

What is BOLD fMRI?

BOLD fMRI is the study of neuronal activity using MRI (Fig. 1). When a particular part of the brain becomes active as a response to a stimulus or task, there is increased flow of oxygen-rich blood into this region Because of the difference in MR signal properties between the blood cells that carry oxygen compared to those that do not, this increase in blood supply can be detected using MRI. However, due to the level of sensitivity required to detect this signal difference, a specialized pulse sequence is needed on the MR scanner. This dynamic series measures the signal changes throughout the brain while a person is cued to perform a particular task. Task performance alternates with cycles of rest (20-30 seconds cycles), allowing a comparison of signal change in the brain due to the task. The description and timing of the cueing task are referred to as the fMRI paradigm.

Typical brain regions that can be mapped using fMRI are the motor cortex (finger tapping, toe movement, tongue movement), sensory regions (visual cortex, auditory cortex) and speech centers.

Why is fMRI important?

One goal of pre-operative surgical planning is to differentiate eloquent areas in the brain from pathology—those regions of the cortex in which injury produces cognitive or motor deficit—and to understand the relationship between eloquent cortex and pathology. The goal is to accurately delineate tissue pathology from surrounding eloquent cortex and vital connections between brain regions to aid in decision making that will maintain a balance between taking a more aggressive resection approach and reducing postoperative deficits. Furthermore, tumors and other pathologies can push brain activity regions out of their expected position, so mapping is critical to ensure maximum safe resection and for determining point of entry. This is of particular interest for determining language lateralization. Language representation can be investigated noninvasively using fMRI. This will reduce the risk of aphasia or other language deficits post surgery [1].

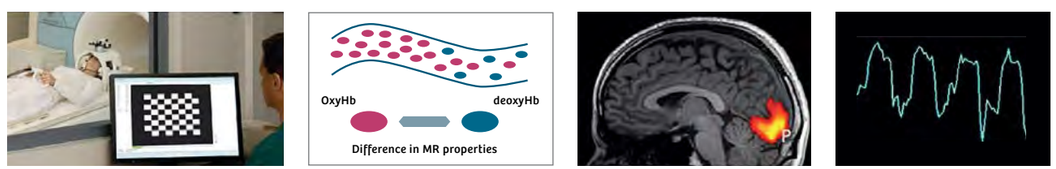

1 When a particular part of the brain becomes active, there will be an increased local blood flow. This can be detected using MRI, and will lead to an increased signal in the activated area.

2 The NNL VisualSystem attached to the headcoil **(2A)**, or the NNL InroomViewingDevice **(2B)** are displaying the paradigm during fMRI. The NNL AudioSystem and ResponseGrip **(2A)** are used to provide audio stimuli and to collect patient response.

In addition to providing critical information in advance of the surgery, BOLD fMRI maps can be used within surgical navigation systems during brain surgery to guide intra-operative decision-making. The use of BOLD fMRI results preoperatively or intraoperatively has the potential to reduce neurological deficits by influencing the surgical approach, allowing for more radical tumor resection while potentially reducing craniotomy size, reducing operating time and the need of awake surgery [1-4].

What equipment is needed for BOLD fMRI?

A high-quality fMRI study will require the patient to be cued to perform a particular cognitive or motor task while in the MR scanner. They can be presented with a visual stimulus (such as flickering checkerboard), be asked to read text (language study) or be cued to make finger movements using a response device. To present the stimuli, as well as inform the patient about whether they should perform a task or simply rest, a display needs to be available for the patient inside the MR bore. The patient can view the display via an MR compatible display attached to the head coil, NordicNeuroLab (NNL) VisualSystem, (Fig. 2A), or via a mirror mounted on top of the headcoil, which presents the image from an MR compatible monitor placed outside the MR scanner (NNL InroomViewingDevice, Fig. 2B). It is also possible to present stimuli to the patient via audio, using the NNL AudioSystem MR compatible headphones (Fig. 2A). These can also be used for patient communication. Patients can respond to language or motor tasks using the NNL ResponseGrip, which also provide a means of monitoring patient responses to various tasks (Fig. 2A).

All equipment used in the MR room must be MR compatible, that is, it must be able to operate safely in a strong magnetic field without causing distortions or artefacts in the MR image. The appropriate BOLD paradigm is presented using the nordicAktiva software, which contains a library of stimulus paradigms covering a wide range of cognitive, language and motor tasks. Enabling the BOLD Dot AddIn integration between the Siemens Numaris platform and nordicAktiva allows the paradigm to be selected and started from within the Numaris environment (Fig. 3). The MR acquisition must be synchronized with the timing of the paradigm, and this is taken care of by the NNL SyncBox which correlates the scanner's trigger pulse to the onset of the paradigm.

"We have been using the NNL fMRI equipment for about 10 years now in a clinical as well as a scientific setting. The efficiency using the products is very high, because of their easy usability and robustness. We are very satisfied with our decision to use NNL equipment."

Professor Dr. Bernd Weber
Head of NeuroCognition, Imaging, Life&Brain Center
Bonn, Germany

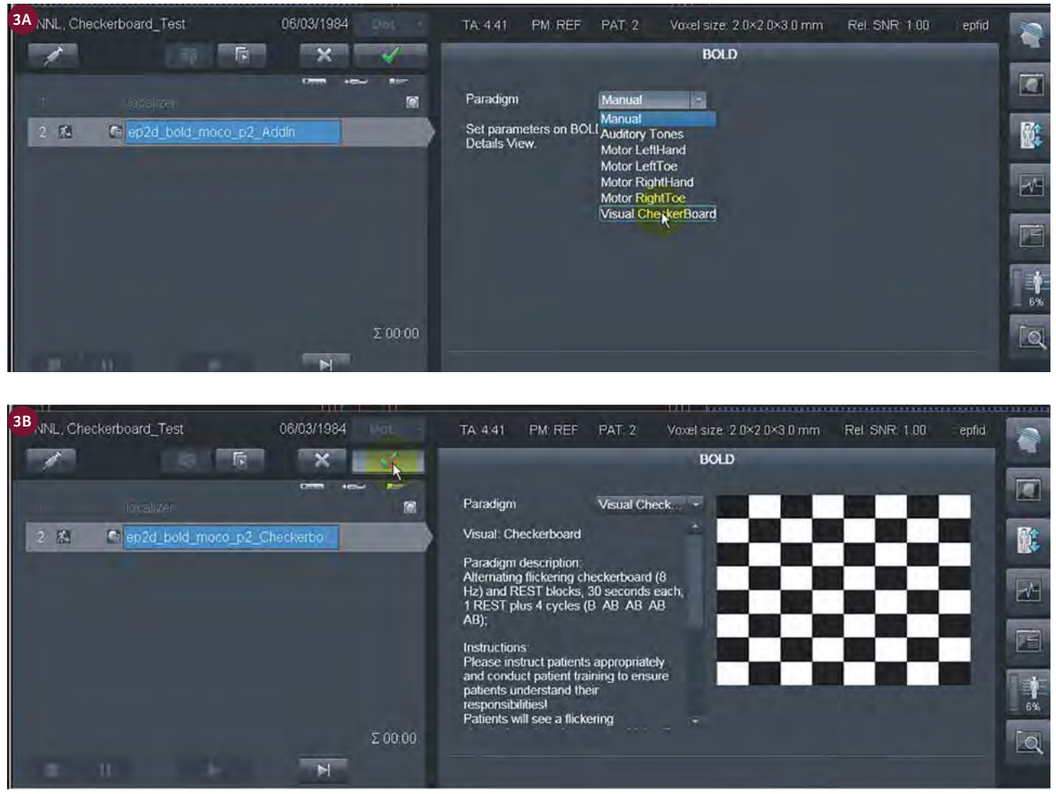

3 When enabling the BOLD Dot AddIn, the user can select the paradigm directly in Siemens Numaris **(3A)**. The lower image **(3B)** shows that a visual stimulation paradigm has been selected.

How to select the appropriate fMRI task?

The aim of presurgical fMRI is to map relevant regions surrounding pathology, so the type of paradigm to be done will be specific to the cortical region of interest (e.g. motor cortex). Tasks are selected that target the regions of interest and are possible for the patient to perform easily. The patient should be trained on each task to ensure that they completely understand the instructions and are able to perform the tasks well.

Task selection can be done directly from the Siemens Numaris workstation (Fig. 3). The paradigm will then be displayed visually on the device inside the MR scanner (NNL VisualSystem or NNL InroomViewingDevice), or aurally, via the headphones, depending on paradigm chosen. The NNL SyncBox will ensure that the paradigm presentation and MR image acquisition are synchronized precisely. A typical fMRI task alternates between a period of rest and activity (30 seconds, for approximately 4 cycles, about 5 minutes in total).

Once the fMRI session is complete, fMRI image data must be processed before the results can be sent to PACS or used for surgical planning (Fig. 4).

How to do fMRI:

- Select paradigms based on location of pathology and functions to map.
- Train patient to ensure they understand and can perform the tasks.
- Select paradigm on Siemens Numaris.
- Run the fMRI using the NNL fMRI equipment for displaying the paradigm to the patient.
- After fMRI: send data to workstation dedicated for fMRI postprocessing.

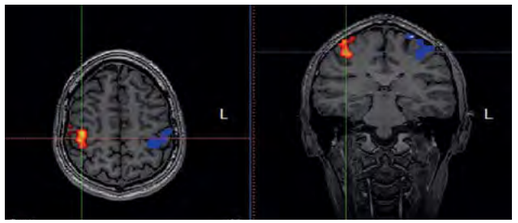

4 BOLD fMRI results of left (red) and right (blue) finger tapping from a healthy volunteer.

Contact
Marte Thuen, Ph.D.
marte@nordicneurolab.com

References

[1] Medina et al.: Seizure Disorders: Functional MR imaging for diagnostic evaluation and surgical treatment – Prospective study. Neuroradiology 236, 2005.

[2] Petrella et al.: Preoperative functional MR imaging localization of language and motor areas: Effect on therapeutic decision making in patients with potentially resectable brain tumors. Radiology 240, 2006.

[3] Håberg et al.: Preoperative blood oxygen level-dependent functional magnetic resonance imaging in patients with primary brain tumors: clinical applications and outcome. Neurosurgery 54, 2004.

[4] Wilden et al.: Strategies to maximize resection of complex, or high surgical risk, low-grade gliomas. Neurosurg Focus 34, 2013.

Different NNL packages may be available for different MR systems in the US. Please contact your local sales representative for details.

syngo.MR Neuro 3D: Your All-In-One Postprocessing, Visualization and Reporting Engine for BOLD Functional and Diffusion Tensor MR Imaging Datasets

Julien Gervais; Lisa Chuah
Siemens Healthineers, Magnetic Resonance, Erlangen, Germany

syngo.MR Neuro 3D enables a streamlined postprocessing and visualization of functional BOLD and diffusion tensor images. For clinical insights into the use of fMRI and DTI in the clinical settings, we would like to refer the interested reader to these case series [1, 2, 3].

Within this article, we have described our preferred workflow and steps for the processing and analysis of BOLD fMRI and diffusion tensor imaging (DTI) data.

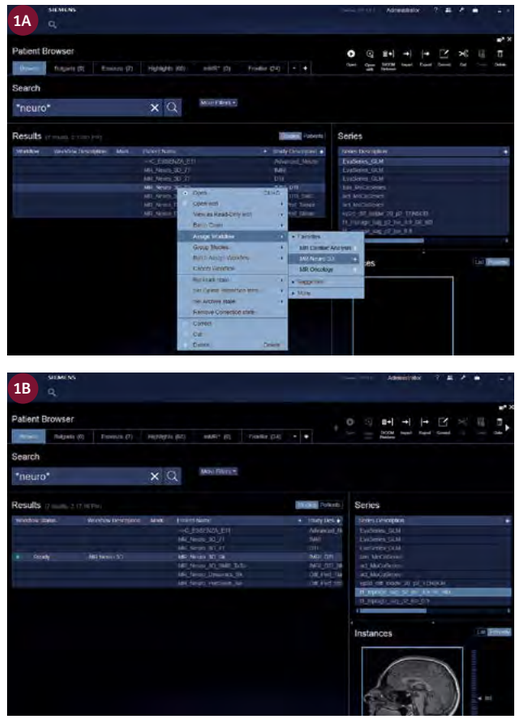

1 **(1A)** Case assignment to Neuro 3D with a right mouse click. **(1B)** When the case is ready, the 'Workflow Status' changes from 'Scheduled' to 'Ready'.

Obviously, it is not necessary to have both BOLD fMRI and DTI datasets available for each patient, syngo.MR Neuro 3D can be used even if there is only BOLD fMRI or DTI data for a patient.

First step: Open the case

Assign the complete case to syngo.MR Neuro 3D with a right-mouse click and selection of the option 'Assign' with further selection of 'MR Neuro 3D' (Fig. 1A). Once the case has been assigned, the status of the case changes from 'Scheduled' to 'Ready' (Fig. 1B). Open the case by double clicking on it.

For faster loading, select only the relevant series (BOLD MOCO, GLM, Tensor, anatomical data) by multi-selection with 'Ctrl' key and left mouse clicks (Fig. 2). Follow this with a right mouse click and selection of the option 'Read only' with further selection of 'MR Neuro 3D' (Fig. 2). syngo.MR Neuro 3D can accept more than one BOLD series with the capability of visualizing activations for up to 4 different paradigms simultaneously. However, the corresponding GLM must also be loaded. For tractography analysis, only the TENSOR data is required. The raw diffusion series does not have to be loaded. syngo.MR Neuro 3D can accept data collected in different scan sessions (e.g., the patient anatomical and DTI data were collected in separate scan sessions from the BOLD data).

2 Multi-selection of the relevant datasets to be opened as 'read only' for Neuro 3D.

Second step: Alignment

The BOLD and DTI data should be registered to a reference scan, usually the anatomical scan such as the MPRAGE. Accurate alignment is especially critical for the analysis of data acquired in different scan sessions.

The alignment overview displays all available series overlaid on the reference scan. This is the starting point for registration (Fig. 3). A drop down menu in the Control Area on the far left enables the selection of different overlay palettes, such as 'Edges' or 'Perfusion', to help visual assessment of co-registration accuracy (Fig. 4). In addition, a blending functionality is available.

3 The alignment overview with all available series overlaid on the reference scan.

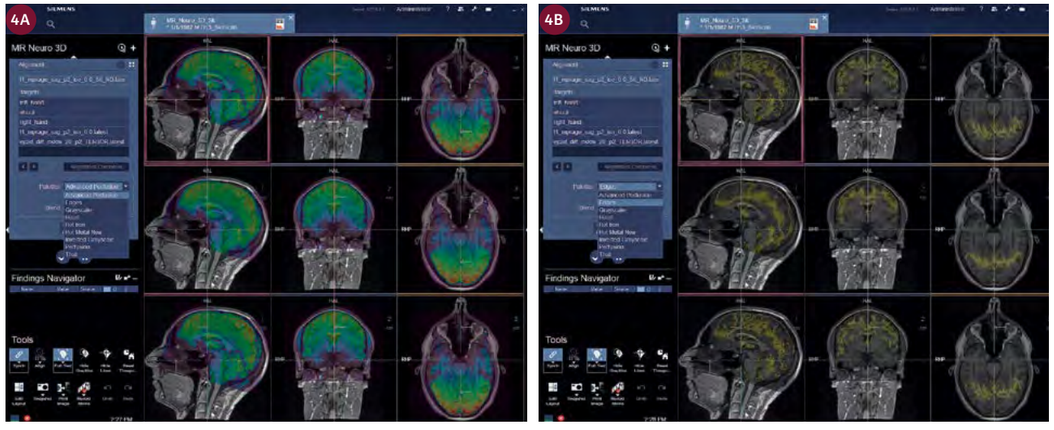

4 Dropdown menu for different overlay palettes in the Control Area on the far left of the screen. These different overlay palettes can aid assessment of co-registration accuracy. The different examples shown are **(4A)** Advanced Perfusion (default) and **(4B)** Edges.

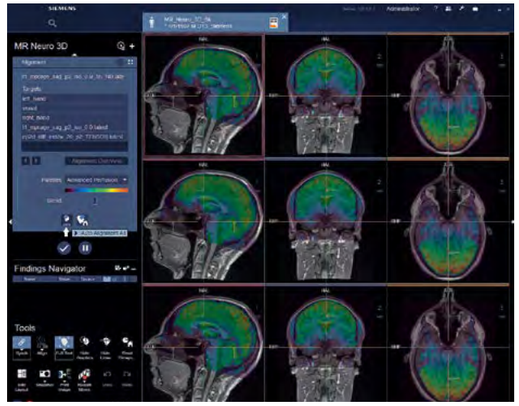

5 Automatic alignment for all series to the reference series is performed by clicking on the 'Auto Alignment All' button (indicated with arrow).

Image alignment can be performed automatically or manually. First, click on the 'Auto Alignment All' button in the Control Area (Fig. 5, indicated by arrow) in order to perform automatic alignment for all series simultaneously. The algorithm works with an iterative approach: Every time you click on the 'registration' button, the registration is further improved until a steady state is reached (Fig. 6).

We recommend the individual verification of each and every series. To do this, click on the series in the 'target images'. This opens the single series in a dedicated 3D MPR view with the functional data overlaid on the reference scan. For BOLD acquisitions, the raw series is also displayed together with motion correction graphs (rotation and translation) (Fig. 7).

For each segment, scroll through the slices to check the alignment. You can scroll using three alternatives:

1. using the mouse wheel,
2. moving the mouse up and down while pressing the right mouse button,
3. pressing the keyboard arrows 'up' and 'down'.

For the BOLD raw series, you can additionally scroll through time using two alternatives:

1. moving the mouse left and right while pressing the right mouse button,
2. pressing the keyboard arrows 'left' and 'right'.

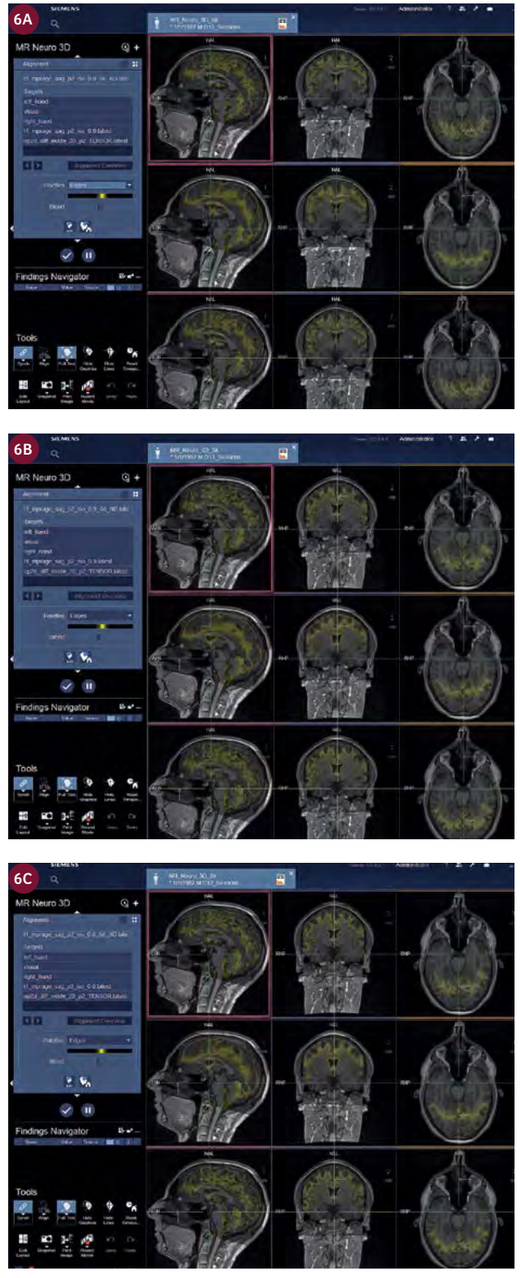

6 Improvements to the automatic coregistration with several iterations. **(6A)** Prior to application of alignment algorithm, **(6B)** after one iteration, **(6C)** after three iterations.

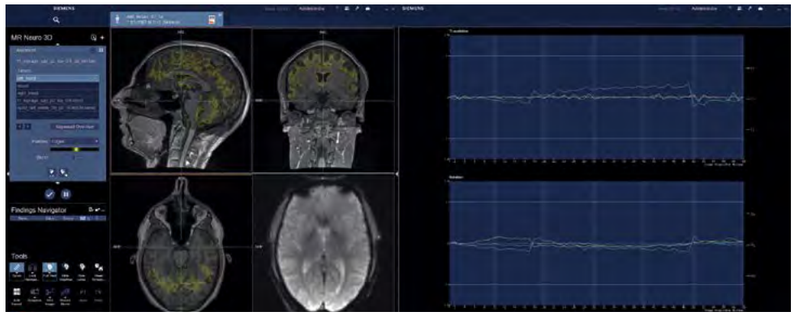

7 Verification of the alignment of a single series in a dedicated display.

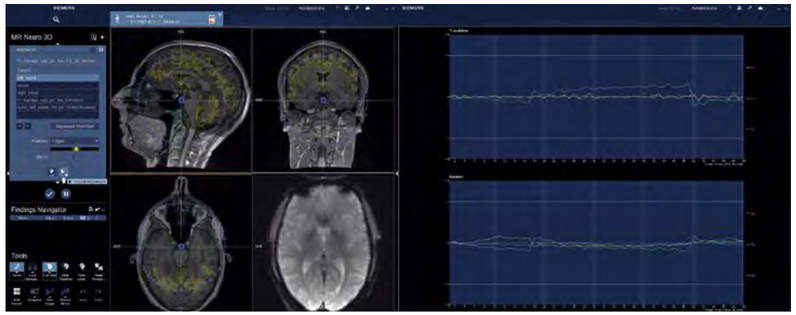

8 Manual alignment is activated by pressing the 'Visual Alignment' button which triggers the appearance of a compass guide.

To modify the alignment, click on the 'Visual Alignment' button in the Control Area (Fig. 8, indicated by arrow). This opens a compass guide in the MPR segments.

For translation: Position the cursor in the desired MPR segment and drag the overlay using the left mouse button.

For rotation: Position the cursor over the compass in the desired MPR segment. The compass changes to white and you can drag it clockwise or counter clockwise using the left mouse button. The center of the rotation can be adjusted by dragging the center of the compass.

Many users find the 'Edges' palette useful for the verification of the alignment. After you have performed the manual alignment, deactivate the 'Visual Alignment' button to avoid any further accidental modifications.

Repeat this step for all the other series: Click in the 'target images' list to select the next series. To go back to the overview display, click on the 'Alignment Overview' button. When all the series are properly registered, processing and visualization can then be performed.

Third step: fMRI

Click on the 'fMRI' step to perform visualization of BOLD activation areas. All BOLD paradigms are presented in the 'function' list and the corresponding activation maps are displayed overlaid on the reference scan in a 3D MPR view and as a volume rendered image (Fig. 9).

The visualization and processing tools offer the following functionalities:

- Hide or display dedicated activation maps by clicking the 'eye' icon in the function list.

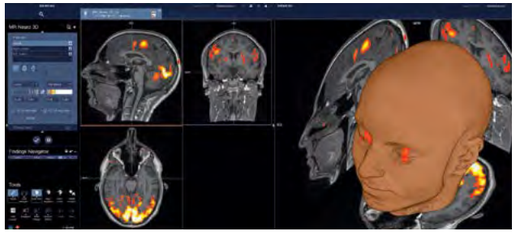

9 Visualization of BOLD activation maps within the fMRI step.

10 **(10A)** Clip plane functionality to better visualize BOLD activations within the VRT segment.
(10B) fMRI activations as displayed on a gray-scale VRT-like visualization within the VRT segment.

- Assignment of color palettes to the activation maps. Different modes are available:
  - 'Individual Mode' to assign different color palettes to each activation map.
  - 'Uniform Mode' to assign the same color palette to all activation maps.
  - 'Highlight Mode' to assign a specific color palette to the activation map resulting from a primary task and another color palette to the secondary tasks.
- Adjustment of statistical threshold levels
- Optional interpolation and specification of cluster size. This can be found in the 'function properties' menu (bottom right corner of each MPR segment)
- In the VRT segment:
  - Clip plane for visualization of the BOLD activation specific to a plane (upper left corner). Several planes can be activated simultaneously.
  - Split plane for visualization of BOLD activation in the whole imaging volume up to the specified anatomical plane (upper left corner)
  - Brain mask for skull removal to better visualize brain surface cortical structures
- Synchronization of MPR and VRT segments: Clicking on the VRT automatically brings the MPR segments to the corresponding reference point.

First, examine the activated areas for the different tasks in the MPR segments. If necessary, adjust the statistical threshold values for each paradigm. Highlight the corresponding paradigm with a click in the function list and adjust the threshold located below (slider bar or keyboard input). The colors of each activation map can be individually specified by using the drop down menus of available color palettes. Within the VRT segment, activate the clip plane and split plane functionalities to help 3D visualization (Fig. 10A). A list of important keyboard shortcuts is present in Appendix A. To translate a plane, position the cursor close to the plane, press and hold the right mouse button and move the mouse in the desired direction. To rotate a plane, position the cursor close to the spheres on its border, press and hold the left mouse button and move the mouse in the desired direction.

Should a VRT-like gray-scale visualization be preferred (Fig. 10B), please do these following steps:

1. Click on "Fused Volume Renderer" (lower left corner) to deactivate the VRT.

2. Click on the wrench within “Orthogonal MPR” (lower left corner) and click on “Orthogonal MPR Properties”. This will activate a pop-up window. Activate the “In-situ Display” option.
3. To translate or rotate the different planes within the VRT segment, simply modify the reference lines within the MPR segments.

Fourth step: Time Course Evaluation

To perform a quality check of the activation maps, click on the ‘Time Course Evaluation’ step to analyze signal-time curves.

Select the desired paradigm in the ‘function list’ by clicking on the corresponding white box. An eye icon will appear and the corresponding activation map is displayed. Time-course analysis can be performed for individual voxels or volumes of interest. Select your desired tool by clicking on the appropriate icon ‘fMRI voxel’ or ‘fMRI VOI’ within the control area or in the upper right corner of each MPR segment (Fig. 11A, highlighted with squares).

For single voxel analysis, select the ‘fMRI voxel’ tool and click on the appropriate voxels of interest within the MPR segments. Every click will create a voxel of a different color and the corresponding signal-time curve is displayed with the same color in the time-course segment. To modify the position of a voxel, first deactivate the ‘fMRI voxel’ tool and relocate the voxel with drag and drop.

For volume analysis, select the ‘fMRI VOI’ tool and draw a volume over an activated area of interest (Fig. 11B). By default, the VOI is restricted to the voxels which are activated above threshold. You can change this behavior with a right click on the VOI and de-selection of ‘shrink to activation’ option.

To delete any voxel or volume of interest, select the corresponding object and choose the ‘delete measurement’ option with a right mouse click.

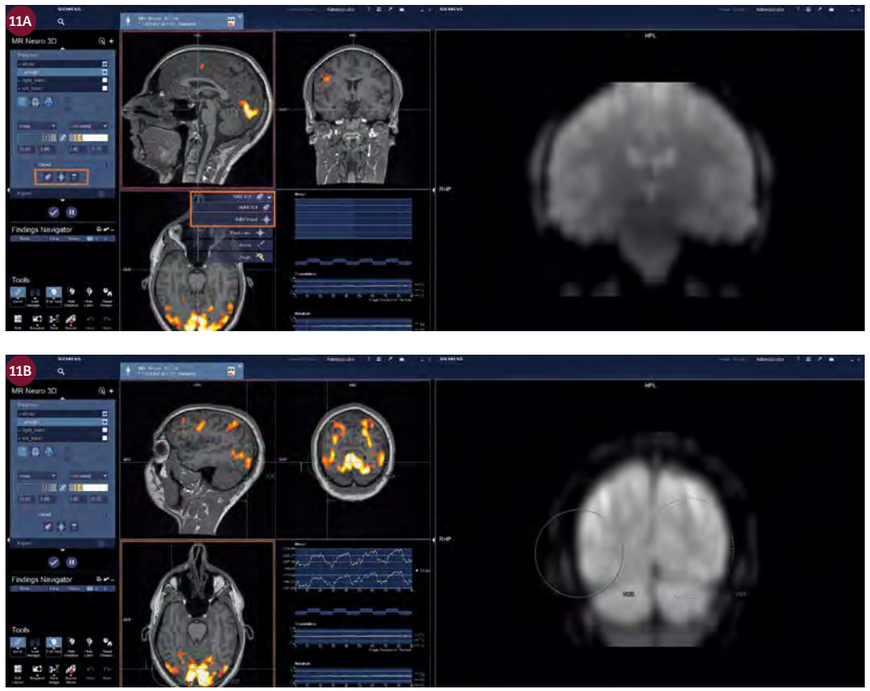

11 **(11A)** Options for tool selection. **(11B)** Display of activation maps with signal-time curves in the Time Course Evaluation step.

12

Fifth step: Tractography

For visualization of diffusion tracts, click on the ‘Tractography’ step. Tractography data for the complete imaging volume have been automatically generated. They are displayed overlaid on the reference scan in a 3D MPR view and as a volume rendered image (Fig. 12). If you have performed the fMRI step as described above, the tractography data is simply added to the currently available MPRs and VRT.

The tracts are generated using a deterministic approach with the FACT algorithm (Fiber Assignment by Continuous Tracking) [4]. Different parameters can be specified, for example seed points and angle threshold (see Appendix B). Specific settings can be saved to be applied for the initial automated whole volume tractography as well as for the more precise generation of refined tracts. Default settings are provided. You can save your own settings, for this, please refer to the user manual.

The whole volume tractography may be useful for the immediate visualization of tracts displacement in the presence of tumors (Fig. 13).

The whole volume tractography can be interactively refined through different options: volume of interest, volume of interest using activated voxels, planes, or logical combination (AND, OR ...) of these (Fig. 14):

1. Tractography VOI: selective visualization of tracts which traverses the VOI.
2. Tractography VOI (Shrink to activation): selective visualization of tracts within the vicinity of fMRI activated voxels in the VOI.
3. Tractography Plane: selective visualization of tracts which crosses the set plane.

As there are many different approaches for tractography analysis, this article will focus on two use cases.

1. Visualization of the arcuate fasciculus

Click on the ‘Interactive Mode’ icon (Fig. 14).

Visualization of this very important tract can be done by placing a Tractography VOI in the inferior frontal lobe or in the temporal lobe. However, in cases of lesions or tumors potentially displacing important functional language regions, it may be helpful to use fMRI activation voxels to guide placement of the VOI.

Select the ‘Tractography VOI’ or ‘Tractography VOI (Shrink to activation)’ by clicking on the corresponding icon. Draw the VOI in any MPR segment. This creates a VOI labeled ‘VOI_1’ (Fig. 15B). The color of the VOI reflects its function: green for a Tractography VOI, purple for a Tractography VOI (Shrink to activation). You can move the VOI by dragging and moving it in the different MPR segments. The VRT is updated in real time.

In the VRT segment, use the clip planes and split planes as described in the fMRI step. Once you are satisfied with the rendering, hide the seed volumes, if desired, with a right click and further selection of ‘Hide seed points’. Save your result by clicking the ‘Create and Save Diffusion Tract Bundle’ icon in the control area. This generates the finalized tract bundle using the settings highlighted in the drop down menu ‘Settings’ (Fig. 15C).

2. Visualization of the connecting pathways for the visual system

Click on the ‘Interactive Mode’ icon.

First, select the ‘Tractography VOI (Shrink to activation)’ by clicking on the corresponding icon and draw a VOI encompassing the visual cortex on the axial plane. This creates a purple VOI labeled ‘VOI_1’ (Fig. 16B). Manipulate the shape of the VOI in the different planes to capture the visual cortex selectively for the left or right hemisphere.

Second, select the ‘Tractography VOI’ and draw a VOI next to the optic chiasm, usually best identified on the axial plane. This creates a green VOI labeled ‘VOI_2’ (Fig. 16C). By default, the logical combination ‘A AND B’ is selected (Fig. 16C, arrow), and therefore only the tracts going through the VOI_1 and the VOI_2 are displayed. You can change the position and shape of both VOIs in all planes in order to best capture the connecting pathways. Use the clip planes and split planes in the VRT segment to fine-tune the rendering.

Save your result by clicking the 'Create and Save Diffusion Tract Bundle' icon in the control area. This generates the finalized tract bundle using the settings highlighted in the drop down menu 'Settings'.

Should a VRT-like gray-scale visualization be preferred (Figs. 17A, B), please refer to the end of the fMRI section for the necessary steps.

Export:

To export the processing results, a dedicated 'Export' step is available. Please refer to the user manual.

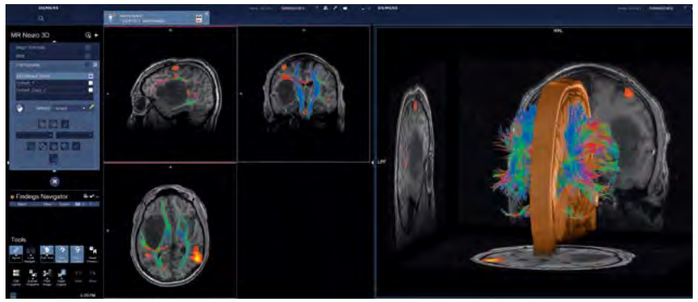

13 Visualization of whole volume tractography within the Tractography step (two clip planes have been used).

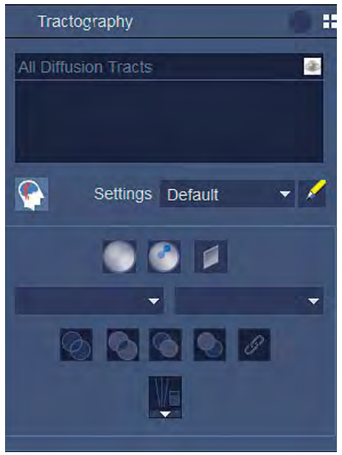

14

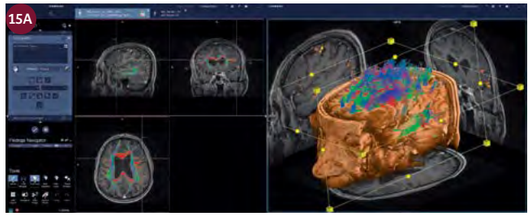

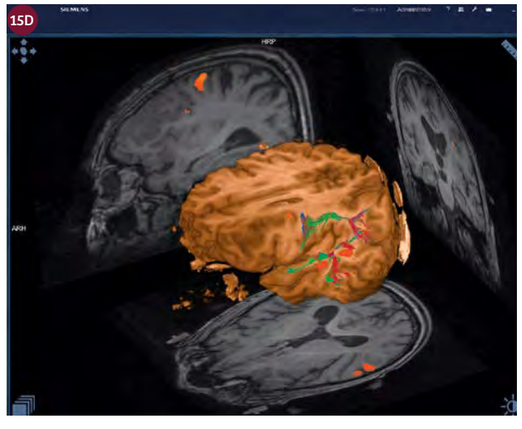

15 Visualization of the arcuate fasciculus in the tractography step. **(15A)** Initial whole brain tractography. **(15B)** Refined tracts after positioning of the VOI. **(15C)** Rendered Tracts with defined settings. **(15D)** Additional rendering with skull stripping.

16 Visualization of the connecting pathways for the visual system in the tractography step. **(16A)** Initial whole brain tractography. **(16B)** After fMRI VOI. **(16C)** After VOI 2, only tracts going through 1 and 2 are displayed. **(16D)** Rendered Tracts with defined settings.

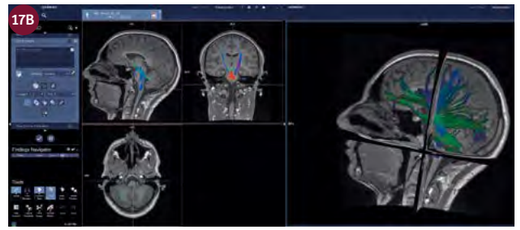

17 Tractography displayed on a VRT-like gray-scale visualization with single seed point **(17A)** and multiple seed points **(17B)**.

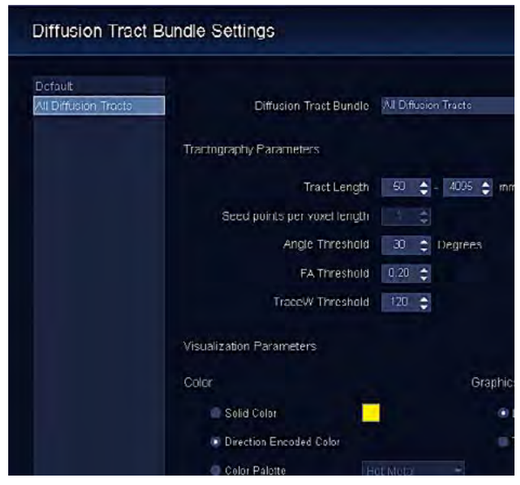

Appendix B2

Clip Planes	
Action	**Keyboard Shortcut**
Left Clip Plane	Shift+ L
Right Clip Plane	Shift + R
Head (Dorsal) Clip Plane	Shift + H
Foot (Ventral) Clip Plane	Shift + F
Anterior Clip Plane	Shift + A
Posterior Clip Plane	Shift + P
Home all Clip Planes (Orientation Reset)	Shift + 0 (zero)
Show/Hide all Clip Planes	Shift + 1
Orthogonal MPRs	
Action	**Keyboard Shortcut**
Action Increase offset of orthogonal MPRs	Shift + ↑
Decrease offset of orthogonal MPRs	Shift + ↓
Show/Hide orthogonal MPR frames	Shift + 2
Show/Hide orthogonal planes	Shift + 3
Others	
Action	**Keyboard Shortcut**
Show/Hide VRT	Shift + 4
Show/Hide Split Plane	Shift + 5
Toggle between Clip Plane and Split Plane	Shift + s

Appendix A: Important keyboard shortcuts for *syngo*.MR Neuro 3D

Tract Length	
larger range = more tracts	**smaller range = less tracts**
It is defined as the length of the tracts that will be shown as tracts.	
Seed points per voxel length	
smaller value = less tracts	**higher value = more tracts**
value 1 = 1^3 = tract, value 2 = 2^3 = 8 tracts, value 3 = 3^3 = 27 tracts ...	
Angle Threshold	
smaller value = less tracts	**higher value = more tracts**
Fiber tracking stops at a certain position if the resulting fiber tract would bend by more than "Angle Threshold" degrees at this position.	
FA Threshold	
smaller value = more tracts	**higher value = less tracts**
It is defined as the degree of Anisotropy: 0 = low anisotropy, 1 = very strong anisotropy; typical values are between 0.05 and 0.2. Fiber tracking stops at voxel postion with an FA value lower than the given FA threshold.	
TraceW Threshold	
smaller value = more tracts	**higher value = less tracts**
The trace-weighted image is obtained by taking the average of the individual diffusion weighted images from the DTI scan. This generates an image comparable to orthogonal DWI, yet is derived from the full diffusion sampling. The TraceW threshold value is set to 120 as default based on internal experience.	

Appendix B1

References

[1]Benzinger TL, McKinstry III RC, Chen CI, Priatna A. Clinical applications of Diffusion Tensor Imaging. MAGNETOM Flash. 2007;37:74-86.

[2]Pillai JJ, Zaca D. Case series: Presurgical planning with fMRI/DTI. MAGNETOM Flash. 2011; 48: 14-17.

[3]Bartsch AJ. Simultaneous Multi-Slice (SMS) Imaging for Pre-Surgical BOLD fMRI and Diffusion Tractography: Case Illustrations. MAGNETOM Flash Special Simultaneous Multi-Slice Supplement. 2015; 63: 58-64.

[4]Mori S, van Zijl PCM. Fiber tracking: Principles and strategies—A technical review. NMR in Biomedicine. 2002;15:468–480.

Contacts
Lisa Chuah, Ph.D.
lisa.chuah@siemens-healthineers.com

Julien Gervais
Julien.Gervais@siemens-healthineers.com

RESOLVE: A Powerful Tool for Imaging the Pediatric Spine

Laura L. Hayes[1]; David A. Porter[2]; Richard A. Jones[1,3]; Susan Palasis[1]; J. Damien Grattan-Smith[1]
[1]Department of Radiology, Children's Healthcare of Atlanta at Scottish Rite, Atlanta, GA, USA
[2]Siemens AG, Healthcare Sector, Erlangen, Germany
[3]Department of Radiology, Emory University, Atlanta, GA, USA

Introduction

Diffusion-weighted imaging (DWI) is one of the most powerful imaging tools available to radiologists today. DWI of the brain revolutionized neuroimaging when it was introduced in the mid-1990s. Until recently, clinically useful DWI of the spine has not been possible using standard single shot EPI techniques due to susceptibility artifacts and the need for higher spatial resolution. The novel 2D-navigator-corrected readout-segmented EPI sequence known as RESOLVE (REadout Segmentation Of Long Variable Echo trains) can obtain images with higher spatial resolution and reduced distortion of the spine related to susceptibility, pulsations, respiration, and motion [1]. This is especially helpful when imaging children where the small size of their spine/cord, prominent CSF and arterial pulsations, and higher pulse and respiratory rates compared to adults can pose significant limitations on the quality of the images obtained. Motion artifacts that notoriously plague every facet of pediatric imaging are also reduced with RESOLVE. RESOLVE is proving to be a valuable sequence for the evaluation of numerous pathological states of the pediatric spine.

Sequence description

RESOLVE [1, 2] is a multi-shot, diffusion-weighted sequence, which is based on the readout-segmented echo-planar imaging (rs-EPI) sampling scheme [3]. The sequence incorporates a 2D non-linear correction for motion-induced phase errors [4] and supports iPAT using GRAPPA. The rs-EPI method only samples a subset of raw data points in the readout direction, making it possible to use a very short EPI echo spacing with a typical value of 360 µs. This is significantly shorter than the echo spacing used for single-shot EPI (ss-EPI), which reduces the level of susceptibility and blurring artifacts and makes it possible to acquire images with a higher spatial resolution.

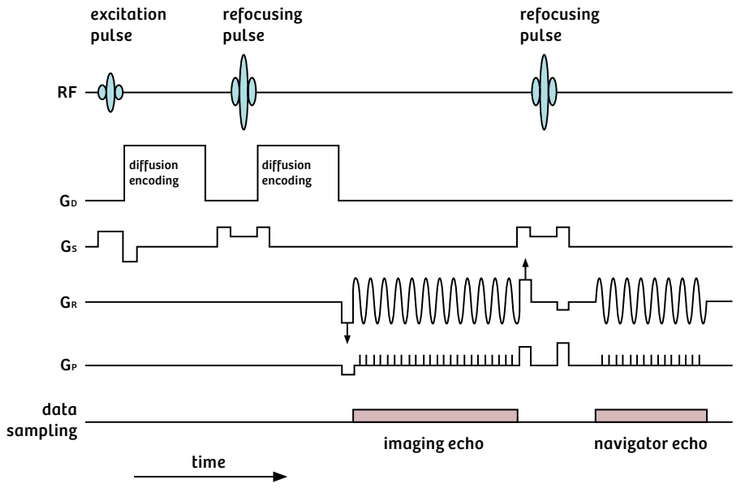

1 Pulse diagram for the RESOLVE sequence. The figure shows radiofrequency (RF) pulses and magnetic field gradient pulses for diffusion-encoding (G_D) and for spatial encoding along slice (G_S), readout (G_R) and phase-encoding (G_P) directions. The gradients with the ↑ symbol have an amplitude that is varied at each spin excitation to control an offset in the k_x direction, so that a different readout segment is sampled by the imaging echo at each shot. In contrast, the navigator echo always samples a fixed 2D region at the centre of *k*-space.

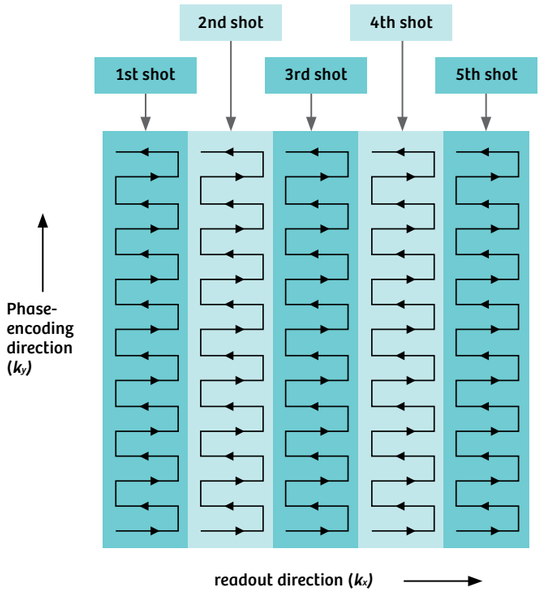

2 Diagram showing the *k*-space sampling scheme used for the imaging echo in the RESOLVE sequence. In this example, a five shot acquisition is used which divides *k*-space into five segments along the readout direction. Within each shot, an EPI readout is used to sample all phase-encoding (k_y) points and a subset of readout (k_x) points. The second (navigator) echo is always used to sample the central readout segment, providing 2D reference data from the center of *k*-space, which are used to perform a non-linear phase correction.

In general, multi-shot, diffusion-weighted sequences are susceptible to image artifacts that arise from motion during the diffusion preparation, resulting in shot-to-shot phase errors. Navigator phase correction [5] can address this problem by sampling data from the center of k-space at each shot; these data are then used to monitor and correct the phase variation between shots. CSF pulsation around the brain and spinal cord causes non-rigid-body motion, resulting in a 2D non-linear phase variation in image space, which requires 2D navigator data to perform a correction [4]. The rs-EPI sampling scheme is particularly well-suited to this type of correction because, unlike the more commonly used interleaved EPI sequence, the Nyquist sampling condition is fulfilled at each shot and there are no aliased signal contributions in the image domain to interfere with the phase correction procedure.

As shown in figure 1, following a spin excitation and diffusion preparation, the RESOLVE sequence uses two EPI readouts to acquire data from two spin echoes respectively at each shot. The first spin echo is used to sample a region of k-space, known as a readout segment, in which contiguous data samples are collected for all phase-encoding (ky) points and for a subset of readout (kx) points. A variable pre-phase gradient is applied along the readout (x) axis before the EPI readout to control an offset along kx, so that a different readout segment is sampled at each shot. As shown in the k-space trajectory in figure 2, data from multiple readout segments are combined to provide full k-space coverage; typical protocols require 5, 7 or 9 shots to acquire the full data set, depending on the spatial resolution. The second spin echo shown in figure 1 is used to sample the central readout segment at each shot, thereby providing data for the 2D non-linear navigator correction. This is performed as a complex multiplication in the image domain before the data from the individual segments are combined to form the final image.

To further reduce the effect of motion-induced phase errors, the RESOLVE sequence uses a reacquisition scheme [6], which has been adapted to the case of a 2D navigator [7]. This ensures that readout segments with severe phase errors, which cannot be removed by the 2D navigator correction, are discarded and replaced by reacquired data.

Currently useful applications:

1. Tumor

a. Intradural

i. Drop metastases

DWI of the brain has revolutionized the sensitivity of MR in diagnosis, staging, and follow-up of children with central nervous system (CNS) tumors [8]. Likewise DWI of the spine is demonstrating the ability to reveal spinal disease that may not be visible on conventional MR sequences in children with primary brain tumors [9]

3 2-year-old girl* with ataxia and vomiting found to have a large posterior fossa tumor that restricted diffusion and demonstrated minimal enhancement, consistent with an atypical rhabdoid teratoid tumor (ATRT). Initial MRI scan of the spine: Sagittal T1 post-contrast **(3A)**, ADC map **(3B)**, isotropic DWI **(3C)**, sagital T2 **(3D)**, and axial T1 post-contrast image at the level of interest **(3E)** demonstrate the lack of any abnormal signal or enhancement **(3A, D, E)** at the location of the nodular diffusion abnormality at the dorsal aspect of the thoracic cord **(3B, C)**.

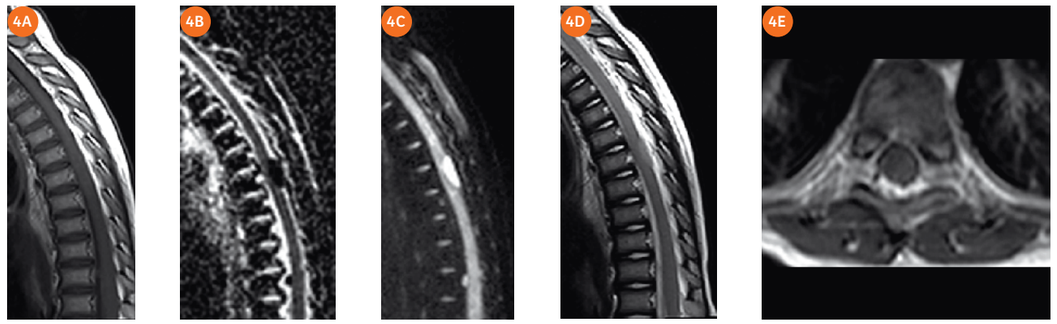

4 Follow up scan two months later. Sagittal T1 post-contrast **(4A)**, ADC map **(4B)**, isotropic DWI **(4C)**, sagittal T2 **(4D)**, and axial T1 post-contrast image at the level of interest **(4E)** demonstrate interval increase in the size of the previously visualized nodular diffusion abnormality, now also seen on the T2 image as well. Another nodular diffusion abnormality along the ventral aspect of the lower thoracic cord is now clearly visible. Note the continued lack of conspicuity on the T1 post-contrast images **(4A, E)**.

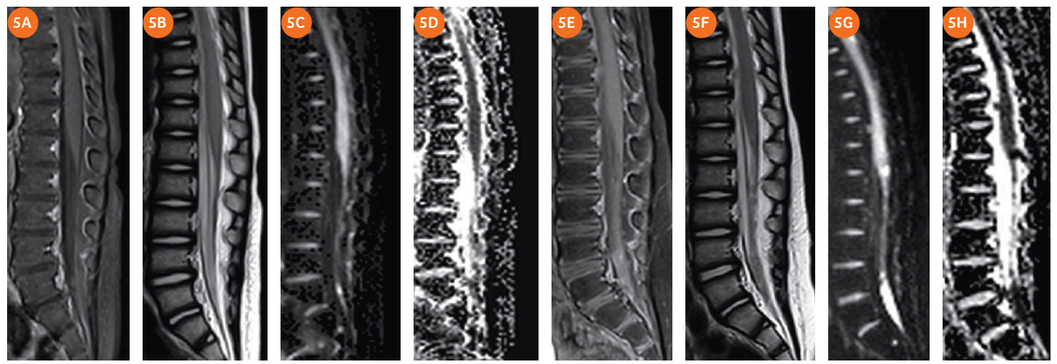

5 Images of the thoracolumbar spine from initial scan **(5A–D)** and follow-up scan two months later **(5E–H)**. Initially negative T1 post-contrast **(5A)** and T2 image **(5B)** with possible tiny, nodular diffusion abnormality along the distal cauda equina on isotropic DWI **(5C)** and ADC map **(5D)**. Follow-up T1 post-contrast image demonstrates enhancement within the distal thecal sac **(5E)**; T2 image demonstrates nodularity along the cauda equina and within the distal thecal sac **(5F)**; isotropic DWI **(5G)** and ADC map **(5H)** demonstrate nodular and clumpy areas of restricted diffusion consistent with drop metastases.

(Figs. 3–5). Many of the primary CNS tumors that metastasize to the spine have a hypercellular tumor matrix. Primitive neuro-ectodermal tumors (PNETs) consist of small, round cells with scanty cytoplasm and have an extremely high cellular density with a high nuclear-to-cytoplasmic index. The total water content of these tumors is low, and their densely packed cellular nature results in restricted diffusion. The physical characteristics of these tumors render them sensitive to detection by DWI. Due to their high grade and often high degree of necrosis, they may not exhibit enhancement on conventional imaging sequences that currently are the standard imaging method for detection of drop metastasis. Medulloblastoma, a PNET, is the second most common neoplasm of the CNS in children and has pathologic features that make it optimal for evaluation with DWI. Other CNS tumors that can restrict diffusion and spread to the spine include other PNETs such as atypical teratoid rhabdoid tumor (ATRT), as well as ependymoma, glioblastoma multiforme, germinoma, and choroid plexus carcinoma.

ii. Primary cord tumor

Just as in the brain, DWI is helpful in narrowing the differential diagnosis of primary spinal tumors (Fig. 6). Diffusion tensor imaging (DTI) can be used to visualize ordered white matter tracts of the spinal cord in an effort to further characterize a mass. It is helpful to determine whether the lesion displaces the tracts or infiltrates between them. Identification of white matter tracts can ultimately assist in surgical planning as well [10].

iii. Epidermoid

Restricted diffusion within a solitary intradural cyst is essentially pathognomonic for an epidermoid cyst (Fig. 7). The restricted diffusion within these cysts is related to their squamous epithelial contents. Epidermoids are often congenital and can be related to tethered cords, a common indication for spine MRI in children. Arachnoid cysts and epidermoid cysts can be easily differentiated with DWI [11].

b. Extradural

i. Vertebral/paravertebral/ metastatic tumors

As previously discussed, spine DWI is particularly well-suited to pediatric oncologic imaging due to the high frequency of densely cellular tumors that occur in children. These tumors can be found both intra- and extradurally within the spine. Pediatric extradural tumors that lend themselves to DWI detection include neuroblastoma, leukemia, lymphoma, rhabdomyosarcoma, and Ewing sarcoma (Fig. 8). The unifying pathologic feature of these tumors is that they are comprised of small, round, blue cells. In the case of primary vertebral Ewing sarcoma, DWI not only assists with tumor detection but also in differentiation from other vertebral lesions that can have a similar appearance on conventional imaging sequences such as eosinophilic granuloma and chordoma (Fig. 9).

Diffusion-weighted imaging can also be a useful tool for distinguishing acute benign osteoporotic from malignant vertebral compression fractures. Increased water motion is typically present in post-traumatic benign compression fractures resulting in low or iso-intense signal on DWI and high ADC values on ADC maps [10]. In contrast, pathologic compression fractures related to densely cellular tumors such as lymphoma have restricted diffusion with hyperintensity on DWI and hypointensity on ADC maps [13] (Fig. 10).

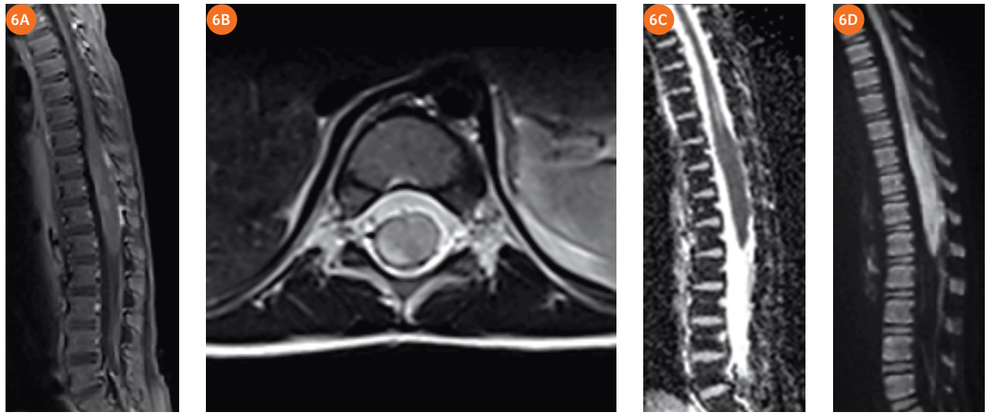

6 2-year-old boy* with limping and back pain. Sagittal T1 post-contrast **(6A)** and axial T2 images **(6B)** demonstrate an intramedullary mass involving the conus medullaris. There is mild enhancement of the lesion, and the mass is iso- to hyperintense on T2. ADC map **(6C)** reveals isointensity of the mass with the normal cord, corresponding to an iso- to hyperintense appearance on the isotropic DWI image **(6D)**. This excludes a densely cellular lesion such as PNET, and is consistent with a lower grade lesion such as a diffuse leptomeningeal neuroepithelial tumor (DLNT) as in this case.

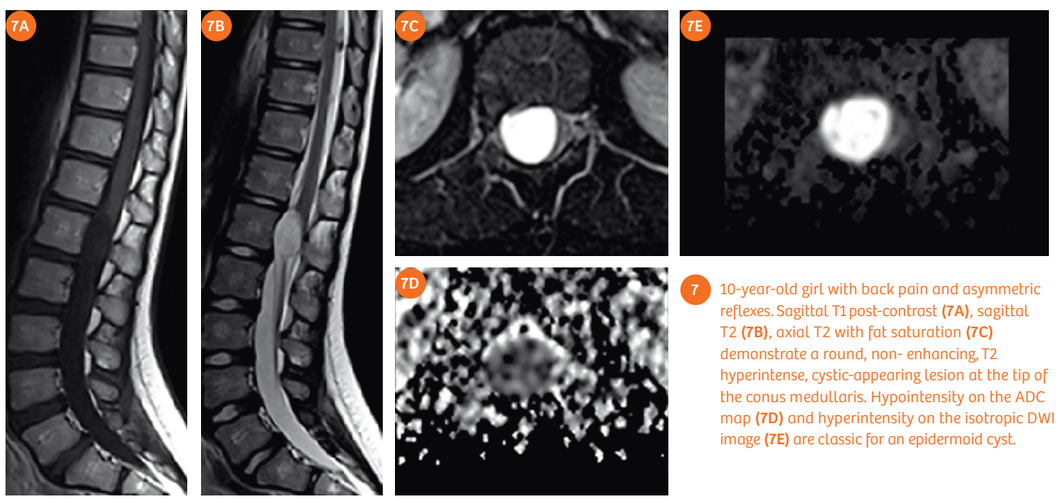

7 10-year-old girl with back pain and asymmetric reflexes. Sagittal T1 post-contrast **(7A)**, sagittal T2 **(7B)**, axial T2 with fat saturation **(7C)** demonstrate a round, non- enhancing, T2 hyperintense, cystic-appearing lesion at the tip of the conus medullaris. Hypointensity on the ADC map **(7D)** and hyperintensity on the isotropic DWI image **(7E)** are classic for an epidermoid cyst.

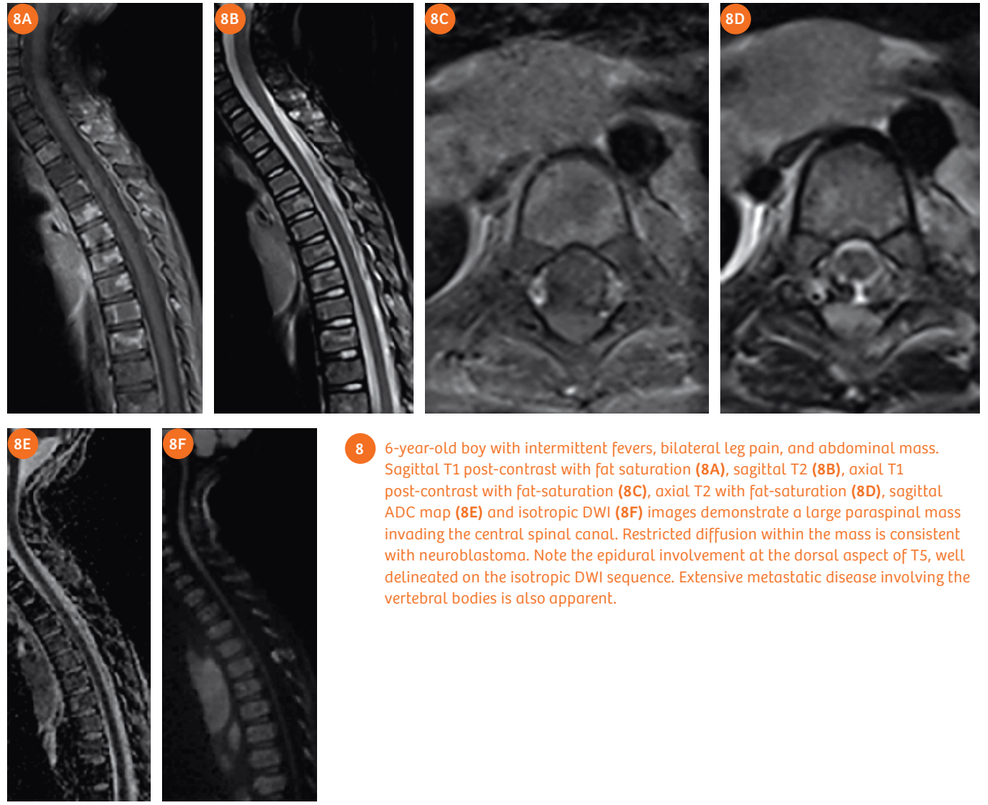

8 6-year-old boy with intermittent fevers, bilateral leg pain, and abdominal mass. Sagittal T1 post-contrast with fat saturation **(8A)**, sagittal T2 **(8B)**, axial T1 post-contrast with fat-saturation **(8C)**, axial T2 with fat-saturation **(8D)**, sagittal ADC map **(8E)** and isotropic DWI **(8F)** images demonstrate a large paraspinal mass invading the central spinal canal. Restricted diffusion within the mass is consistent with neuroblastoma. Note the epidural involvement at the dorsal aspect of T5, well delineated on the isotropic DWI sequence. Extensive metastatic disease involving the vertebral bodies is also apparent.

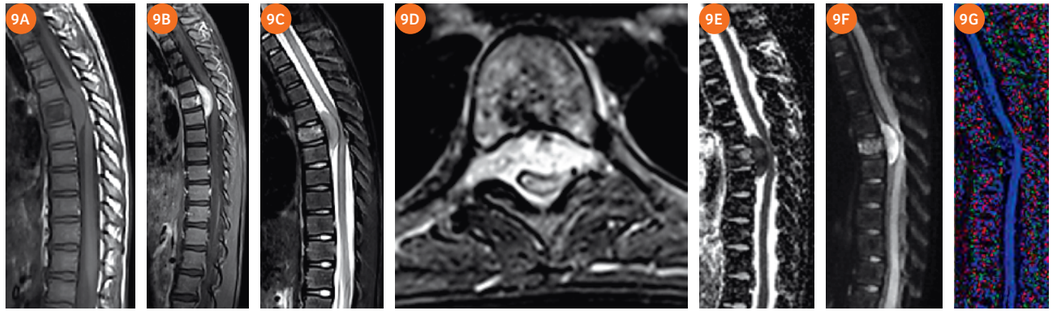

9 8-year-old boy with ataxia. Sagittal pre-contrast T1 **(9A)** and post-contrast T1 with fat saturation **(9B)**, sagittal and axial T2 with fat saturation **(9C, D)**, sagittal ADC **(9E)**, isotropic DWI **(9F)**, and color FA (fractional anisotropy) map **(9G)** reveal a large, enhancing epidural mass involving the T6 vertebral body producing cord compression. Restricted diffusion in the mass **(9E, F)** is typical for Ewing sarcoma.

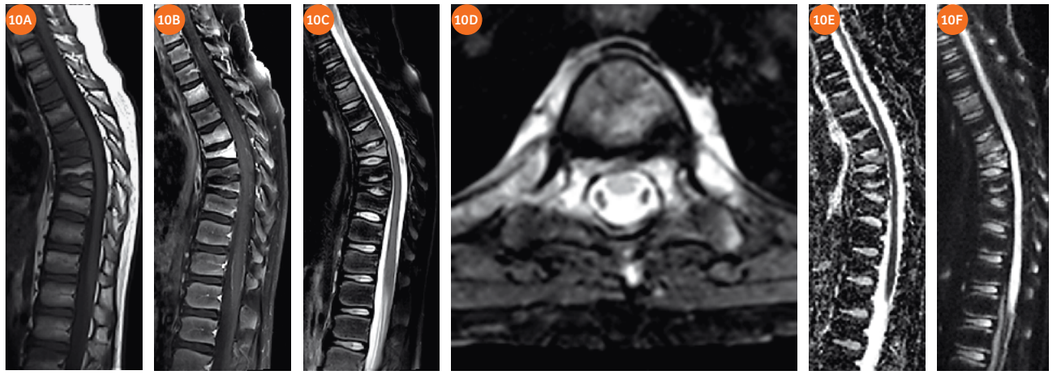

10 10-year-old boy with back pain. Sagittal pre-contrast T1 **(10A)**, post-contrast T1 with fat saturation **(10B)**, sagittal and axial T2 with fat saturation **(10C, D)**, ADC map **(10E)** and isotropic DWI **(10F)** images demonstrate multilevel compression fractures with enhancement of the involved vertebral bodies, low signal on ADC maps, and marked hyperintensity on DWI. Findings are consistent with leukemia/lymphoma. Chronic relapsing multifocal osteomyelitis is one differential consideration.

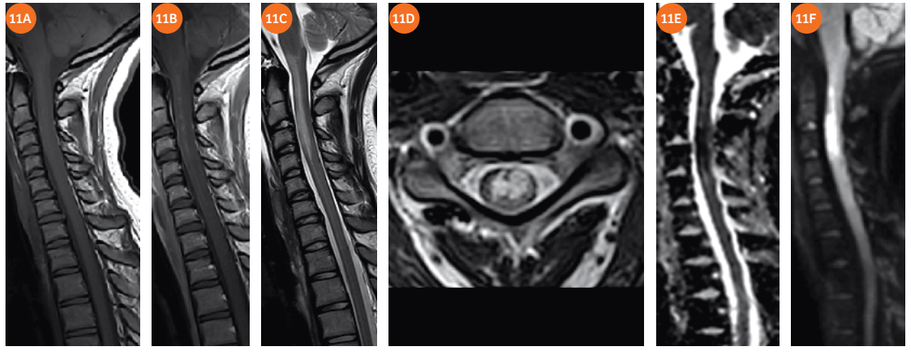

11 17-year-old girl with acute onset of neck pain followed by flaccid tetraparesis. Sagittal pre- and post-contrast T1 **(11A, B)** and sagittal and axial T2 **(11C, D)** images demonstrate intrinsic T2 hyperintensity within the cord from the level of the cervicomedullary junction to the level of C4. There is corresponding hypointensity with minimal enhancement on T1. Sagittal ADC map **(11E)** demonstrates marked hypointensity within the cord at these levels, and isotropic DWI image **(11F)** demonstrates hyperintensity consistent with acute cord infarction.

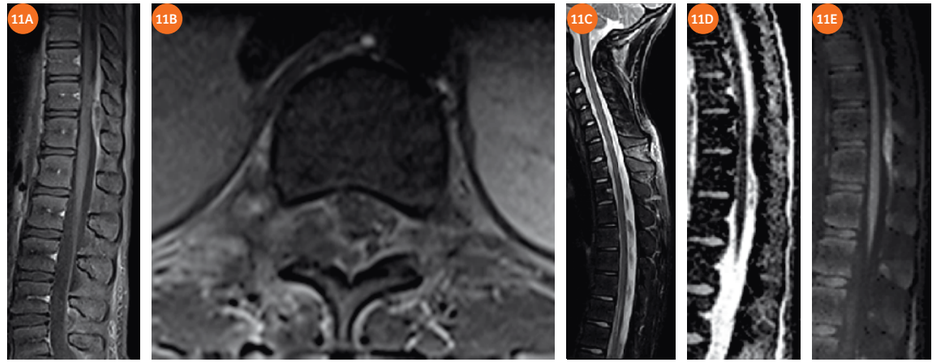

12 12-year-old girl with back pain, fever, and CSF pleocytosis. Sagittal and axial T1 post-contrast with fat saturation **(12A, B)**, sagittal T2 with fat saturation **(12C)**, sagittal ADC map **(12D)**, and isotropic DWI **(12E)** images reveal an epidural collection with irregular enhancement with associated paraspinal soft tissue edema. There is corresponding hypointensity on the ADC map with well-defined hyperintensity on isotropic DWI in keeping with restricted diffusion in an abscess.

2. Infarction

DWI is a powerful tool in the identification of spinal cord infarction, sometimes revealing restricted diffusion in the cord even before changes on the T1 or T2-weighted images develop [14]. Spinal cord infarctions in children are rare, but can occur in such settings as spinal arteriovenous malformations (AVMs) and fibrocartilaginous emboli. The latter are caused by retrograde migration of nucleus pulposis from the intervertebral disk into the spinal microcirculation [15]. This is usually caused by a minor physical trauma or a physical effort in conjunction with Valsalva [12]. Acute spinal cord infarcts present with severe pain followed by a rapidly progressive paraplegia/tetraplegia and loss of reflexes. MR images reveal cord swelling, increased T2 signal, and markedly restricted diffusion [16] (Fig. 11). Spinal cord infarcts secondary to fibrocartilaginous emboli can demonstrate loss of expected T2-hyperintensity in the disk and loss of disk height.

DWI can aid in the differentiation of acute infarction from inflammatory conditions such as transverse myelitis, a condition not uncommon in children. While restricted diffusion can be seen with transverse myelitis once vasogenic edema becomes cytotoxic, the ADC values are typically not as low as those seen with acute infarction. Further studies are needed to evaluate these differences.

3. Infection

Infection involving the spine is frequently encountered in children. Osteomyelitis, diskitis, and epidural abscesses are common ailments, caused by hematological seeding of bacteria and often manifested with fever, pain, and/or limp. Abscesses can be surgical emergencies due to their potential for cord compression that requires emergent surgical intervention before permanent cord damage ensues. Prompt and accurate imaging detection is critical, and can be assisted by the use of spine DWI. Both osseous and epidural/intradural abscesses restrict diffusion, appearing markedly hyperintense on isotropic trace images and dark on ADC maps [17]. Polymorphonuclear leukocytes and necrotic debris in abscesses restricts water motion, a characteristic that can help differentiate abscesses from simple or mildly proteinaceous fluid collections. Abscess formation is often more conspicuous on DWI than on conventional images. DWI can also identify the extent of the abscess and assist in identifying multifocal disease that may not otherwise be apparent (Fig. 12).

Future directions

DWI shows promise in the evaluation of numerous pathological states of the pediatric spine. More research is needed in regards to demyelinating disease such as multiple sclerosis and spinal cord trauma such as SCIWORA (Spinal Cord Injury Without Radiographic Abnormality) in an effort to improve lesion detection and contribute to a prompt and accurate prognosis.

Several technical developments could further improve the quality of spine DWI images, specifically the use of coils with larger numbers of elements (which has improved diffusion imaging of the brain in recent years) and the use of multi-band to improve the efficiency of the image acquisition [17, 19]. Work also needs to be done to determine the optimum b-values for spine imaging as a range of values has been used in the literature.

As RESOLVE becomes more readily available in the community, it should serve to revolutionize spine imaging just as DWI did when it was introduced into routine MR imaging of the brain. DWI of the brain is currently standard-of-care in MR imaging, and we expect that DWI of the spine will become part of the standard of care for spine imaging in the near future.

Conclusions

RESOLVE DWI is a powerful imaging tool for evaluation of spinal pathology. Images presented in this article demonstrate that this technique is exquisitely helpful in the work-up of numerous pathological conditions of the spine affecting children, including tumor, infarction, and infection.

*MR scanning has not been established as safe for imaging fetuses and infants less than two years of age. The responsible physician must evaluate the benefits of the MR examination compared to those of other imaging procedures.

References

[1]Porter DA, Heidemann RM. High resolution diffusion weighted imaging using readout segmented echo planar imaging, parallel imaging and a two dimensional navigator based reacquisition. Magn Reson Med 2009;62:468-475.

[2]Porter DA, Mueller E. Multi-shot diffusion-weighted EPI with readout mosaic segmentation and 2D navigator correction. In: Proceedings of the 12th Annual Meeting of ISMRM, Kyoto, Japan, 2004. p442.

[3]Robson MD, Anderson AW, Gore JC. Diffusion-weighted multiple-shot echo planar imaging of humans without navigation. Magn Reson Med 1997; 38:82-88.

[4]Miller KL, Pauly JP. Nonlinear phase correction for navigated diffusion imaging. Magn Reson Med 2003;50:343–353.

[5]Griswold MA, Jakob PM, Heidemann RM, Nittka M, Jellus V, Wang J, Kiefer B, Haase A. GeneRalized Autocalibrating Partially Parallel Acquisitions (GRAPPA). Magn Reson Med 2002;47:1202-1210.

[6]Ordidge RJ, Helpern JA, Qing ZX, Knight RA, Nagesh V. Correction of motional artefacts in diffusion-weighted MR images using navigator echoes. Magn Reson Imag 1994; 12:455-460.

[7]Anderson AW, Gore JC. Analysis and correction of motion artifacts in diffusion weighted imaging. Magn Reson Med 1994;32:379-387.

[8]Nguyen Q, Clemence M, Thornton J, Ordidge RJ, Isotropic diffusion-weighted multishot imaging using automatic reacquisition. In: Proceedings of the 7th Annual Meeting of ISMRM, Philadelphia, USA, 1999. p 559.

[9]Porter DA. 2D-navigator-based re-acquisition for motion artefact suppression in multi-Shot, diffusion-weighted Imaging. In: Proceedings of the 14th Annual Meeting of ISMRM, Seattle, USA, 2006. p1047.

[10]Moffat BA, Chenevert TL, Lawrence TS et al. Functional diffusion map: a noninvasive MRI biomarker for early stratification of clinical brain tumor response. PNAS 2005; 102(15): 5524-5529.

[11]Hayes LL, Jones RA, Palasis S, Aguilera D, Porter DA. Drop metastases to the pediatric spine revealed with diffusion-weighted MR imaging. Pediatr Radiol 2012;42(8): 1009-13.

[12]Tanenbaum LN. Clinical applications of diffusion imaging in the spine. Magn Reson Imaging Clin N Am 2013;21(2): 229-320.

[13]Kukreja K, Manzano G, Ragheb J, Medina LS. Differentiation between pediatric spinal arachnoid cyst and epidermoid-dermoid cysts: is diffusion-weighted MRI useful? Pediatr Radiol 2007;37(6):556-60

[14]Rumpel H, Chong Y, Porter DA, Chan LL. Benign versus metastatic vertebral compression fractures: combined diffusion-weighted MRI and MR spectroscopy aids differentiation. Eur Radiol 2013;23(2):541-50.

[15]Baur A, Stäbler A, Brüning R, Bartl R, Krödel A, Reiser M, Deimling M. Diffusion-weighted MR imaging of bone marrow: differentiation of benign versus pathologic compression fractures. Radiology 1998;207(2):349-56.

[16]Manara R, Calderone M, Severino MS, Citton V, Toldo I, Laverda AM, Sartori S. Spinal cord infarction due to fibrocartilaginous embolism: the role of diffusion weighted imaging and short-tau inversion recovery sequences. J Child Neurol 2010;25(8):1024-8.

[17]Reisner A, Gary MF, Chern JJ, Grattan-Smith JD. Spinal cord infarction following minor trauma in children: fibrocartilaginous embolism as a putative cause. J Neurosurg Pediatr 2013;11(4):445-50.

[18]Tsang BK, Foster E, Kam A, Storey E. Diffusion weighted imaging with trace diffusion weighted imaging, the apparent diffusion coefficient and exponential images in the diagnosis of spinal cord infarction. J Clin Neurosci 2013;20(11): 1630-2.

[19]Eastwood JD, Vollmer RT, Provenzale JM. Diffusion-weighted imaging in a patient with vertebral and epidural abscesses. AJNR 2002;(21): 496-498.

[20]Setsompop K, Gagoski BA, Polimeni JR, Witzel T, Wedeen VJ, Wald LL. Blipped-controlled aliasing in parallel imaging for simultaneous multislice echo planar imaging with reduced g-factor penalty. Magn Reson Med 2012;67:1210–1224.

[21]Frost R, Porter DA, Douaud G, Jezzard P, Miller KL. Reduction of diffusion-weighted readout-segmented EPI scan time using a blipped-CAIPI modification. In: Proceedings of the 20th Annual Meeting of ISMRM, 2012 (abstract 116).

Contact
Laura L. Hayes, M.D.
laura.hayes@choa.org

Perspective—High Potential Impact of Simultaneous Multi-Slice Diffusion Acquisition Strategies on Future Clinical Neuroradiology Practice

Timothy Shepherd, M.D., Ph.D., Assistant Professor, Neuroradiology Section, Department of Radiology, New York University, New York, NY, USA

Diffusion has become a critical component of almost all neuroradiology protocols for the head [1] with potential important roles in spine and neck now being better defined [2, 3]. The most impactful application over the past 25 years has been that diffusion is essential for the diagnosis of acute stroke, a frequent indication for MRI in hospitals throughout the world. Diffusion MRI also helps determine subsequent clinical management decisions in this stroke population [1]. Tissue diffusion properties can be informative for characterizing a variety of other neurological conditions such as peri-operative or drug-related cytotoxic edema, specific tumor diagnoses (e.g. epidermoid) and tumor grading (e.g. lymphoma) [4]. Early mathematical models of diffusion anisotropy that are widely available for clinical use, such as diffusion tensor imaging (DTI), can be used to indirectly assess white matter integrity. DTI can characterize white matter pathology not evident or readily detected with other conventional MRI sequences (e.g. normal-appearing white matter in multiple sclerosis) [5]. DTI data can be used to create tractography estimations for localizing eloquent white matter pathways, such as the arcuate fasciculus, for preoperative surgical planning of anatomic corridors and extent of resection [6].

For current routine clinical imaging, diffusion trace and apparent diffusion coefficient (ADC) maps have proven most efficient and practical—these generally only require 3 or 6 diffusion encoding directions for sufficient accuracy

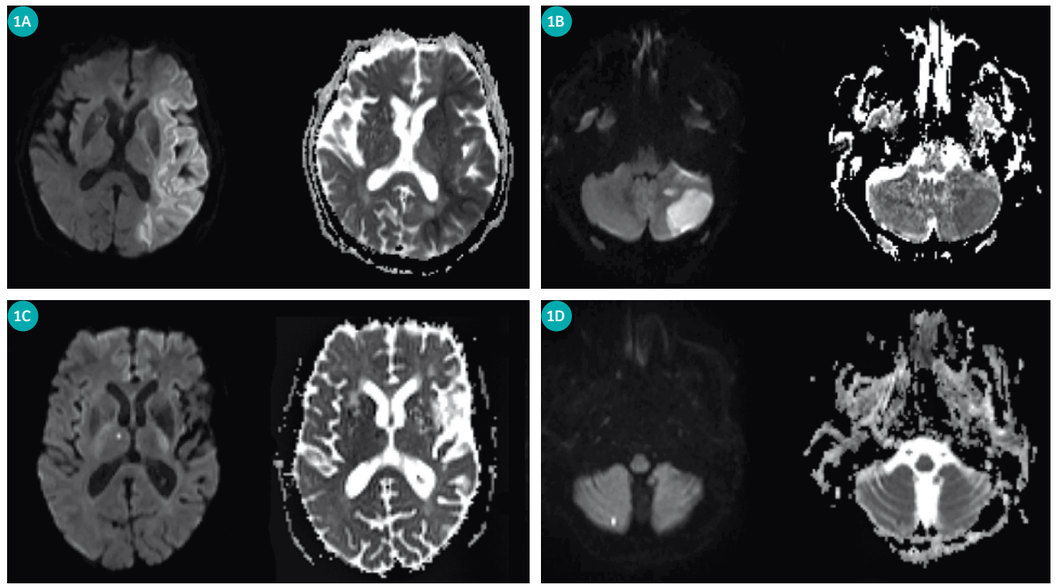

1 Simultaneous multi-slice axial diffusion trace and apparent diffusion coefficient maps in 4 different clinical patients with ischemic infarcts—large left middle cerebral artery territory **(1A)**, left anterior inferior cerebellar territory **(1B)**, right thalamus **(1C)** and right peripheral cerebellar hemisphere **(1D)**. Note while there was a small drop in apparent signal-to-noise in the posterior fossa using SMS diffusion with a 20-channel head & neck coil, large and small, focal posterior fossa infarcts remain well-delineated (panels 1B, D respectively).

during qualitative clinical interpretation. Such scans can be acquired in 2-3 minutes on most modern MRI scanners, whereas DTI for tractography purposes can require 10+ minute acquisitions. More recent acquisition strategies and their companion advanced data analysis techniques developed over the past 15 years provide more information about the tissue environment than diffusion trace or DTI-derived parameters, yet remain relatively limited to application in volunteers and/or selected patient populations under carefully controlled conditions. Such sophisticated techniques require longer acquisitions to increase the number of gradient directions, increase spatial resolution, and/or to acquire images at multiple diffusion-weightings (e.g., b-values of 1500-4000 s/mm2). These acquisitions result in lower signal-to-noise ratio (SNR) that also can require more signal averages. Scan time for such acquisitions is largely affected by image geometry (number of slices and resolution/matrix size), number of averages and diffusion encoding directions [7], but quickly approaches 15-30 minutes, making it impractical for use in most sick patients. Thus, higher angular resolution diffusion acquisition strategies [8, 9], measures of non-Gaussian diffusion [10], advanced biophysical modeling [11, 12, 13] and high spatial resolution diffusion studies of cortical and hippocampal layers [14, 15] have shown exciting potential utility for studying nervous tissue in disease that is thus far unrealized in daily clinical practice.

Recently, simultaneous multi-slice (SMS) acquisition with a blipped- CAIPIRINHA readout has demonstrated the potential to reduce scan times for 2D multislice diffusion EPI [16, 17]. This technique relies on exciting multiple slices simultaneously and reconstructing them individually using the slice GRAPPA method. Since multiple slices are excited simultaneously, the overall repetition time (TR) for a desired spatial coverage can be reduced. The SMS acceleration method is SNR preserving with no intrinsic reduction in signal due to reduced sampling. The only SNR penalty is due to g-factor related losses during slice GRAPPA reconstruction. In simple terms for practicing radiologists like myself, this new SMS technology allows us to acquire the same diffusion data for a variety of clinical and translational research applications using a much shorter TR and shortened overall scan time. Alternatively SMS can be used to increase slice resolution and/or increase the overall volume of coverage in the same scan time.

At our institution, we were quick to recognize the potential practical workflow advantages for SMS diffusion to reduce scan time requirements in our patient population. In our initial explorations of the SMS diffusion application in healthy volunteers, we learned that one must pay particular attention to correct fat saturation. With single-shot EPI, an unsaturdated fat signal affects only a single slice. With SMS, there is potential for aliasing into all simultaneously acquired slices. With TR reduction below 2.5 seconds, factors such as increased acoustic noise may make patients less comfortable. We also noted that SMS trace images have more T1-weighting than we were used to seeing – this 'T1-shine through' is most evident in the limbic cortical regions and in the central portions of the cortical spinal tract as it descends through the hemispheric white matter away from the hand knob region. We directly compared the axial diffusion sequence for our routine MRI head protocol to an SMS version with acceleration factor of 2 and a TR reduced by 50%. Scans were performed on a MAGNETOM Skyra 3T (Siemens Healthcare, Erlangen, Germany) with a Head/Neck 20 coil. With the calibration scan required for the SMS reconstructions, scan time was reduced approximately 40%, thereby saving 1 minute per scan. Given that a diffusion-weighted sequence is present in almost all neuroradiology protocols, this 1 minute time savings would translate into sufficient time for an additional 2-3 patient scans per day per magnet at a busy outpatient practice. Similar results are expected for coronal diffusion acquisitions although this is not a part of our institution's routine protocols. Further time savings might be realized with 3 or 4-fold slice acceleration using array coils with more receive elements (such as a Siemens 64-channel head and neck coil). In a blinded side-by-side comparison, 3 neuroradiologists universally agreed that image quality was equivalent between the routine and SMS-accelerated axial diffusion trace sequence and calculated ADC images such that the latter was acceptable for routine clinical work (see examples in Fig. 1).

Next we compared diffusion tensor imaging and deterministic tractography for presurgical planning cases – again, side-by-side comparison of data obtained with SMS acceleration factor of 2 appeared equivalent and appropriate for use in clinical care. Tractography results for the corticospinal tract and arcuate fasciculus in close proximity to various ipsilateral intra-axial neoplasms were equivalent for routine and SMS-based high angular resolution diffusion acquisitions (see example in Fig. 2). Our referring neurosurgeons have been very happy with the resulting data and have used SMS-derived tracto-graphy as part of their routine workflow on a weekly basis for surgical planning over the past 9 months. Thus far, we have scanned over 1000 patients with MRI head protocols using SMS diffusion without problems or patient recalls for diffusion image quality. The initial results of these comparisons were reported at RSNA last year [18] and a more detailed report has been submitted for publication. Completing routine clinical scans faster has many practical advantages for patients and radiology administrators, but what I personally am most excited

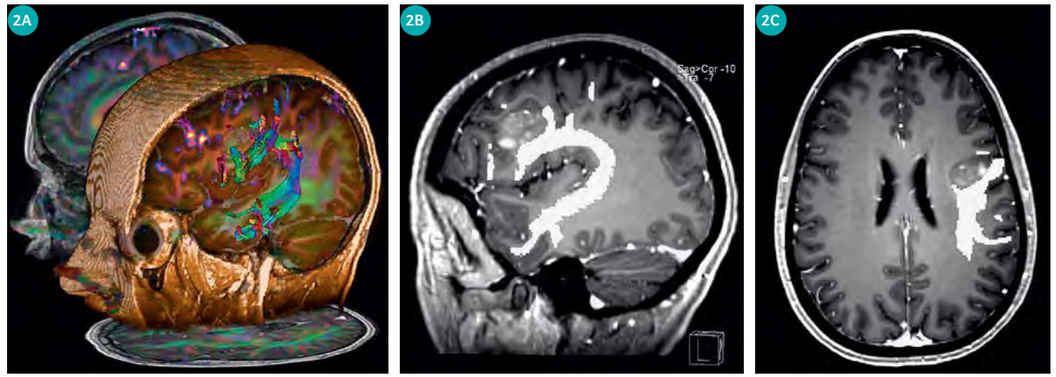

2 Deterministic diffusion tensor tractography of the arcuate fasciculus based on a simultaneous multi-slice diffusion dataset from a left-language dominant patient with a left frontal operculum high-grade glioma (**2A**: 3D lateral projection of tracts on MPRAGE with overlay from fMRI word generation task). Oblique sagittal and axial 2D reformats (**2B, C** respectively) demonstrate that the tumor margin abuts the inferior and medial margins of the tractography-visualized frontal projections of the arcuate fasciculus. Over the past year we have consistently obtained excellent tractography results for presurgical planning patients using SMS diffusion acquisition strategies – the accelerated acquisition quickly provides a diffusion dataset with high angular resolution, reduces patient motion problems and leaves more available scan time for detailed functional MRI assessment of eloquent cortex.

3 Short scan times enabled by simultaneous multi-slice diffusion should facilitate more frequent clinical use or implementation of advanced diffusion acquisitions and postprocessing. Here an example of caudal midbrain anatomy depicted with conventional axial T2 **(3A)**, track density images **(3B)** and direction-encoded track density **(3C)**. This advanced diffusion technique requires high angular resolution diffusion acquisitions (64 directions, b = 2500 s/mm^2), but can be acquired with SMS approaches in under 10 minutes. Exquisite anatomical detail is obtained and may be exploited in the future for new biomarkers of brainstem pathology and functional neurosurgery planning [for details see 19-21].

about is the potential for SMS-accelerated diffusion to enable more translational research in patient populations with advanced diffusion acquisition and postprocessing strategies. Frankly, most patients, particularly elderly sick patients, will not tolerate individual scan sequence scan times beyond 8-10 minutes well. SMS acquisition strategies finally may allow us to apply advanced diffusion strategies reported at research meetings to real patients. As an example, over the past 6 months, we have been using SMS-diffusion acquisition strategies to acquire high angular resolution multiple b-shell scans for diffusion kurtosis imaging and advanced models of mesoscopic tissue structure in over 500 patients as part of an NIH-funded study—it would not be practical to include this acquisition using conventional diffusion acquisitions because of scan time and workflow limitations on our busy clinical scanners. We also use SMS to obtain diffusion data sufficient for super-resolution tract density imaging (TDI) [19] to define thalamic substructures for functional neurosurgery planning in patients with essential tremor and Parkinson's disease [20]. Recent results indicate SMS diffusion acquisitions combined with TDI can reveal internal brainstem anatomy not previously seen in living patients

using 3T MRI [21] (see examples in Fig. 3). These latter two results from our group suggest neuroradiologists may need to relearn detailed anatomy for deep gray nuclei and brainstem structures that were previously considered difficult or impossible to visualize outside autopsy. Such studies also could lead to direct targeting opportunities in the future for functional neurosurgery applications.

Finally, it should be emphasized that the best models of human pathology are living human patients! The present difficulty studying real patients with long diffusion scan times has so far limited application of advanced biophysical models of tissue mesoscopic structure derived from diffusion data to cooperative, motivated outpatients with chronic conditions, animal models of human disease, and ex vivo, formaldehyde-fixed samples, where many water diffusion and relaxation properties are altered [20, 23]. I personally anticipate that SMS diffusion techniques will provide a substantial new window of opportunity to study many new patient populations with both acute and chronic pathologies directly—this should result in improved understanding of human neurologic diseases, such as the nervous tissue changes associated with acute stroke. SMS appears to represent a transformative technology for translating advanced diffusion MRI applications into clinical practice.

References

[1] Schaefer PW, Grant PE, Gonzalez RG. Diffusion-weighted MR imaging of the brain. Radiology 2000; 217(2): 331-345.

[2] Andre JB, Zaharchuk G, Saritas E, et al. Clinical evaluation of reduced field-of-view diffusion-weighted imaging of the cervical and thoracic spine and spinal cord. Am J Neuroradiol 2012; 33(10): 1860-1866.

[3] Thoeny HC. Diffusion-weighted MRI in head and neck radiology: applications in oncology. Cancer Imaging 2011; 10: 209-214.

[4] Barajas RF Jr, Rubenstein JL, Chang JS, Hwang J, Cha S. Diffusion-weighted MR imaging derived apparent diffusion coefficient is predictive of clinical outcome in primary central nervous system lymphoma. Am J Neuroradiol 2010; 31(1): 60-66.

[5] Mesaros S, Rocca MA, Kacar K, et al. Diffusion tensor MRI tractography and cognitive impairment in multiple sclerosis. Neurology 2012; 78(13): 969-975.

[6] Wu JS, Zhou LF, Tang WJ, et al. Clinical evaluation and follow-up outcome of diffusion tensor imaging-based functional neuronavigation: a prospective, controlled study in patients with gliomas involving pyramidal tracts. Neurosurgery 2007; 61(5): 935-948.

[7] Mukherjee P, Chung SW, Berman JI, Hess CP, Henry RG. Diffusion tensor MR imaging and fiber tractography: technical considerations. Am J Neuroradiol 2008; 29(5): 843-852.

[8] Tuch, DS. Q-ball imaging. Magn Reson Med 2004; 52(6): 1358-1372.

[9] Wedeen VJ, Hagmann P, Tseng WY, Reese TG, Weisskoff RM. Mapping complex tissue architecture with diffusion spectrum magnetic resonance imaging. Magn Reson Med 2005; 54(6): 1377-1386.

[10] Jensen JH, Helpern JA. MRI quantification of non-Gaussian water diffusion by kurtosis analysis. NMR Biomed 2010; 23(7): 698-710.

[11] Assaf Y, Freidlin RZ, Rohde GK, Basser PJ. New modeling and experimental framework to characterize hindered and restricted water diffusion in brain white matter. Mag Reson Med 2004; 52(5): 965-978.

[12] Zhang H, Schneider T, Wheeler-Kingshott CA, Alexander DC. NODDI: Practical in vivo neurite orientation dispersion and density imaging of the human brain. Neuroimage 2012; 61(4): 1000-1016.

[13] Fieremans EJ, Jensen JH, Tabesh A, Hu C, Helpern J.A. White matter model for diffusional kurtosis imaging. Paper presented at: ISMRM 2010. Proceedings of the 18th Annual Meeting of the International Society for Magnetic Resonance in Medicine: 2010 May 1-7; Stockholm, Sweden.

[14] McNab JA, Polimeni JR, Wang R, et al. Surface based analysis of diffusion orientation for identifying architectonic domains in the in vivo human cortex. Neuroimage 2013; 69: 87-100.

[15] Shepherd T, Ozarslan E, Yachnis AT, King MA, Blackband SJ. Diffusion tensor microscopy indicates the cytoarchitectural basis for diffusion anisotropy in the human hippocampus. Am J Neuroradiol; 28(5): 958-964.

[16] Setsompop K, Gagoski BA, Polimeni JR, Witzel T, Wedeen VJ, Wald LL. Blipped-controlled aliasing in parallel imaging for simultaneous multislice echo planar imaging with reduced g-factor penalty. Magn Reson Med 2012; 67(5): 1210-1024.

[17] Xu J, Moeller S, Auerbach EJ, et al. Evaluation of slice accelerations using multiband echo planar imaging at 3T. Neuroimage 2013; 83: 991-1001.

[18] Young MG, Cohen BA, Glielmi C, et al. Multiband sequence reduces scan time for diffusion MRI and tractography in clinical patients. Paper presented at: RSNA 2014. Proceedings of the 100th Scientific Assembly and Annual Meeting of the Radiological Society of North America; 2014 Nov 30 – Dec 5; Chicago, USA.

[19] Calamante F, Tournier JD, Jackson GD, Connelly A. Tract density imaging (TDI) : super-resolution white matter imaging using whole-brain track density mapping. Neuroimage 2010; 53(4): 1233-1243.

[20] Shepherd TM, Chung S, Glielmi C, Mogilner AY, Boada F, Kondziolka D. 3-Tesla magnetic resonance imaging track density imaging to identify thalamic nuclei for functional neurosurgery. Paper presented at: CNS 2014. Proceedings of the 63rd Annual Congress of Neurological Surgeons; 2014 Oct 18-22; Boston, USA.

[21] Hoch M, Chung S, Yoshimoto A, Ben-Eliezer N, Fatterpekar G, Shepherd TM. Advanced multiparametric MRI reveals detailed in vivo brainstem anatomy at 3-T. Paper presented at: ASNR 2015. Proceedings of the 53rd Annual Meeting of the American Society of Neuroradiology; 2015 Apr 25-30; Chicago, USA.

[22] Shepherd TM, Flint JJ, Thelwall PE., et al. Postmortem interval alters the water relaxation and diffusion properties of rat nervous tissue – implications for MRI studies of human autopsy samples. Neuroimage 2009; 44(3): 820-826.

[23] Shepherd TM, Thelwall PE, Stanisz GJ, Blackband SJ. Aldehyde fixative solutions alter the water relaxation and diffusion properties of nervous tissue. Magn Reson Med 2009; 62(1): 26-34.

Contact
Timothy Shepherd
Timothy.Shepherd@nyumc.org

Advancing Diffusion MRI Using Simultaneous Multi-Slice Echo Planar Imaging

Kawin Setsompop[1,2]; Stephen F. Cauley[1,2]; Lawrence L. Wald[1,2]
[1]Martinos Center for Biomedical Imaging, Department of Radiology, Massachusetts General Hospital, Charlestown, MA, USA
[2]Department of Radiology, Harvard Medical School, Boston, MA, USA

Introduction

There has been a recent significant interest in the use of parallel imaging based Simultaneous Multi-Slice (SMS) acquisition [1] to increase the temporal efficiency of many imaging sequences in MRI. In particular, the use of SMS for diffusion MRI (dMRI) and functional MRI (fMRI) has fundamentally changed the scope of studies that clinicians and researchers are able to perform with these imaging sequences. For dMRI, SMS has opened up the possibility of obtaining information from many more diffusion encoding directions in a limited timeframe, to enable more complex/advanced diffusion acquistions to be performed in clinical and neuroscientific settings.

Due to the use of diffusion encoding gradients in dMRI, large temporally and spatially varying phase contamination exists, which hampers the utility of multi-shot acquisitions. As such, dMRI acquisitions are often based on rapid single-shot 2D spin- echo EPI sequence. This sequence provides high quality imaging but at a cost of being highly inefficient. Figure 1 shows the sequence diagram for such acquisition, where a single 2D imaging slice is excited, after which diffusion encoding is performed and the data for that particular slice is then readout/received using EPI encoding. This process is repeated multiple times, once for each imaging slice, until whole-brain coverage is achieved. As depicted, the diffusion encoding period can represent a significant portion of the acquisition time. This diffusion encoding is performed using magnetic field gradient pulses which provide encoding to the whole imaging volume. However, for each acquisition period, only a single slice is excited and acquired, and the lengthy diffusion encoding has to be repeated for all imaging slices, leading to large inefficiency.

Standard 2D slice-by-slice dMRI

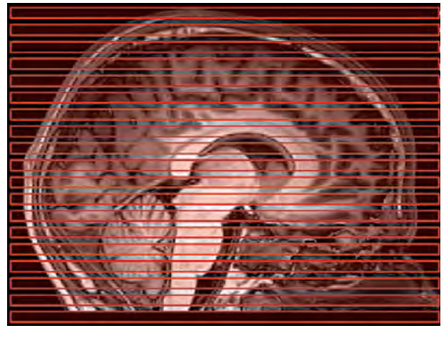

Contrast encoding is 3D but receive is 2D
→ highly inefficient!

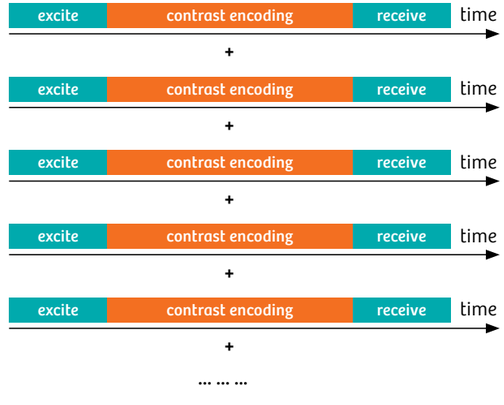

1 The inefficiency of standard 2D DWI techniques is illustrated. Although the lengthy diffusion contrast-encoding encompasses the entire volume, only a single slice is acquired. Simultaneous multi-slice enables the concurrent acquisition of several imaging slices during a single diffusion encoding. Unlike typical in-plane acceleration techniques, which only shorten the receive portion of the acquisition, SMS allows for proportional reductions in total scan time as the multiband factor is increased.

Blipped-CAIPIRINHA SMS-EPI

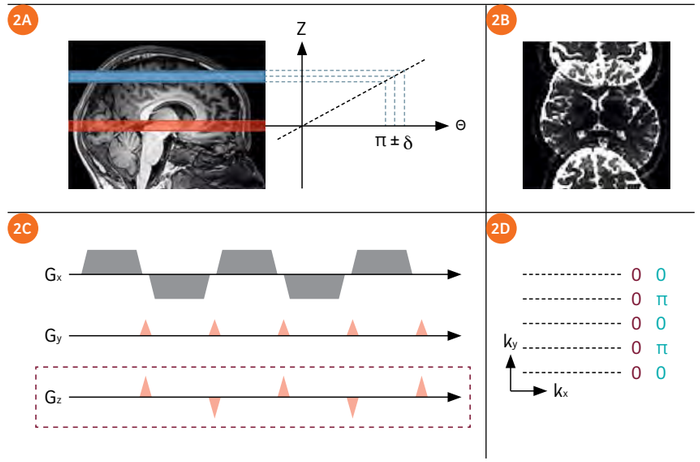

2 A blipped-CAIPIRINHA SMS-EPI gradient scheme applied across the X, Y and Z (Readout, Phase-Encode, and Slice) axes is illustrated. The G_z gradient blips required to create a FOV/2 shift between two simultaneously acquired slices are shown (collapsed image in **2B**). The blipped-CAIPIRINHA method varies the sign of the G_z gradient blips in order to avoid accumulation of through-slice phase variation, which would result in voxel titling artifacts. The accumulated phase applied to each of the k_y lines are shown for the two slices **(2D)**.

The use of conventional 2D parallel imaging acceleration [2-4] in dMRI can reduce the number of phase encoding steps of EPI which reduces image distortion and blurring artifacts. However, such technique does not provide significant acceleration to dMRI, since they only shorten the EPI encoding period and not the other components of the data acquisition, in particular the lengthy diffusion encoding. The use of simultaneous multi-slice (SMS) acceleration [1], on the other hand, allows for the concurrent acquisition of several imaging slices (the slices will appear collapsed before reconstruction) during each acquisition period, thereby reducing the number of acquisition periods needed to perform volumetric acquisition. Thus, SMS is much more effective at providing scan time reduction in dMRI, where the total scan time is now reduced by a factor equal to the number of simultaneously excited slices (multiband (MB) factor). Additionally, unlike conventional parallel imaging, SMS does not shorten the EPI encoding period and is not affected by the undesirable √R SNR penalty of conventional parallel imaging.

Several SMS methods have been applied to single shot SMS-EPI, including Wideband imaging [5, 6], Simultaneous Image Refocusing (SIR) [7, 8] and parallel image reconstruction based multi-slice imaging [9, 10]. However, the presence of significant artifact and/or signal-to-noise (SNR) loss from these methods have prevented their wide scale adoption in dMRI. In particular, parallel imaging based multi-slice imaging suffers from high g-factor noise amplification in brain MRI. This is due to the fact that the imaging field-of-view (FOV) along the slice direction is typically small for brain acquisitions, causing the aliased voxels of the simultaneously acquired slices to be spatially close which makes it hard to tease them apart. An improved parallel imaging strategy termed CAIPIRINHA [11], which creates an inter-slice image shift between simultaneously acquired slices to increase the distance between the aliased voxels has been proposed as a way to reduce the g-factor penalty associated with SMS. The CAIPIRINHA method creates an inter-slice shift by utilizing a different RF pulse for the data acquisition of each k-space line, where each RF pulse is designed to induce a different phase modulation to each of the slices that are being acquired simultaneously. This is feasible for multi-shot acquisitions but not for single-shot EPI where only a single RF pulse is used to acquire all lines of k-space. An initial attempt to adopt CAIPIRINHA for single-shot EPI acquisitions was performed by Nunes et al. [9]. Here, a Wideband-like approach was used in the phase encoding and readout directions to increase the distance between aliased voxels. However, this resulted in voxel tilting (blurring) artifacts and heavily restricted the distance that could be imposed between aliased voxels. In this article, we describe the blipped-CAIPIRINHA method [12] which is a modification of Nunes' approach, to generate the desired voxel shifts in the phase encoding direction without tilting artifacts. This approach has provided us with the ability to perform high quality parallel imaging based SMS-EPI acquisition that can be used to significantly shorten dMRI acquisition time.

Blipped-CAIPIRINHA

The blipped-CAIPIRINHA method utilizes additional Gz magnetic field gradient blips during the EPI readout. Figure 2 shows the standard Gx and Gy gradients of the EPI encoding, along with these additional Gz gradient blips. These Gz blips are applied concurrently with the Gy phase encoding blips to create a different phase modulation between the simultaneously excited slices for the data acquisition of each k-space line. For this example, the Gz blips are being applied to create a FOV/2 shift along the phase encoding (PE) direction between two simultaneously acquired slices (collapsed image shown in top-right of Figure 2). In order to create the desired inter-slice shift, an appropriate gradient blip area must be used for these Gz blips. Specifically, in the example in Figure 2, each Gz blip will have to create a π phase increment to the spins located at the upper slice (blue) and no increment to the lower slice (red). The phase modulations along ky caused by the Gz blip train are shown on the lower-right of Figure 2, for the upper (blue) and lower (red) imaging slices. With no phase modulation to the lower slice, this slice remains unaffected. On the other hand, the linear phase moduation along ky at π phase increment for the top slice causes this slice to shift by FOV/2 along the PE direction. As such, a desired FOV/2 inter-slice shift is achieved.

It is important to note that each Gz blip will also introduce a small phase variation 2δ across the finitely thick slices being acquired as shown in Figure 2. This through-slice phase variation created by each blip will result in a very minor signal attenu-ation (typically less than 1%). The important concept in blipped-CAIPIRINHA is the utilization of alternating positive and negative gradient blips to limit ability of the gradient moment and this through-slice phase variation to accumulate during the EPI encode and cause significant signal attenuation.

SMS-3 Blipped-CAIPIRINHA with 32-channel head coil

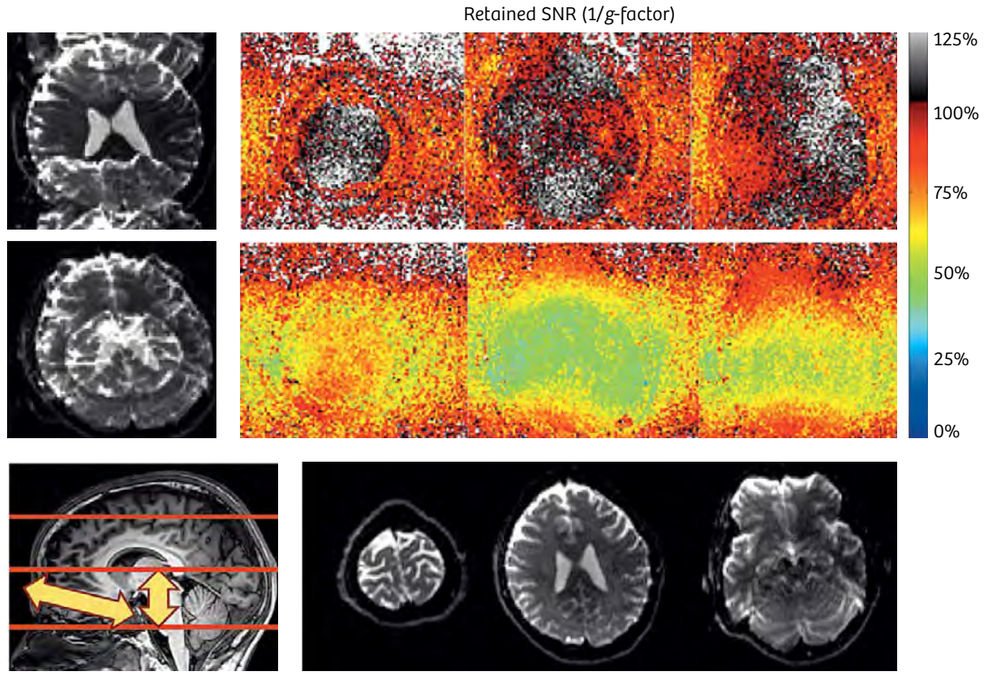

3 SMS-EPI at SMS-3 acceleration acquired at 3T using Siemens' 32-channel coil. The *g*-factor associated with FOV/2 shift and no-shift parallel imaging reconstructions are compared. The retained SNR (1 / *g*-factor), when no-shift was applied dropped significantly to 68%. The blipped-CAIPIRINHA method with FOV/2 shift retained over 99% of the SNR, while avoiding the 3.5 voxel tilt associated with standard wideband approaches.

Multiband RF pulse: SLR & VERSE algorithm
high quality slice profile and low SAR

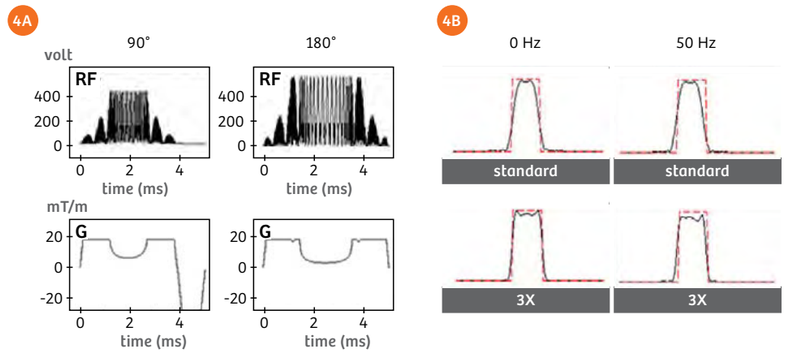

Slice-GRAPPA recon: leak-block and dual kernel

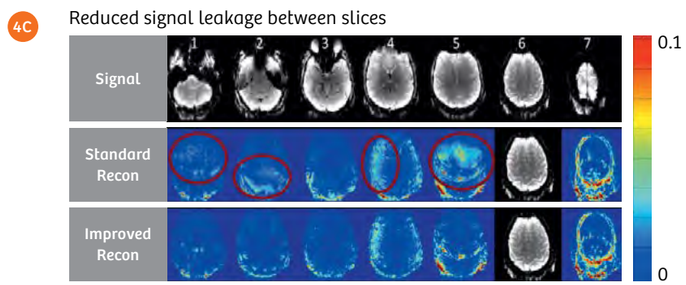

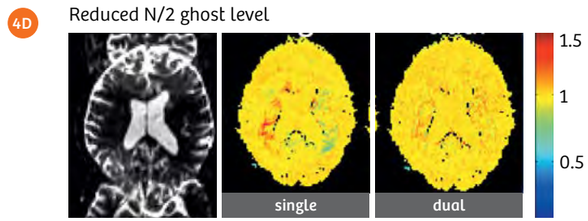

4 Critical implementation aspects for the blipped-CAIPIRINHA method are highlighted. The multiband 90-180 pulses with slice acceleration factor-3 designed using both the SLR and VERSE algorithms are shown. **(4A)** The VERSE 90 and 180 RF pulses along with corresponding Gradient pulses. **(4B)** A comparison of slice-profiles from a standard single-slice 90-180 RF pulse pair and those obtained from the slice acceleration factor 3 RF pulse pair. These pulses are necessary to ensure image quality while limiting peak-power and SAR. The benefits of the 'LeakBlock' Slice-GRAPPA reconstruction technique in reducing leakage signal contamination between simultaneously acquired slices is shown **(4C)**.The individual leakage signal contaminations onto the 6th imaging slice (for a SMS 7 acquisition) are greatly reduced when compared with standard slice-GRAPPA reconstruction. The use of 'dual kernel' slice-GRAPPA to separate SMS 3 blipped-CAIPIRINHA EPI with FOV/2 shift data is shown **(4D)**. The dual kernels operate specifically to the even and the odd lines of the slice-collapsed *k*-space data, and enable clean separation of both of the slice data and associated ghost (prior to the application of typical ghost correction).

This solves the issue of the Wideband approach where only positive Gz blips are employed which results in accumulation of through-slice dephasing and voxel tilting artifacts. Thus, the blipped-CAIPIRINHA method facilitates efficient CAIPIRINHA controlled aliasing schemes for simultaneously acquired slices in EPI. This can be seen clearly when examining the 3× slice-accelerated (SMS 3) example acquired using a 32-channel head coil at 3T shown in Figure 3. Here, the g-factor associated with FOV/2 shift and no-shift parallel imaging reconstructions are compared (both with slice-GRAPPA reconstruction). When no-shift was applied between the simultaneously acquired slices, the average retained SNR (1 / g-factor) dropped significantly to 68%. The blipped-CAIPIRINHA method with FOV/2 shift retained over 99% of the SNR, while removing the 3.5 voxel tilt that would have been present with the standard wideband approach. Thereby, blipped-CAIPIRINHA enables three times faster acquisitions in dMRI without incurring significant SNR penalty. (Note that in some regions the retained SNR is slightly greater than unity indicating some noise cancellation in the reconstruction process as previously demonstrated in low acceleration in-plane GRAPPA acquisitions [13]).

RF pulse design and image reconstruction

When considering the use of blipped-CAIPIRINHA for high slice acceleration factors, there are several sequence design and image reconstruction aspects that need to be carefully developed. Of particular importance to diffusion-weighted imaging (DWI) is the design of the multiband RF pulse that allows for multiple slices to be simultaneously excited in SMS acquisitions. Multiband RF pulses cause an increase in SAR, which is especially problematic for DWI since it relies on high SAR spin-echo 90-180 pulses. At SMS-3 acceleration, the use of the VERSE algorithm [14] has been shown to provide adequate SAR reduction for in vivo DWI at 3T [15]. However, the benefit of SAR reduction from VERSE comes at a cost of slice profile distortion at off-resonance frequencies. This can be mitigated by the use of the SLR algorithm for RF pulse design along with a high time-bandwidth product that improves the slice-profile quality prior to the application of VERSE. Figure 4 (A, B) shows multiband 90-180 pulses with slice acceleration factor 3 designed using both the SLR and VERSE algorithms. Figure 4A shows the VERSE 90 and 180 RF pulses along with corresponding gradient pulses. Figure 4B shows the comparison of slice-profiles obtained from a standard single-slice 90-180 RF pulse pair and those obtained from the slice acceleration factor 3 RF pulse pair. Here, the high-quality slice profiles are achieved at both on resonance and 50 Hz off-resonance.

In addition to the combined design of VERSE and SLR, a number of other approaches have been developed to reduce both SAR and peak-power of MB pulses. These techniques are particularly beneficial at higher slice accelerations and/or for ultra-high field imaging. In order to reduce peak-power, a phase optimization scheme [16], a pulse time-shift method [17] and a combined approach [18, 19] of phase optimization with the use of 90° and 180° pulses with spatially-varying phases that combine to provide a flat spin-echo excitation phase have been proposed. In addition, the Power Independent of Number of Slices (PINS) [20] and MultiPINS [21] RF pulse designs have been proposed as a strategy to excite/refocus a large number of imaging slices simultaneously without increasing peak power or SAR.

A number of techniques have been developed in order to improve the quality of SMS-EPI image reconstruction. The original SENSE/GRAPPA approach for SMS reconstruction [22] has been modified to facilitate CAIPIRINHA acquisitions with inter-slice FOV shifts [23-25]. Slice-GRAPPA [12], which has been widely-used for blipped-CAIPIRINHA SMS-EPI reconstruction, has been redesigned to provide robust reconstruction through a 'LeakBlock' technique [26]. This technique reduces the leakage signal contamination between simultaneously acquired slices and has been shown to improve temporal stability at high accelerations. Figure 4C shows a comparison of signal leakage contamination in the standard and the improved LeakBlock slice-GRAPPA reconstructions for blipped-CAIPIRINHA acquisition at SMS-7 using a 32-channel head coil. It can be clearly seen that the individual leakage signal contaminations onto the 6th imaging slice are greatly reduced using the LeakBlock reconstruction.

Another important consideration for SMS-EPI reconstruction is in the minimization of N/2 image ghosting artifacts. For SMS-EPI, this is a particular concern since a different slice-specific ghost correction could be required for each of the simultaneously acquired imaging slices (due to differences in phase error of the N/2 ghost for different slice locations). Thus, the N/2 ghost cannot be cleanly removed from the slice-collapsed dataset prior to the parallel imaging (slice-unaliasing) reconstruction. The use of a 'dual kernel' slice-GRAPPA, where separate GRAPPA kernels are applied to the even and the odd lines of the slice-collapsed *k*-space data has been shown to overcome this issue [15]. This method enables a clean separation of both of the slice data and associated ghost, prior to the application of typical ghost correction.

3x Faster brain dMRI

Q-ball: 12 min ➔ 4 min

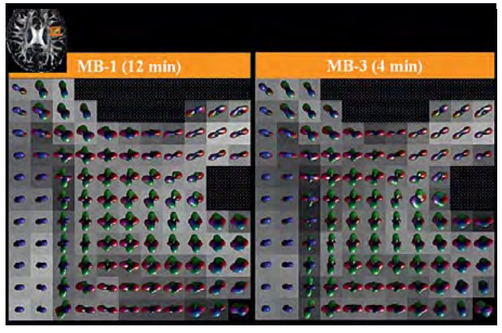

DTI: 10 min ➔ 3 min

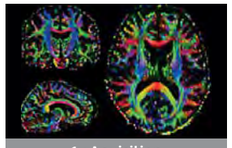
1x Aquisition

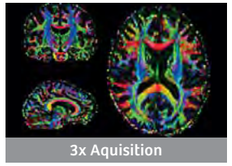
3x Aquisition

DSI: 45 min ➔ 15 min

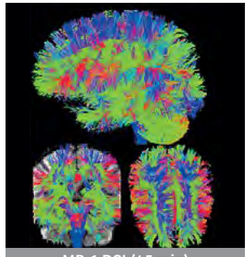
MB-1 DSI (45 min)

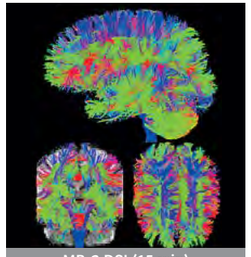
MB-3 DSI (15 min)

5 Diffusion Tensor Imaging, Q-ball, and Diffusion Spectrum Imaging are compared using standard SMS 1 and blipped-CAIPIRINHA SMS 3 acquisitions at 3T using Siemens' 32-channel head coil. The high level of similarities in color FA, Orientation Distribution Function, and the fiber tracking results can be clearly seen.

Applications outside of the brain

Liver diffusion

b = 50

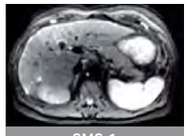
SMS-1

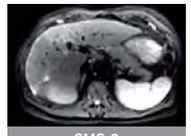
SMS-2

b = 400

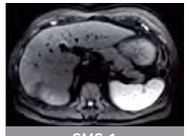
SMS-1


SMS-2

b = 800


SMS-1


SMS-2

ADC


SMS-1


SMS-2

Whole-body diffusion

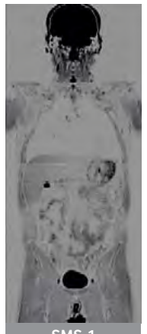
SMS-1


SMS-2

Breast diffusion


SMS-1


SMS-2

6 Emerging applications of DWI in the body are demonstrated. Blipped-CAIPIRINHA with SMS 2 and in-plane GRAPPA 2 was used in large FOV body diffusion. Relative to conventional DWI with in-plane GRAPPA 2, similar image quality can be seen. Blipped-CAIPIRINHA SMS enables effective combination of in-plane GRAPPA acceleration which is critical for the reduction of distortions especially in large FOV DWI of the body. With blipped-CAIPIRINHA SMS-EPI, scan time reductions to a factor of 2 with similar image quality can be obtained for the liver, breast, and whole-body DWI.

Figure 4D shows a comparison of the N/2 ghost artifact level for an SMS-3 blipped-CAIPIRINHA SMS-EPI with FOV/2 shift reconstructed using i) single kernel slice-GRAPPA and ii) dual kernel slice-GRAPPA approaches. Note that the ghost artifact of the top imaging slice in the SMS acquisition lands directly in the center of the imaging FOV of the middle imaging slice (due to the FOV/2 inter-slice shift). This prevents the single kernel slice-GRAPPA approach from accurately unaliasing the ghosting artifact. Figure 4 shows the corresponding large reconstruction artifact in the center of the middle imaging slice. With the use of dual kernel slice-GRAPPA, this artifact has been mitigated. The dual kernel approach has been successfully applied to SENSE/GRAPPA reconstruction [27] and an extension of the method has been used to overcome artifacts associated with phase-encode line bunching [28]. Finally, for SENSE based reconstruction of SMS data, a slice-specific phase error of the ghost artifact has been successfully incorporated into the parallel imaging reconstruction [29].

Diffusion-weighted imaging applications

With the careful design of RF pulses and the image reconstruction framework, blipped-CAIPIRINHA allows for the efficient acquisition of high quality SMS-EPI data for DWI. In clinical settings, where time is limited, DWI is often restricted to only a small number of diffusion encoding directions. This constrains studies to only examine the most basic diffusion information, such as the apparent diffusion coefficient (ADC). With the use of blipped-CAIPIRINHA SMS-EPI, diffusion-weighted acquisitions can be accelerated robustly by 3-fold to provide high quality data with negligible SNR loss and artifact levels. This has allowed for more diffusion directions to be obtained in a clinically relevant time-frame, enabling more complex diffusion models/metrics (e.g. Fractional Anisotropy (FA), Diffusion Kurtosis, and fiber tracking) to be considered. Figure 5 demonstrates the use of blipped-CAIPIRINHA to achieve 3-fold acceleration for typical neuroimaging acquisitions based upon Diffusion Tensor Imaging (DTI), Q-ball, and Diffusion Spectrum Imaging (DSI). Here, the color FA, Orientation Distribution Function (ODF), and the fiber tracking results from these diffusion models are compared using standard SMS-1 and blipped-CAIPIRINHA SMS-3 acquisitions. In all cases, the high quality of the results is maintained at a 3-fold speed up with the blipped-CAIPIRINHA technique.

There is a growing interest in the application of DWI to areas outside the brain, where it has also proven to be highly sensitive to tissue abnormalities. Similar to the neuroimaging applications described above, blipped-CAIPIRINHA SMS-EPI can play a role in speeding up acquisitions in the body. Here, a large in-plane FOV has to be encoded and in-plane acceleration (typically a factor of 2) is used to reduce image distortion. While accelerations in the slice and in-plane directions are compatible, the use of both can lead to a high total acceleration factor (the product of the two acceleration factors) and result in higher g-factor noise amplifications. For the DWI applications where SNR is inherently low, it is desirable to keep the noise penalty to a minimum. Thus, a combined SMS-2 and in-plane-2 acceleration strategy is typically employed for blipped-CAIPIRINHA SMS-EPI in the body.

Figure 6 shows DWI results for liver, whole-body, and breast imaging from a standard in-plane-2 acceleration with and without the inclusion of blipped-CAIPIRINHA SMS factor 2. The imaging results are near identical, with the blipped-CAIPIRINHA acquisition providing a 2-fold speed up in imaging time. This is particularly useful for whole-body DWI, where a large number of imaging slices are acquired. Reducing these lengthy scans (often ~20 minutes is required for standard diffusion scans focusing on the basic ADC metric) will have a significant impact on the wide-spread adoption of whole-body DWI in clinical settings.

References

[1] Larkman DJ, Hajnal J V, Herlihy AH, Coutts GA, Young IR, Ehnholm G. Use of multicoil arrays for separation of signal from multiple slices simultaneously excited. J Magn Reson imaging. 2001;13:313–7.

[2] Pruessmann KP, Weiger M, Scheidegger MB, Boesiger P. SENSE: sensitivity encoding for fast MRI. Magn Reson Med [Internet]. 1999 Nov;42(5):952–62. Available from: 10.1002/(SICI)1522-2594(199911)42:5<952::AID-MRM16>3.0.CO;2-S.

[3] Griswold MA, Jakob PM, Heidemann RM, Nittka M, Jellus V, Wang J, et al. Generalized autocalibrating partially parallel acquisitions (GRAPPA). Magn Reson Med [Internet]. 2002 Jun [cited 2014 Jan 21];47(6):1202–10. Available from: http://www.ncbi.nlm.nih.gov/pubmed/12111967.

[4] Sodickson DK, Manning WJ. Simultaneous acquisition of spatial harmonics (SMASH): fast imaging with radiofrequency coil arrays. Magn Reson Med [Internet]. 1997 Oct;38(4):591–603. Available from: http://www.ncbi.nlm.nih.gov/pubmed/9324327.

[5] Paley MNJ, Lee KJ, Wild JM, Griffiths PD, Whitby EH. Simultaneous parallel inclined readout image technique. Magn Reson Imaging [Internet]. 2006 Jun [cited 2014 Sep 9];24(5):557–62. Available from: http://www.ncbi.nlm.nih.gov/pubmed/16735176.

[6] Weaver JB. Simultaneous Multislice Acquisition of MR Images. 1988;284:275–84.

[7] Feinberg D a., Reese TG, Wedeen VJ. Simultaneous echo refocusing in EPI. Magn Reson Med. 2002;48(1):1–5.

[8] Reese TG, Benner T, Wang R, Feinberg D a., Van Wedeen J. Halving imaging time of whole brain diffusion spectrum imaging and diffusion tractography using simultaneous image refocusing in EPI. J Magn Reson Imaging. 2009;29(3):517–22.

[9]Nunes RG, Hajnal J V, Golay X, Larkman DJ. Simultaneous slice excitation and reconstruction for single shot EPI . Proc Intl Soc Mag Reson Med. 2006. p. 293.

[10]Moeller S, Yacoub E, Olman C a, Auerbach EJ, Strupp J, Harel N, et al. Multiband multislice GE-EPI at 7 tesla, with 16-fold acceleration using partial parallel imaging with application to high spatial and temporal whole-brain fMRI. Magn Reson Med [Internet]. 2010 May [cited 2014 Jan 21];63(5):1144–53. Available from: http://www.pubmedcentral.nih.gov/articlerender.fcgi?artid=2906244&tool=pmcentrez&rendertype=abstract.

[11]Breuer FA, Blaimer M, Heidemann RM, Mueller MF, Griswold MA, Jakob PM. Controlled aliasing in parallel imaging results in higher acceleration (CAIPIRINHA) for multi-slice imaging. Magn Reson Med. 2005;53:684–91.

[12]Setsompop K, Gagoski BA, Polimeni JR, Witzel T, Wedeen VJ, Wald LL. Blipped-controlled aliasing in parallel imaging for simultaneous multislice echo planar imaging with reduced g-factor penalty. Magn Reson Med [Internet]. 2012 May [cited 2014 Jan 21];67(5):1210–24. Available from: http://www.pubmedcentral.nih.gov/articlerender.fcgi?artid=3323676&tool=pmcentrez&rendertype=abstract.

[13]Polimeni JR, Wiggins GC, Wald LL. Characterization of artifacts and noise enhancement introduced by GRAPPA reconstructions. Proc Intl Soc Mag Reson Med. 2008. p. 1286.

[14]Conolly SM, Nishimura DG, Macovski A, Glover GH. Variable-rate selective excitation. J Magn Reson [Internet]. 1988 Jul [cited 2012 Jul 4];78(3):440–58. Available from: http://linkinghub.elsevier.com/retrieve/pii/002223648890131X.

[15]Setsompop K, Cohen-Adad J, Gagoski BA, Raij T, Yendiki A, Keil B, et al. Improving diffusion MRI using simultaneous multi-slice echo planar imaging. Neuroimage [Internet]. Elsevier Inc.; 2012 Oct 15 [cited 2014 Jan 30];63(1):569–80. Available from: http://www.pubmedcentral.nih.gov/articlerender.fcgi?artid=3429710&tool=pmcentrez&rendertype=abstract.

[16]Wong E. Optimized phase schedules for minimizing peak RF power in simultaneous multi-slice RF excitation pulses. Proc Intl Soc Mag Reson Med [Internet]. 2012 [cited 2014 Jan 21]. p. 2209. Available from: http://scholar.google.com/scholar?hl=en&btnG=Search&q=intitle:Optimized+phase+schedules+for+minimizing+peak+RF+power+in+simultaneous+multi-slice+RF+excitation+pulses#0.

[17]Auerbach EJ, Xu J, Yacoub E, Moeller S, Uğurbil K. Multiband accelerated spin-echo echo planar imaging with reduced peak RF power using time-shifted RF pulses. Magn Reson Med. 2013 May;69(5):1261–7.

[18]Zhu K, Kerr AB, Pauly JM. Nonlinear-Phase Multiband 90°-180° RF Pair With Reduced Peak Power. Proc Intl Soc Mag Reson Med. 2014. p. 1440.

[19]Sharma A, Bammer R, Stenger VA, Grissom W a. Low peak power multiband spokes pulses for B 1 + inhomogeneity-compensated simultaneous multislice excitation in high field MRI. Magn Reson Med [Internet]. 2015;doi: 10.1002/mrm.25455. Available from: http://doi.wiley.com/10.1002/mrm.25455.

[20]Norris DG, Koopmans PJ, Boyacioğlu R, Barth M. Power Independent of Number of Slices (PINS) radiofrequency pulses for low-power simultaneous multislice excitation. Magn Reson Med [Internet]. 2011 Nov [cited 2014 Jan 10];66(5):1234–40. Available from: http://www.ncbi.nlm.nih.gov/pubmed/22009706.

[21]Eichner C, Wald LL, Setsompop K. A low power radiofrequency pulse for simultaneous multislice excitation and refocusing. Magn Reson Med [Internet]. 2014 Oct [cited 2014 Sep 25];72:949–58. Available from: http://www.ncbi.nlm.nih.gov/pubmed/25103999.

[22]Blaimer M, Breuer F a, Seiberlich N, Mueller MF, Heidemann RM, Jellus V, et al. Accelerated volumetric MRI with a SENSE/GRAPPA combination. J Magn Reson imaging [Internet]. 2006 Aug [cited 2014 Oct 13];24(2):444–50. Available from: http://www.ncbi.nlm.nih.gov/pubmed/16786571.

[23]Stäb D, Ritter CO, Breuer F a, Weng AM, Hahn D, Köstler H. CAIPIRINHA accelerated SSFP imaging. Magn Reson Med. 2011;65:157–64.

[24]Blaimer M, Choli M, Jakob PM, Griswold M a, Breuer F a. Multiband phase-constrained parallel MRI. Magn Reson Med [Internet]. 2013 Apr [cited 2014 Jul 21];69(4):974–80. Available from: http://www.pubmedcentral.nih.gov/articlerender.fcgi?artid=3606646&tool=pmcentrez&rendertype=abstract.

[25]Moeller S, Vu AT, Auerbach E, Ugurbil K, Yacoub E. RO extended FOV SENSE/GRAPPA for multiband imaging with FOV shift. Proc Intl Soc Mag Reson Med. 2014. p. 4396.

[26]Cauley SF, Polimeni JR, Bhat H, Wald LL, Setsompop K. Interslice leakage artifact reduction technique for simultaneous multislice acquisitions. Magn Reson Med [Internet]. 2014 [cited 2014 Jan 28];72:93–102. Available from: http://www.ncbi.nlm.nih.gov/pubmed/23963964.

[27]Koopmans PJ, Poser BA, Breuer FA. 2D-SENSE-GRAPPA For Fast, Ghosting-Robust Reconstruction of In-Plane and Slice Accelerated Blipped-CAIPI-EPI. Proc Intl Soc Mag Reson Med. 2015. p. 2410.

[28]Moeller S, Auerbach EJ, Vu AT, Lenglet C, Sotiropoulos SN, Ugurbil K, et al. EPI 2D ghost correction and integration with multiband : application to diffusion imaging at 7T. Proc Intl Soc Mag Reson Med. 2015. p. 248.

[29]Zhu K, Dougherty RF, Takahashi A, Pauly J, Kerr AB. Nyquist Ghosting Correction For Simultaneous Multislice Echo Planar Imaging. 2014. p. 647.

Contact
Kawin Setsompop
kawin@nmr.mgh.harvard.edu

Simultaneous Multi-Slice (SMS) Imaging for Pre-Surgical BOLD fMRI and Diffusion Tractography: Case Illustrations

Andreas J. Bartsch[1,2,3]
[1]Radiologie Bamberg, Germany
[2]Departments of Neuroradiology, Universities of Heidelberg and Wuerzburg, Germany
[3]Oxford Centre for Functional MRI of the Brain (FMRIB), University of Oxford, UK

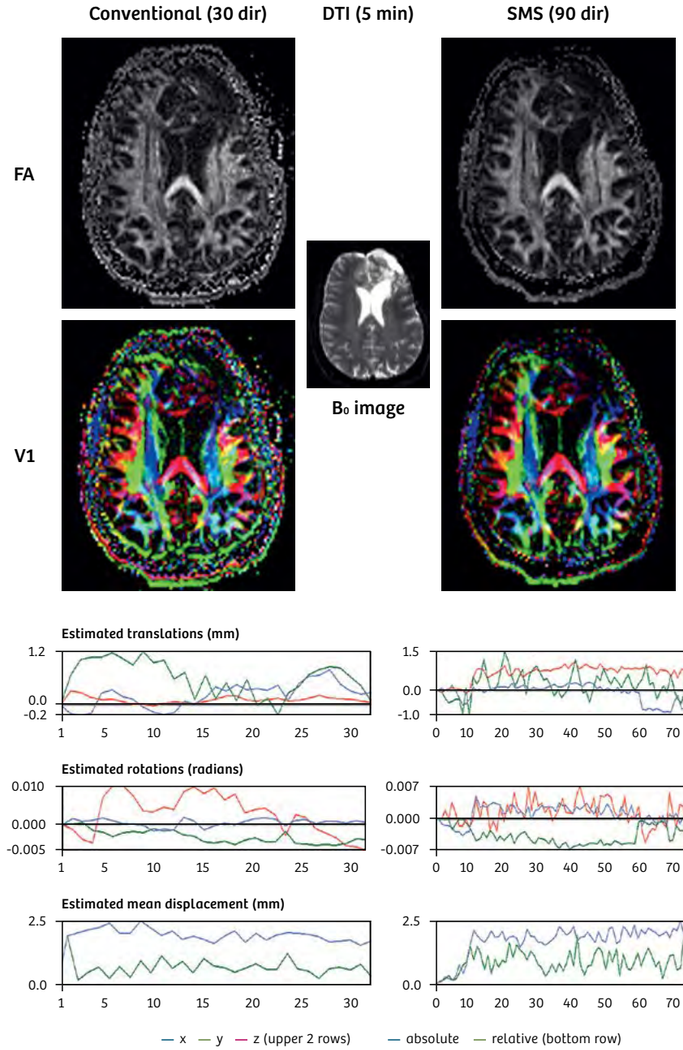

1 Comparison of conventional (30 diffusion encoding directions) vs. SMS DTI (90 directions; SMS factor 3), both recorded with whole-brain coverage at 1.8 mm isotropic in 5 min, in a patient with a partially resected, left frontal oligodendroglioma (same slice position but scans not coregistered). Online-generated FA **(top)** and color-coded V1 maps **(middle)** illustrate less noisy estimates from more sampled diffusion directions by SMS. Between-volume motion tends to be slightly lower for SMS compared to conventional DWI **(bottom)**. A subdural hygroma abutting the left frontal lobe is apparent in the middle image with no diffusion but T2-weighting.

Introduction

Simultaneous multi-slice (SMS) imaging accelerates the temporal sampling of MRI and enables unprecedented increases in temporal resolution. This is of interest not just for research, but for various clinical applications that are currently emerging.

Dense temporal sampling by SMS offers new insights into temporal dynamics when time-series are studied and has been shown to improve the sensitivity of resting-state fMRI, for example (cf. the corresponding article by Miller et al. in this issue; [15, 19]). At the same time, it can be used to encode more information in diffusion MRI (e.g.,by recording more diffusion directions; Fig. 1), to shorten acquisition times, or to increase spatial image resolution and / or coverage [8, 10, 18]. While SMS imaging is applicable to different pulse sequences such as echo-planar imaging (EPI) and turbo spin echo (TSE), it has gained particular attention for BOLD fMRI and diffusion EPI. While SMS-accelerated EPI may be able to increase statistical confidence and / or to reduce experimental scan duration of clinical BOLD fMRI (see Fig. 2 in this article; Figs. 4, 5 of the article by Miller et al. in this issue), the benefit of fast temporal sampling becomes particularly apparent for diffusion EPI. Here, multidirectional (MDDW) and high-angular resolution diffusion-weighted imaging (HARDI), possibly across multiple b-value shells, are instrumental for diffusion-tensor (DTI; Fig. 1) or -kurtosis imaging (DKI) and tractography (Figs. 2, 3, 5, 6). For example, recording 3 times more unique diffusion directions by SMS within the same period of time compared to conventional DTI can reduce the noise in fractional anisotropy (FA) and color-coded first eigenvector (V1) maps (Fig. 1, top).

For DWI requiring just 3 diffusion-encoding directions (e.g., stroke or epidermoid imaging), there is, in terms of acquisition speed, relatively little to gain: Here, SMS reduces the default imaging time only by a fraction and in the magnitude of 15 to 20 seconds for each whole-brain average. In a busy practice scanning up to 40 neuroradiological patients in 10 hours, this may enable the examination of one additional patient per day.

For DTI or tractography studies investigating structures with rather uniformly directed diffusion and few crossing fibers, such as in the peripheral nervous system, potential gains offered by SMS are probably less related to sampling more diffusion directions and more to extend the coverage and facilitate isotropic recordings.

For structures in the central nervous system with lots of crossing fibers or tractography into low FA areas, such as perifocal tumor edema [6], sampling more diffusion directions can considerably improve the tracking of the fiber pathways of interest (Fig. 2, bottom). Diffusion tractography nowadays regularly supplements fMRI for pre-surgical planning and intra-operative neuro-navigation, and here SMS allows us to record high-resolution (1.8 mm isotropic) diffusion-weighted (e.g., at b = 1500 s/mm2) whole-brain data of, for example, 160 unique encoding directions in less than 10 minutes while comparable conventional recordings without SMS would normally exceed the scanning tolerance of clinical patients, especially if fMRI is conducted in the same session.

Additionally, faster scanning by SMS imaging may, at least in theory, reduce motion artifacts. Other than motion between consecutive volumes, within-volume motion is usually not correctable. In our experience, estimated motion between EPI volumes tends to be slightly lower for SMS recordings (Fig. 1, bottom). Thereby, SMS may increase the quality of the scans recorded.

For fMRI, SMS changes the auto-correlation structure and 'spin history' effects of the data. Statistical modeling and inference can account for the former, while dense temporal sampling in SMS fMRI makes the data more amenable to denoising procedures to remove effects of the latter. SMS fMRI is attractive for clinical applications considering potential gains in 'functional' signal-to-noise ratios (SNR) that can be achieved at the individual patient level. Assuming that the detected functional signal adds up linearly with each measurement and that the random noise increases with the square root of the number of measurements, the 'functional SNR' would increase by the square root of the number of samples. In other words, if we measure the same functional signal four times and sum up the measurements, we increase the SNR by a factor of two compared to a single measurement. Even though these assumptions are certainly simplistic, SMS is able to boost statistical confidence, and these gains can be invested

I) to render first-level FMRI results more robust (see Fig. 2 in this article; Figs. 4, 5 in the article by Miller et al. in this issue),

II) to increase the spatial resolution of the measurements (see Fig. 4 in the article by Miller et al. in this issue) and/or

III) to shorten the experimental acquisition time (see Fig. 5 in the article by Miller et al. in this issue).

Increasing the spatial resolution of fMRI and diffusion tractography is relevant for clinical applications to improve spatial accuracy, including registration to anatomical scans, but penalized by a loss in SNR because the measured signal decreases approximately linearly with the voxel size.

[1]*MR scanning has not been established as safe for imaging fetuses and infants under two years of age. The responsible physician must evaluate the benefit of the MRI examination in comparison to other imaging procedures.*

Additionally, the relative contribution of thermal noise increases nonlinearly at higher spatial resolutions. This is also the reason why task-based SMS fMRI data tend to require a similar amount of smoothing like low-resolution recordings to achieve comparable results [11]. However, recent statistical advances specifically addressing pre-surgical fMRI indicate that the potentially detrimental effects of smoothing (blurring of larger or elimination of smaller activations, leading to false-positive or -negative detections in space) can be avoided [16].

Given that patients (especially children1, elderly, neuropsychologically impaired, mentally handicapped and those suffering from intractable epilepsies) often have a limited tolerance for long scan durations, the potential benefits of SMS-accelerated scanning to obtain high-quality data are substantial. At the same time, there is no obvious drawback: Auditory noise characteristics are the same for conventional and SMS EPI (with the fundamental frequency peak being determined by the echo spacing of the read-out gradient, [5]), and the risk for peripheral nerve stimulations (due to rapid read-out gradient switches) should not be increased. In fact, we have not observed an increased number of such incidents with SMS over the past three years.

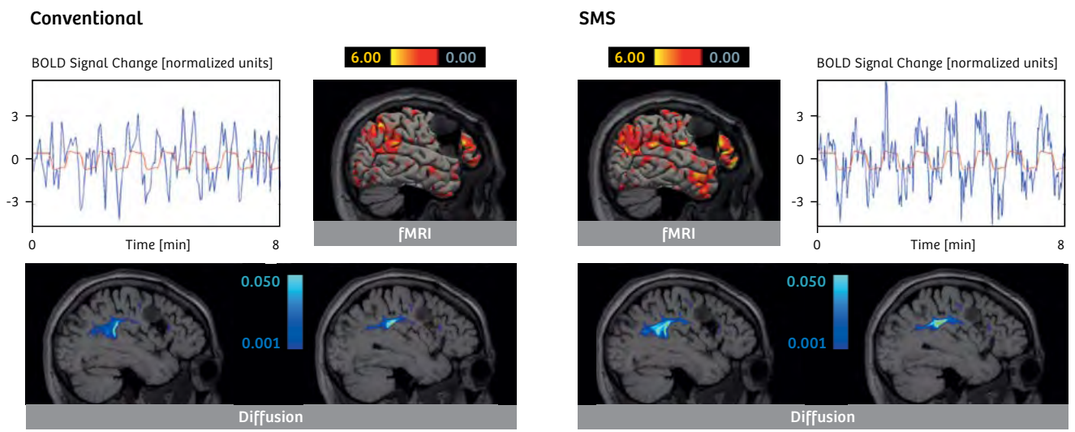

2 Comparison of conventional vs. SMS BOLD fMRI (**top**; TR 3.0 vs. 1.5 secs) and diffusion tractography (**bottom**; 60 vs. 180 directions; distortion-corrected by phase reversal – cf. Fig. 3) in a left-hander with a recurrent, right frontal low-grade glioma prior to second surgery. Doubling the temporal fMRI resolution by SMS increased the statistical confidence (red-to-yellow Z-statistics obtained by independent component analysis ICA / dual regression) of the activations correlated with the language paradigm and improved the temporal correlation of the respective time-courses (blue) with the model (red; r = 0.2 vs. 0.7; **top**). Similarly, tripling the number of diffusion directions by SMS increased conditional probabilities to reconstruct streamlines of the superior longitudinal / arcuate fascicle (blue-to-light blue, thresholded at 1 ‰ of the number of samples making it from seed to target [6]; **bottom**).

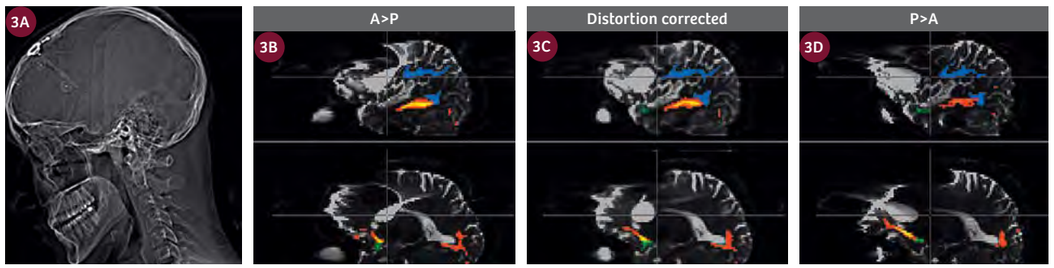

3 Distortion correction by SMS SE-EPI using alternate phase encodings (A>P **(3B)** vs. P>A **(3D)**). Patient with a left fronto-opercular cystic ganglioglioma, craniofix and Ommaya reservoir **(3A)**. Probabilistic tractography of SMS DWI with the arcuate **(blue-to-lightblue)**, inferior longitudinal **(red-to-yellow)** and uncinate **(green-to-lightgreen)** fascicle. Note distortion of the tumor cyst depending on the phase-encode direction and the resulting neuro-navigation error as indicated by the cross hairs.

Therefore, pre-surgical BOLD fMRI and diffusion tractography are prime examples of where the use of SMS-accelerated EPI is expected to translate into obvious clinical advantages, and we have decided to share our experience with this new technology in this context based on selected cases.

Case-based illustrations of SMS benefits

Head-to-head comparisons of conventional vs. SMS fMRI and diffusion-weighted EPI were performed in Figures 4 and 5 of the article by Miller et al. in this issue and in Figures 1 and 2 of this presentation. Figure 2 illustrates the core findings:

Recording more time points and more diffusion directions by SMS acceleration is able to enhance the statistical confidence of fMRI and diffusion tractography results. Such improvements may lead to increased spatial extent and maximum height probabilities to detect functional activations and structural connectivities. In other words, SMS can improve the sensitivity of functional and diffusion MRI. Sensitivity is crucial for pre-surgical fMRI and tractography applications because most of these aim to avoid infliction of new clinical deficits to the patient by minimizing false-negative detections.

Cerebrovascular Reactivity Mapping (CVRM)

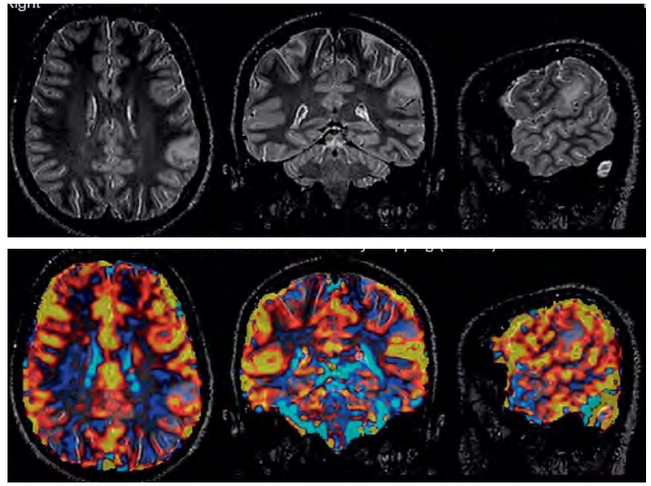

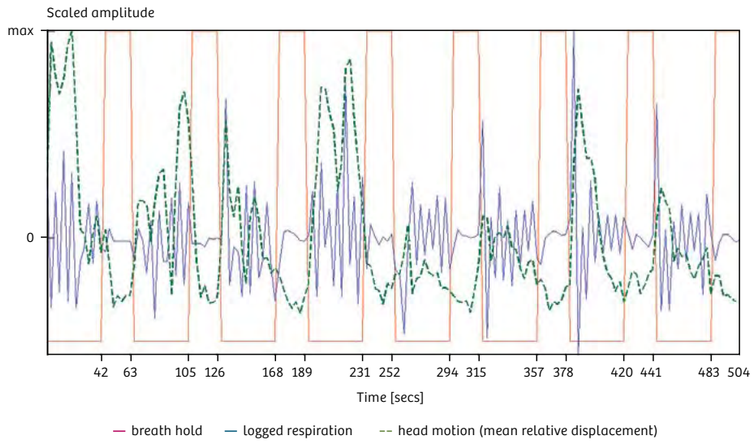

4 Cerebrovascular reactivity mapping (CVRM) by SMS BOLD fMRI, same patient as in Fig. 4 of the article by Miller et al. in this issue.
Top: SMS identified reduced cerebrovascular BOLD reactivity of the left supramarginal focal cortical dysplasia (FCD).
Bottom: Logged respiration (blue) by Siemens' proprietary physiological monitoring confirmed patient compliance with breath-hold commands (red), motion correction estimates reveal increased head motion (green) during free breathing.

For the patient shown in Figure 2, right-brain speech had already been confirmed by intra-operative electrical stimulation mapping (ESM) during the primary, partial tumor resection. However, ESM was, at the time, complicated by a series of intra-operative seizures, and the current fMRI examination prior to secondary resection was considered helpful in supporting a sufficient safety margin between the recurrent, low-grade glioma and cortical fMRI activations (Fig. 2, top). Probabilistic diffusion tractography revealed the proximity of the arcuate fasciculus (AF) to the upper medial tumor nodule, with SMS suggesting a smaller safety margin than conventional diffusion tractography (Fig. 2, bottom). We regularly provide these data to the operating neurosurgeon for transfer into the neuro-navigation system. It is useful to define ESM points and to tailor the neurosurgical approach to the functionally relevant anatomy.

Figures 3–6 further illustrate the application of SMS to pre-surgical fMRI and tractography. Distortion correction of BOLD and diffusion-weighted EPI is essential for accurate pre-surgical planning and intra-operative neuro-navigation, particularly in patients with

I) lesions close to the skull base and

II) previous surgery, craniofix and metallic implants (Fig. 3). SMS spin- echo (SE-) EPI is currently the fastest means to acquire field map data for distortion correction by alternate phase encodings. Figure 3 illustrates the profound neuro-navigation error that may result if geometric distortions are not adequately corrected for.

Figure 4 depicts the same patient as in Figure 4 of the article by Miller et al. in this issue.Here, SMS BOLD fMRI was used for cerebrovascular reactivity mapping (CVRM) [17]. The incidentally detected, left supramarginal focal cortical dysplasia (FCD) without transmantle sign, which was initially mistaken for a low-grade glioma but then shown to lack any spectral tumor pattern, revealed reduced BOLD signal changes in response to hypercapnic fluctuations evoked by simple breath holding.

Abolished or decreased cerebro-vascular reactivity may increase false-negatives of cognitive task-based and resting-state fMRI results. Based on SMS mapping of speech and language functions, however, the lesion was considered to occupy an eloquent location in the dorsal stream [12], a conclusion indeed primarily supported by SMS but not conventional BOLD fMRI (cf. Fig. 4 of the article by Miller et al. in this issue). Follow-up of the lesion with reduced mechanical compliance established by MR elastography [7, 9] over the past two years was stable and resection was therefore not recommended.

Figure 4 also illustrates the usage of advanced physiological signal monitoring: Respiration, pulse and ECG can all be recorded along with SMS, and Siemens' proprietary implementation logs these signals in precise temporal synchronization with each acquired slice and volume to (pseudo-) DICOM series. From these, the recorded signals can be read out for physiological noise modeling to 'regress out' effects of physiological noise in fMRI, for example. This feature makes physiological signal monitoring very convenient and easy to handle without the need for any third-party equipment. Figures 5 and 6 spotlight the application of SMS fMRI and diffusion tractography to patients with drug-resistant seizures evaluated prior to invasive electrocorticography and epilepsy surgery.

Epilepsy differs from tumor surgery in that patients with intractable seizures but with no identifiable brain lesions and no pre-surgical neurocognitive impairments (such as the case in Fig. 6) are at particular risk to develop new postsurgical deficits. In contrast, for patients who undergo surgical resections of brain tumors or other intra-axial lesions, those with no pre-surgical deficits generally fare best (such as the case in Fig. 2).

The patient shown in Figure 5 is the case of a 9-year-old, handicapped boy with classical Sturge-Weber syndrome (Figs. 5A, B) evaluated prior to left hemispherotomy considered for surgical treatment of refractory seizures. Absent visual resting-state fMRI signal fluctuations in the primarily affected left hemisphere (Fig. 5C) reflected right visual field hemianopsia of the patient. Speech mapping (passive story listening vs. scrambled sounds) with SMS BOLD fMRI detected predominantly right hemispheric activations (Fig. 5D), using both general linear modeling (GLM; model time-course in green) and independent component analysis (ICA) with spatial mixture modeling (MM) for statistical inference [20]. Right-brain speech was later confirmed by left intra-carotid WADA testing and corresponded to degeneration of the left arcuate fasciculus (AF), especially in the posterior segment, detected by probabilistic SMS diffusion tractography (Fig. 5E). Similarly, the left corticospinal tract showed signs of degeneration that corresponded to the patient's right hemi-paresis (and impeded unbiased handedness evaluation). Left hemispherotomy was successfully performed (Fig. 5F), effectively eliminating the previous frequent seizures, and did not result in aphasic complications but just slight worsening of the hemiparesis. Rapid temporal sampling by SMS was instrumental to minimize the acquisition time for BOLD fMRI and diffusion tractography (< 30 min) obtaining high-quality data (280 fMRI time-points, 320 diffusion directions) without exceeding the scanning tolerance of the patient.

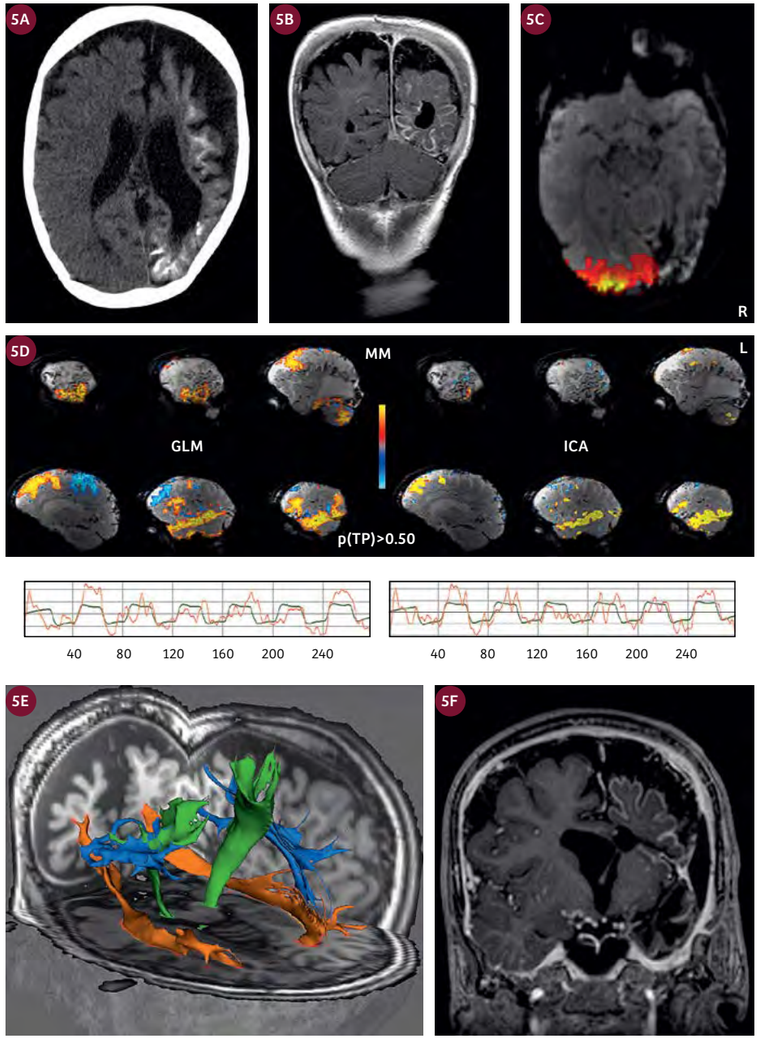

5 SMS BOLD fMRI and diffusion tractography in a boy with Sturge-Weber syndrome prior to surgical treatment of refractory seizures. Pathognomonic CAT **(5A)** and contrast-enhanced T1-weighted MRI **(5B)** scans revealing left leptomeningeal angiomatosis and intra-axial calcifications. SMS BOLD fMRI detected no signal fluctuations of visual resting-state networks in the degenerated left occipital lobe, corresponding to a right visual field hemianopsia of the patient **(5C)**. Speech mapping by SMS BOLD fMRI suggested right hemispheric language lateralization **(5D)**. SMS diffusion tractography **(5E)** indicated degeneration of the left arcuate (AF; **blue**) and pyramidal (**green**) tract, while the left inferior fronto-occipital fasciculus (IFOF; **orange**) seemed largely intact. Subsequent left hemispherotomy was successful **(5F)** without aphasic deficits.

Figure 6 illustrates the case of a nonlesional, drug-resistant epilepsy patient, not eligible for WADA testing. He was transferred for best possible non-invasive assessment of language organization / lateralization prior to invasive electrocorticography (ECoG). ECoG was considered to better localize the seizure focus. The 13-year-old left-handed boy suffered from refractory seizures originating in the left frontal lobe (according to scalp EEG) during which he maintained the ability to speak. Using independent component analysis (ICA), speech mapping by SMS BOLD fMRI detected two paradigm-correlated independent components—one lateralized to the triangular part of the right inferior frontal gyrus and another with largely bilateral activations—presumably corresponding to the dorsal and ventral stream of speech and language processing, respectively [12]. Lateralization of the dorsal stream fMRI component suggested right-brain speech dominance for articulation, consistent with preservation of expressive speech during left frontal seizures. However, an important limitation is that fMRI cannot discriminate essential from dispensable (co-)activations by itself. Therefore, we sought to substantiate right-brain speech dominance by relating the functional to structural connectivity profiles

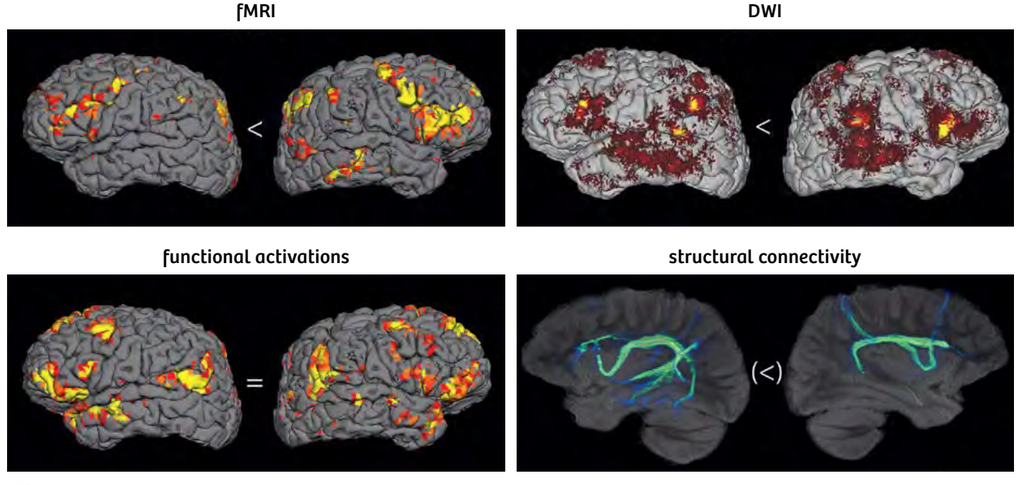

6 SMS BOLD fMRI and diffusion tractography in a left-handed boy with no apparent lesion (according to structural MRI) but drug-resistant, left frontal lobe seizures. Speech mapping by SMS BOLD fMRI **(left)** detected two paradigm-correlated components: one right-lateralized **(top left)** and another bilateral **(bottom left)**. SMS diffusion tractography **(right)** revealed spatial cross-correlation of right triangular activation probabilities with association fiber projection probabilities of the arcuate fasciculus **(top right)**. Its anterior segment was hypoplastic on the left **(bottom right)**. Right Broca's dominance was considered likely, invasive left frontal electrocorticography (ECoG) was recommended to further localize the seizure focus.

[6, 13]. Probabilistic SMS diffusion tractography revealed a highly significant correspondence of right-lateralized fMRI activations with right triangular projections of the arcuate fasciculus (AF) which was not significant on the left. On the left, the anterior segment of the AF was hypoplastic. This case exemplifies a sophisticated clinical application of joint fMRI and diffusion analysis. SMS was essential to generate the underlying high-resolution data (1.8 mm isotropic) at a minimal scan time (25 min) adjusted to reduced scan compliance of the patient.

Conclusions

The case studies presented here make it evident that SMS is ready to be transferred into clinical practice. We have illustrated that SMS can increase the statistical confidence of fMRI and diffusion tractography results. This is in itself very valuable. These gains may also be used to increase spatial image resolution and coverage, to improve spatial coregistration to high-resolution anatomical scans for intra-operative neuro-navigation, and / or to shorten acquisition times. Eventually, SMS may allow us to better tailor pre-surgical fMRI and tractography to individual limitations of task performance and scanning tolerance of the patients we care for.

Pre-surgical fMRI and diffusion tractography will take advantage of this exciting new technology. In terms of auditory scan comfort, despite an increased specific absorption rate (SAR), or unwanted peripheral stimulations, no penalties are involved. Dense temporal sampling of SMS may also be of clinical interest for real-time fMRI applications, where the gains could be substantial, and potentially to better differentiate vegetative from minimally conscious states or locked-in patients. However, benefits for such clinical applications have yet to be evaluated.

Over the past decade, pre-surgical fMRI and diffusion tractography have hardly kept up with the rapid methodological advancements in the field. Pre-surgical tractography, for example, often continues to rely on 6 or 12 diffusion directions only – even though it has been demonstrated that at least 30 unique sampling orientations are required for a robust estimation of diffusion tensor orientations [14]. Current guidelines of the American Society for Functional Neuroradiology (ASFNR) do not specify a firm minimum of unique diffusion encoding directions for clinical DTI and tractography or provide a recommended set of pre- and post-processing algorithms to be used [2]. Similarly, Current Procedural Terminology (CPT) codes of the American Medical Association (AMA) for clinical fMRI [2] and practice guidelines for fMRI by the American College

of Radiology (ACR) [1] make no reference to recommended data acquisition and analysis strategies to assure appropriate conduct for fMRI exams. Unfortunately, clinical settings tend to strongly favor speed over sensitivity and accuracy in data acquisition and analysis. SMS seems a perfect tool to overcome exactly these shortcomings.

Overall, SMS provides a showcase for capitalizing on recently developed, advanced data acquisition and analysis strategies that lead to tangible benefits in research [10, 15, 19] and clinical practice. It is able to facilitate patient-specific applications to optimize clinical decision-making [4] and to translate technological cutting-edge progress into medical practice. In this regard, SMS is a versatile 'kick' for functional and diffusion MRI to finally become much more than just fashionable merely by virtue of 'colored brain images'.

Acknowledgements

… to Siemens Healthcare GmbH, Germany (Thomas Beck, Thorsten Feiweier and Heiko Meyer, in particular), and the Center for Magnetic Resonance Research (CMRR) of the University of Minnesota, USA (Edward Auerbach, Steen Moeller and Essa Yacoub, in particular), for the opportunity to use their SMS EPI implementations and the excellent support.

… to the Oxford Centre for Functional MRI of the Brain (FMRIB) and the Laboratory for Computational Neuroimaging of the Martinos Center for Biomedical Imaging at MGH / Havard University Boston, USA, for the outstanding software (FSL & FreeSurfer) they are developing. I have used it with great clinical benefits for my patients.

… to Optoacoustics', Israel (http://www.optoacoustics.com/), supreme Active Noise Cancellation (ANC) system to cancel out EPI read-out noise making both fMRI as well as diffusion scanning much more comfortable. For fMRI it also greatly improves auditory stimulus trans-mission. Data shown in Figures 5, 6 were recorded using ANC (and these patients would have hardly tolerated unattenuated EPI noise).

References

[1] American College of Radiology (ACR), 2007: http://www.asfnr.org/wp-content/uploads/fMRI-Clinical-Guidelines.pdf.

[2] American Society for Functional Neuroradiology (ASFNR), 2012: http://www.asfnr.org/wp-content/uploads/ASFNR-Guidelines-for-DTI.pdf and http://www.asfnr.org/cpt-codes/.

[3] Anderson, J. L. R. (2014). Geometric distortions in diffusion MRI. In: Diffusion MRI: from quantitative measurement to in-vivo neuroanatomy. Johansen-Berg, H. & Behrens, T. E. (Eds.), 2nd edition, Elsevier Academic Press, Amsterdam (ISBN 978-0-12-396460-1), 2014. pp. 63-85.

[4] Bartsch, A. J., et al., Diagnostic functional MRI: illustrated clinical applications and decision-making. J Magn Reson Imaging, 2006. 23: 921-932.

[5] Bartsch, A. J., et al., Scanning for the scanner: FMRI of audition by read-out omissions from echo-planar imaging. NeuroImage, 2007. 35: 234-243.

[6] Bartsch, A. J., et al., Presurgical tractography applications. In: Diffusion MRI: from quantitative measurement to in-vivo neuroanatomy. Johansen-Berg, H. & Behrens, T. E. (Eds.), 2nd edition, Elsevier Academic Press, Amsterdam (ISBN 978-0-12-396460-1), 2014. pp. 531-568.

[7] Bartsch, A.J., et al., Erratum to: State-of-the-art MRI techniques in neuroradiology: principles, pitfalls, and clinical applications. Neuroradiology, 2015. 57(10):1075.

[8] Feinberg, D. A., et al., Multiplexed echo planar imaging for sub-second whole brain FMRI and fast diffusion imaging. PLoS One, 2010. 5(12): e15710.

[9] Gallichan, D., et al., TREMR: Table-resonance elastography with MR. Magn Reson Med, 2009. 62(3): 815–821.

[10] Glasser, M. F., et al., The minimal preprocessing pipelines for the Human Connectome Project. NeuroImage, 2013. 80:105-24.

[11] Harms, M. P., et al., Impact of multiband EPI acquisition in a simple FMRI task paradigm analysis. OHBM (Human Brain Mapping Conference), 2013. 3448.

[12] Hickok, G., et al., The cortical organization of speech processing. Nat Rev Neurosci, 2007. 8: 393-402.

[13] Homola, G. A., et al., A brain network processing the age of faces. PLoS One, 2012. 7: e49451.

[14] Jones, D. K., The effect of gradient sampling schemes on measures derived from diffusion tensor MRI: a Monte Carlo study. Magn Reson Med, 2004. 51: 807-815.

[15] Kalcher, K., et al., The spectral diversity of resting-state fluctuations in the human brain. PLoS One, 2014. 9(4):e93375.

[16] Liu, Z., et al., Pre-surgical fMRI Data Analysis Using a Spatially Adaptive Conditionally Autoregressive Model. Bayesian Analysis, 2015. http://projecteuclid.org/euclid.ba/1440594946.

[17] Pillai, J. J., et al., Cerebrovascular reactivity mapping: an evolving standard for clinical functional imaging. AJNR Am J Neuroradiol, 2015. 36(1):7-13.

[18] Setsompop, K., et al., Blipped-controlled aliasing in parallel imaging for simultaneous multislice echo planar imaging with reduced g-factor penalty. Magn Reson Med, 2012. 67: 1210-1224.

[19] Smith, S. M., et al., Resting-state fMRI in the Human Connectome Project. NeuroImage, 2013. 80: 144-168.

[20] Woolrich, M., et al., Mixture Models with Adaptive Spatial Regularisation for Segmentation with an Application to FMRI Data. IEEE Trans. Medical Imaging, 2005. 24(1):1-11.

Contact
Andreas Joachim Bartsch, M.D.
bartsch@radvisory.net

Simultaneous Multi-Slice Imaging for Resting-State fMRI

Karla L. Miller[1]; Andreas J. Bartsch[1,2]; Stephen M. Smith[1]
[1]Oxford Centre for Functional MRI of the Brain (FMRIB), University of Oxford, UK
[2]Departments of Neuroradiology, Universities of Heidelberg and Würzburg, and Radiologie Bamberg, Germany

Background

Functional MRI (fMRI) is a primary tool in neuroscience that enables non-invasive detection and characterization of brain activity. fMRI is often described in terms of spatial 'mapping'; importantly, however, fMRI experiments encode information about brain activity in the temporal domain. Echo-planar imaging (EPI) has therefore been crucial to this development by enabling temporal resolution (TR) of several seconds per whole-brain image volume. Nevertheless, the encoding of activity in the temporal domain means that fMRI data quality is fundamentally tied to temporal resolution. It is therefore notable that a typical fMRI experiment with TR = 3 s may encode hundreds of thousands of voxels, but can only achieve 200 time points in 10 minutes. The advent of parallel imaging has enabled reduction of image distortions in EPI; however, unlike many structural MRI techniques, parallel imaging 'acceleration' has little effect on volume scan times in fMRI.

Temporal resolution in fMRI has until recently remained directly proportional to the number of slices (TR = 2-3 s). The explosion of simultaneous multi-slice (SMS, also known as multiband) technology in the past 5 years, described in detail elsewhere in this issue, has now removed the strict coupling between the number of slices and the temporal resolution. The dense temporal sampling enabled by SMS techniques can enormously benefit our ability to identify which voxels are activated by a task or define regions that spontaneously co-activate in resting-state fMRI, provided other aspects of data quality are not unduly compromised. The source of these gains is somewhat complex, and we therefore go into some detail on this point below.

In this article, we will focus in particular on the benefits SMS has to offer for resting-state fMRI. In resting-state fMRI [1, 3], intrinsic signal fluctuations are used to identify connectivity patterns in the brain under the (now well-established) hypothesis that connected brain regions will co-fluctuate in activity level even in the absence of an experimentally imposed task (Fig. 1). A given neural network would thus be characterized by a common time course of activity that is shared within the

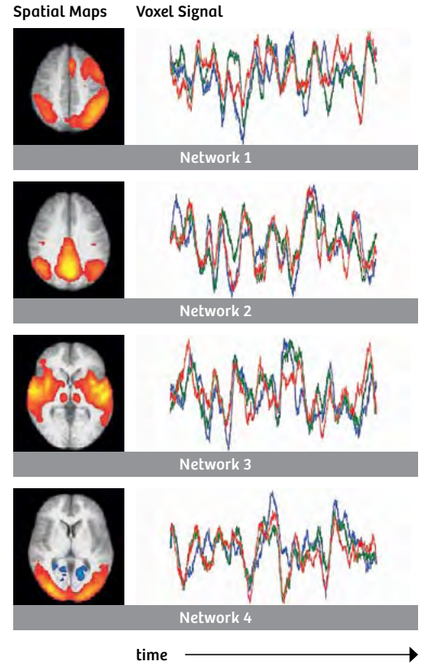

1 Resting-state fMRI identifies patterns of connectivity across the brain based on spontaneous fluctuations of the BOLD signal (in the absence of an experimentally-induced mental or cognitive state). Each map represents the spatial distribution of one brain network, with example voxel time courses depicted in the color plots to the side. Brain networks are inferred by identifying voxels that share a common time course (e.g. are temporally correlated), as simulated here. The centrality of the time domain for identifying networks makes SMS acquisition a powerful technology for resting-state fMRI.

[1]This simplistic description of independent time courses would only strictly hold if the brain was composed of isolated networks. In practice, the picture is more one of networks that are more and less tightly coupled, representing a hierarchy of connectivity that is reflected in the degree to which time courses are shared.

network and largely independent of activity outside the network[1]. Many resting-state studies aim to capture the dynamics of a rich set of networks, placing even greater demand on the temporal domain than simple tasks with pre-defined timings. Moreover, dense temporal sampling has the potential to reveal subtle aspects of these networks, such as transient connectivity. We discuss the role that SMS has to play in achieving these goals.

Benefits of high temporal resolution for resting-state fMRI

Statistical benefits of fast sampling

One fundamental characteristic of fMRI is that the blood oxygenation level-dependent (BOLD) response to neural activity is relatively sluggish, as described by the blurred hemodynamic response function used to model the BOLD response to a task. It may seem at first as if there is little to be gained from sampling a slowly-varying signal faster than is necessary to characterize its basic temporal features. This intuition would seem to be supported if one compares the size of BOLD signal change to the standard deviation of the measurement noise (the contrast-to-noise ratio), for which the density of samples has little effect.

Critically, however, the statistical tests used to identify brain activity as 'above threshold' depend on both the noise level and the number of independent measurements. Increasing the number of time points reduces the influence of noise on estimates of BOLD signal change in much the same way that averaging of repeated measurements reduces noise. That is, an increased number of time points drives an improved estimate of the noise, even if the signal is much smoother than the temporal sampling rate. From this perspective, it is clear that the achievable benefits depend on the specific properties of the noise, which is inextricably linked to signal modeling.

fMRI analysis most typically decomposes the measured data into modeled 'signal' and noise 'residuals' (defined as the component of the measured data that is unexplained by the signal model). A simple regression analysis of task fMRI might fit one regressor time series matching a pre-defined task to each voxel's measured time course. More sophisticated analyses can include multiple regressors to account for independent cognitive processes, as well as artifactual fluctuations such as physiological variations or movement. In all cases, a voxel's residuals would be given by the difference between the complete model fit (including all regressors) and the measured data.

Inclusion of a larger number of regressor time courses by definition reduces the 'noise' residuals; but intuitively, there is a limit to the number of regressors that can be usefully fit. This intuition is partly quantified by the temporal 'degrees of freedom', which is essentially the number of data points available to the regression[2]. SMS can directly increase the degrees of freedom by enabling more time points in a given experimental duration, thereby boosting statistical significance.

This is a key insight into the role of SMS in fMRI: Acquiring more samples per unit time increases degrees of freedom and supports fitting of an increased number of regressors; conversely, experiments with a small number of regressors are intrinsically high degrees-of-freedom and therefore have less to gain from SMS in a statistical sense.

Resting-state fMRI analysis

In task fMRI, the timing of a given cognitive, sensory or motor process is controlled. By comparison, resting-state fMRI analyses must empirically determine the time course of any resting-state network (RSN) of interest. There are broadly two approaches to this problem: 'seed' analyses extract the desired time course based on pre-specified anatomy, whereas data-driven 'multivariate' analyses decompose the data set as a whole into network components based on certain criteria of interest.

Seed analysis is at heart similar to the regression described above for task fMRI. Investigators specify a seed voxel or region that they know to be part of a network of interest, from which a characteristic time series is extracted. This time series is then used in the same way as a task regressor to identify voxels that share this time course, representing brain areas with connectivity to the seed (i.e. RSNs) [3]. This concept can be extended to multiple networks by defining a set of seed regions and extracting the unique time series from each region using multiple regression. For example, in the 'dual regression'[3] approach [5], network maps from a population brain atlas are used to extract subject-specific time courses, which are then used in a multiple regression to define subject-specific spatial maps for each RSN (typically 10s of networks).

Multi-variate analyses, most notably independent component analyses (ICA), are fundamentally different from regression. Rather than analyzing each voxel independently with a seed-derived time series, the entire 4-dimensional data set (3D space x 1D time for one subject) is decomposed simultaneously. This analysis aims to holistically identify RSNs as 'modes' (or 'components') of variation in the 4-dimensional data that

[2]More precisely, degrees of freedom is the number of independent time points in the model-fitting residuals, reduced by the model complexity (i. e. the number of regressors).

[3]While dual regression is not typically described as a seed-based technique, it is useful and appropriate to characterize it as such for our purposes.

are in some sense independent. Each mode represents an RSN and is characterized by a canonical time course and its associated spatial map. Temporal ICA aims to identify components based on temporal independence, which this fits with the characterization of networks based on temporal co-fluctuation; alternatively, spatial ICA require that the modes are spatially independent, i.e. non-overlapping. In practice, the fact that most fMRI protocols achieve several orders of magnitude more samples in space than time means that spatial ICA is far more robust than temporal ICA. For ICA, the number of networks that are identified is set by the investigator, and typically in the range of 10-100.

SMS for resting-state fMRI

As in task fMRI, both seed and multi-variate analyses decompose fMRI data into 'signal' (corresponding to RSNs) and noise residuals. Hence, we can apply similar arguments regarding the benefits of SMS for resting-state fMRI based on the degrees of freedom, considering both the complexity of the model (number of RSNs) and the number of independent noise measurements. For example, the most common seed-based analysis includes only a few regressors, and thus has intrinsically high degrees of freedom even without SMS. Seed-based analyses will therefore have little to gain from SMS in many situations, although SMS may be beneficial to seed-based analyses in clinical applications if it can confer reduced scan times.

The potential of SMS is at its greatest when a large number of RSNs are considered, for example in dual regression. As originally defined [5], the first stage of dual regression uses ICA to derive a group-wide atlas of RSN spatial maps, potentially parcellating the entire cerebral cortex. Alternatively, the dual regression approach can utilize a network atlas that is derived from another data set or resource, such as the Human Connectome Project. In either case, the limiting degrees of freedom is at the individual subject level, since it is at this stage that a multiple regression is used to refine each RSN to its subject specific spatial map. The degrees of freedom for this multiple regression is thus determined by the number of time points in each subject's scan and the number of RSNs being studied. In dual regression, the increased degrees of freedom offered by SMS acquisition directly enable consideration of a richer set of networks.

Intrinsically multi-variate analyses like ICA have the potential to decompose fMRI data into hundreds of brain parcels representing a detailed network hierarchy, although more commonly 20-50 RSNs might be identified. The loss of degrees of freedom implied by this relatively large number of components would require a proportionate increase in the number of time points to robustly identify RSNs. Previously, this increase in time points could only be achieved by combining at a group level across a large cohort of subjects (requiring the assumption that brain regions co-align across subjects) or acquiring long time series from a given subject. Increasing the density of temporal sampling using SMS within a more modest experimental duration for a single subject (5-20 minutes) can therefore directly enable a more detailed analysis of a network hierarchy, such as the temporal functional modes [6] and clinical applications described below.

Resting-state fMRI in practice

The gains described above can be leveraged in several ways to improve the quality of resting-state fMRI data. First, for a fixed duration of experiment, the increased degrees of freedom confers statistical benefit, which may be useful for detecting subtle differences between networks or for a more fine-scale differentiation of a given network. Alternatively, one can leverage this statistical advantage to combat the reduced SNR associated with smaller voxels to achieve gains in spatial resolution. Finally, one could reduce scan time in the face of limited subject compliance, with clinical applications in particular having much to gain. This final goal is directly enabled by SMS up to a point; however, resting-state fMRI acquisitions must be long enough to observe brain networks in a broad range of its repertoire of 'states'.

Large-scale population studies

Several neuroimaging initiatives have been launched in recent years that aim to distribute large-scale databases of resting-state fMRI. These resources share the hypothesis that certain insights into brain function and connectivity can only be gained from a large number of subjects. Resources like the 1000 Functional Connectomes Project [7] achieve large numbers by aggregating many smaller existing studies, with the benefit of low additional cost but requiring researchers to account for heterogeneity across study protocols. An alternate approach is to explicitly acquire large cohorts with a single protocol to maximize data homogeneity and quality. We will briefly high-light the role of SMS in two such prospective studies representing different extremes of data acquisition: the Human Connectome Project (HCP) and the UK Biobank Project.

The HCP Consortium is focused on characterizing connectivity in the brain [8], with the WashU-UMinn consortium focusing on healthy adults and acquiring a range of modalities including resting-state fMRI in 1200 subjects [9]. SMS has been a central technology to the HCP from the outset, and a number of technical developments have arisen from this project in addition to

the data resource (see articles by Uğurbil and Yacoub in this issue). Within the HCP, the benefits of SMS have been intensely optimized to achieve both high spatial and temporal resolution fMRI (2 mm, TR = 0.72 s), with individual subjects undergoing four 15-minute resting-state scans. Subjects undergo a total of 4 hours of imaging, which additionally includes task fMRI, diffusion imaging and anatomical scans, as well as intense non-imaging phenotyping. Data are acquired on a single scanner (representing a pre-cursor to the MAGNETOM Prisma 3T platform) that was designed specifically for this study. The use of state-of-the-art SMS fMRI has enabled the HCP to achieve exquisite data quality for individual subjects, as well as protocol homogeneity over a relatively large, extensively phenotyped cohort.

UK Biobank is an established epidemiological cohort of 500,000 subjects aged 45-75 that has undergone (non-imaging) phenotyping, behavioral/lifestyle measures and genotyping, and will be followed for long-term health outcomes via the UK National Health Service. An Imaging Enhancement study is currently in the pilot phase, and ultimately aims to enlist 100,000 of the existing cohort for imaging, including brain, cardiac and body scans.

Successfully scanning of this cohort over five years corresponds to extremely high throughput: three dedicated centers running 7 days per week, each accumulating 18 subjects per day. The resulting brain imaging protocol is limited to 35 minutes, during which several imaging modalities are acquired (task and resting-state fMRI, diffusion imaging and multiple anatomical modalities). SMS imaging techniques developed for the HCP [10] have been critical to achieving this highly-ambitious goal without requiring significant compromise relative to conventional data quality. The resting-state fMRI protocol achieves 2.4 mm resolution with sub-second sampling (TR = 0.73 s) using an SMS acceleration of 8, enabling 500 time points per subject in just 6 minutes.

Revealing novel aspects of functional connectivity

Coincident with the development of SMS acceleration for fMRI has been an explosion of ambitious resting-state research with respect to both sophisticated data analysis techniques and attempts to probe increasingly subtle aspects of brain function. The benefit of high temporal resolution for resting-state fMRI is likely to extend beyond boosted statistics or improvements in spatial resolution. Here, we highlight one example from our research where

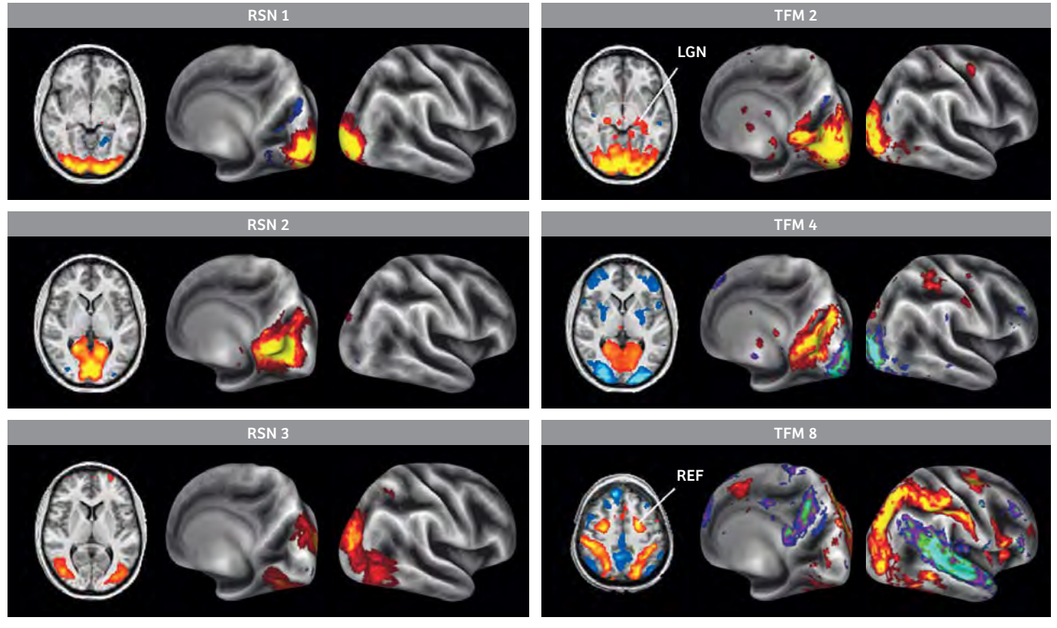

2 Components of the visual system identified from resting-state data using ICA. On the left, spatial independence breaks the occipital lobe into non-overlapping 'resting-state networks' corresponding to early stages of processing of information at the centre and periphery of vision (RSN 1 and RSN 2, respectively), and higher-level visual processing (RSN 3). On the right, temporal independence combines across these areas to identify extended visual networks that correspond to known anatomical support for processes such as low-level visual processing (TFM 2), high vs low visual eccentricity (TFM 4) and the dorsal visual stream (TFM 8). *Reproduced with permission from [2].*

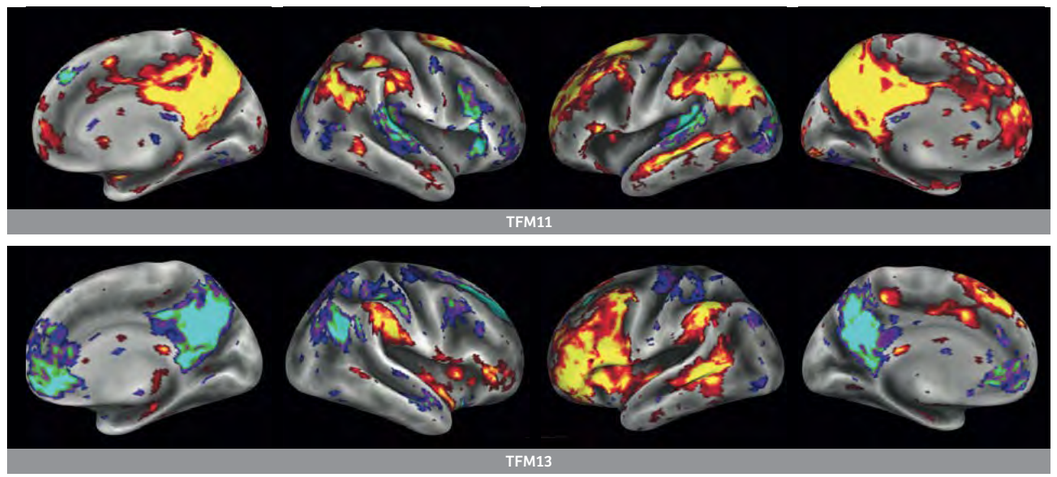

3 High-level cognitive networks identified from resting-state fMRI data on the basis of temporal independence, both including overlap with the well-established 'default mode network' [1]. The network on the top (TFM 11) is reasonably symmetric across hemispheres and involves a set of regions that are involved semantic processing. The network displayed below (TFM 13) contains significant overlap with this semantic network, but is strongly lateralized and includes language regions. *Reproduced with permission from [2].*

SMS has directly enabled novel methodology and preliminary insights into functional connectivity, namely the identification of temporally independent modes of functional activity.

The goal of most resting-state studies is to derive estimates of apparent connection strength between brain regions. While many potential measures of connection strength exist, the most common are based on temporal correlation. Standard approaches parcellate the brain into regions and associated time courses, and estimate the connection strength between a pair of regions based on the correlation between regional time series. Regardless of how the regions are derived (seed- or ICA-based), this approach is underpinned by some problematic assumptions. Temporal correlation is only able to capture the time-averaged behavior of the connectivity between two regions, which would conceal neuroscientifically interesting variations in connection strength over time ('non-stationarities'). Examples include independent networks with spatial overlap (due to interdigitation of neural populations or simply limited spatial resolution), or temporal modulation of physical connections due to processes like attention. In the case of multiple networks that contain a common (overlap) region but are largely independent, the 'networks' identified by both spatial ICA and seed-based approaches are unsatisfying: spatial ICA requires components to be non-overlapping, whereas seed-based analysis identifies all correlated areas as a single network, even if the extended regions do not significantly correlate with each other. These assumptions are problematic, both with respect to basic neuroscience investigations and for clinical applications, particularly pre-surgical planning, as described below.

Identification of more subtle temporal features like the non-stationarities described above, places a strong demand on the temporal domain of the acquired data, which is typically several orders of magnitude smaller than the spatial domain of image voxels. We explored the potential to identify extended brain networks using temporal independence (temporal ICA), in which a brain network would be recognized based on having a unique temporal signature [2]. Unlike spatial ICA, this analysis does not penalize spatial overlap between networks, but it does require a large number of temporal samples to robustly identify these independent time processes. This approach was demonstrated using pilot resting-state SMS data acquired by the HCP. We combined data across five subjects with TR = 0.8 s to accumulate 24,000 time points over 360 minutes. Following careful data clean up (see below), the data was parcellated into 142 regions using spatial ICA, which were then fed into temporal ICA to identify 21 temporally independent functional modes (TFMs). The resulting TFMs contained significant spatial overlap, with most of the spatial ICA parcels contributing significantly to multiple modes. Encouragingly, most of

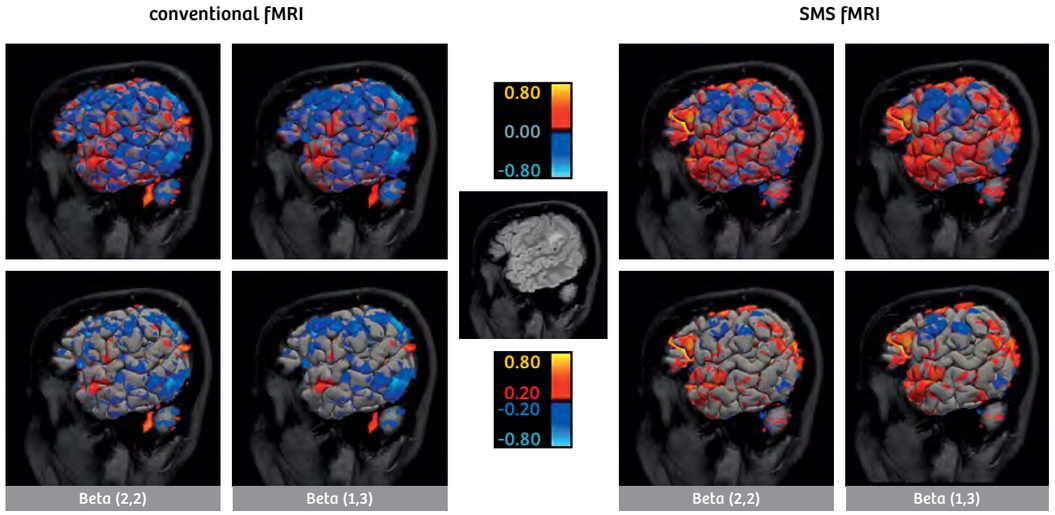

4 Improved single-subject fMRI results with SMS fMRI. Speech mapping data in the same patient, using non-SMS low spatio-temporal resolution (3 mm, TR = 3s) vs. SMS high spatio-temporal resolution (1.8 mm isotropic, TR = 1.5 s, SMS factor 3). Statistical confidence of the SMS results increases remarkably (*top*: unthresholded, *bottom*: thresholded using different Beta priors [14] instead of smoothing kernels), demonstrating that doubling the temporal resolution by SMS over-compensated the reduced SNR at higher spatial resolution. The lesion was an incidentially detected, left supramarginal focal cortical dysplasia (small center image), initially mistaken for a low-grade glioma, with reduced intra- and perilesional cerebrovascular reactivity.

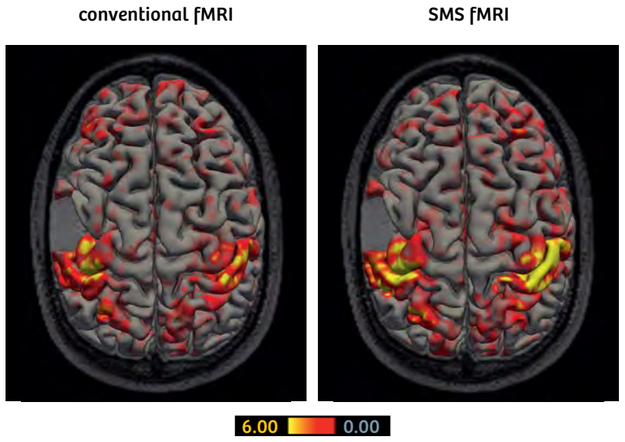

5 Improved (sensori-)motor mapping by SMS resting-state fMRI in a left precentral low-grade glioma prior to resective surgery. The patient suffered from focal motor seizures involving both eyebrows (bilateral N.VII innervation), the contralateral mouth corner (contralateral N.VII innervation), chewing, vocalizations and speech arrest (N.V, IX, X and XII innervation), corresponding to the motor humunculus representation below the handknob. Task-based fMRI would have been confounded by stimulus-correlated head motion potentially causing false-positive detections primarily at the tumor border. Resting-state fMRI reveals statistical gains (color-coded Z-statistics) of SMS high (TR = 1.56 s, SMS factor 3) over non-SMS low (TR = 3.33 s) temporal resolution fMRI, despite the shorter acquisition time (6.5 vs. 14 min).

the TFMs also corresponded to extended networks of known functional anatomy. The visual system was decomposed into well-established streams of visual information processing (Fig. 2), while other TFMs capture high-level cognition such as semantic processing or language (Fig. 3).

Clinical fMRI at the individual patient level

The use of resting-state fMRI in the clinical domain is fairly recent, but has begun to attract attention for clinical applications in general, and for pre-surgical mapping in particular [11, 12]. Resting-state fMRI does not depend on task performance and is less contingent on

patient compliance. It is also less demanding with respect to experimental setup than task-based fMRI and can be more easily acquired by MRI technicians. In some instances, such as when probing orofacial motor functions, task-based fMRI is prone to task-correlated head motion. Furthermore, there is initial evidence that resting-state fMRI data may establish intra- and perilesional BOLD reactivity and thereby serve as a less stressful substitute for cerebrovascular reactivity mapping by experimentally induced hypercapnia [13]. Clinical applications can benefit directly from the increase in statistical significance conferred by SMS, or can leverage statistical gains to increase spatial resolution or reduce scan durations – all of which are extremely desirable for clinical applications.

Increasing the spatial resolution of fMRI improves spatial accuracy, including registration to anatomical scans, but incurs a reduction in SNR proportionate to voxel volume. In some contexts, data quality can be improved through the combined use of high spatial resolution with edge-preserving smoothing to increase SNR, reducing partial volume and signal dropout compared to data acquired at the filtered resolution. However, smoothing can artificially extend or eliminate true activations, both of which are problematic for pre-surgical mapping and intra-operative neuro-navigation. Sophisticated data analysis strategies will thus be required to translate the potential improvements in spatio-temporal resolution with SMS fMRI into clinical applicability [14, 15].

An example of the benefits of increased spatio-temporal resolution by SMS fMRI for language mapping in a patient is given in Figure 4.

Shorter experiments are desirable not only because scan time is precious in the clinical domain, but also considering limitations in task performance and/or compliance in patients. Figure 5 illustrates corresponding gains that can be achieved by SMS for pre-surgical fMRI, exemplified by sensorimotor mapping. These benefits have to be substantiated and systematically explored by future studies. Note that motor mapping is, even in the case of space-occupying lesions, rarely indicated because the sensori-motor strip can be identifiedin most patients by pure anatomic criteria. The real challenge to transfer resting-state fMRI into pre-surgical practice lies in the mapping of 'eloquent' functions with no absolute cortical representation. That is, the meaningful pre-surgical mapping of essential functions whose cortical representations cannot be predicted by anatomic criteria alone, such as speech and language in particular. While it is intrinsically difficult to avoid a circularity of assumptions about the hemispheric representation and dominance of speech and language in this context, recent attempts to relate connectivity gradients from SMS resting-state fMRI to language lateralization in non-clinical samples of the HCP project have been promising [16]. However, task-based pre-surgical fMRI mapping can be performed in 3 to 8 minutes while the recording of these high-quality SMS resting-state data took one hour (see above), and initial efforts to translate such sophisticated analyses to real pre-surgical tumor patients using clinically acceptable scan times of 6 to 13 min have proven difficult. Generally, acquiring high-quality resting-state fMRI data that provide access to subtle information in the spatio-temporal domain (such as robust functional connectivity gradients or TFMs; see above) will continue to require longer scan times than simple task-based fMRI even if SMS acceleration is used.

Cautions, challenges and confounds

Achieving the benefits of SMS in fMRI does require some additional care to protocol design and data analysis. Here we review several common challenges and strategies to overcome them.

High temporal resolution using SMS requires careful consideration of standard analysis pipelines. Residuals are generally assumed to be 'white noise' (with each time point independent of other time points), making any source of structured noise problematic. Violation of this assumption (for example, temporally smooth noise) can cause the residuals to have lower degrees of freedom than anticipated and thereby inflate the apparent statistical significance. At high temporal resolution, it is therefore crucial to account for any structure in the residuals [4]. Most fMRI software packages enable suitable noise corrections, although this may not be a default option.

Fast temporal sampling with SMS will typically reduce the repetition time down to the second or sub-second range, such that the magnetization will not recover fully from one RF excitation to the next. This results in some loss of signal in each individual volume relative to more typical temporal sampling at a rate of 2-3 seconds. Reducing the excitation to the Ernst angle can mitigate these effects, but some signal loss is inevitable. Nevertheless, it is straightforward to demonstrate that the signal loss in a given image volume is more than compensated by the statistical gains described above [17].

Despite the benefits described above, fast sampling is not a panacea for overcoming some limitations of functional MRI based on the BOLD response. Neurovascular coupling, which determines BOLD signal delays, is dependent on region, physiological state and neurovascular pathology. Hence, while faster sampling

enables detection of the BOLD response to neural activity with greater temporal precision, uncertainties in the hemodynamic response mean that it is unlikely to provide the ability to infer neural timings with greater precision [18]. It may, however, enable the detection of subtle temporal features of the hemodynamic response, such as an initial signal reduction (known as the 'initial dip') that has been long hypothesized to provide improved spatial specificity to the locus of neural activity [19].

Another challenge associated with short repetition time is signal instability from 'spin history' effects that disturb the signal steady state, such as caused by subject motion. Motivated in part by recent innovations in SMS technology, machine learning techniques have been developed to automatically 'clean' data by removing these artifacts [20]. These techniques, which have been extensively evaluated within the HCP, can remove much of the signal fluctuations due to physiological noise, hardware instabilities and motion. Indeed, the fact that methods for cleaning data often are based on the same analytical techniques (multi-variate analysis [20] or regression [21]) suggests that SMS data may be more intrinsically amenable to clean-up than conventional non-SMS data.

Conclusions

Simultaneous multi-slice imaging offers enormous potential benefits to functional MRI in general, and resting-state fMRI in particular. These benefits derive primarily from the statistical advantage of increasing the experimental degrees of freedom. For simple tasks, this could enable shorter experiments, but the primary benefit is expected when estimating a number of separate time courses reflecting different aspects of brain function. In resting-state fMRI, experiments that probe a rich hierarchy of brain networks are limited by the degrees of freedom. SMS fMRI can therefore be expected to have particular impact in this area. Several examples of such benefit have been highlighted here, including deployment in large cohorts, unique insights into connectivity and clinical applications.

References

[1] M.E. Raichle, et al., A default mode of brain function. Proc Natl Acad Sci 2001. 98: p. 676-682.

[2] Smith, S.M., et al., Temporally-independent functional modes of spontaneous brain activity. Proceedings of the National Academy of Sciences, 2012. 109(8): p. 3131-3136.

[3] Biswal, B., et al., Functional connectivity in the motor cortex of resting human brain using echo-planar MRI. Magn Reson Med, 1995. 34: p. 537-541.

[4] Bullmore, E., et al., Statistical Methods of Estimation and Inference for Functional MR Image Analysis. Magn Reson Med, 1996. 35(2): p. 261-277.

[5] Filippini, N., et al., Distinct patterns of brain activity in young carriers of the APOE-e4 allele. Proc National Academy of Sciences USA, 2009. 106: p. 7209-7214.

[6] Smith, S., et al., Temporally-independent functional modes of spontaneous brain activity. Proceedings of the National Academy of Sciences, 2012. 109(8): p. 3131-3136.

[7] Biswal, B.B., et al., Toward discovery science of human brain function. Proceedings of the National Academy of Sciences, 2010. 107(10): p. 4734-4739.

[8] Van Essen, D.C., et al., The Human Connectome Project: A data acquisition perspective. NeuroImage, 2012. 62(4): p. 2222-2231.

[9] Smith, S., et al., Resting-state fMRI in the Human Connectome Project. NeuroImage, 2013. 80(C): p. 144-168.

[10] Ugurbil, K., et al., Pushing spatial and temporal resolution for functional and diffusion MRI in the Human Connectome Project. NeuroImage, 2013. 80(C): p. 80-104.

[11] Lee, M.H., C.D. Smyser, and J.S. Shimony, Resting-state fMRI: a review of methods and clinical applications. AJNR Am J Neuroradiol, 2013. 34(10): p. 1866-72.

[12] Kokkonen, S.M., et al., Preoperative localization of the sensorimotor area using independent component analysis of resting-state fMRI. Magn Reson Imaging, 2009. 27(6): p. 733-40.

[13] Zaca, D., et al., Cerebrovascular reactivity mapping in patients with low grade gliomas undergoing presurgical sensorimotor mapping with BOLD fMRI. J Magn Reson Imaging, 2014. 40(2): p. 383-90.

[14] Liu, Z., et al., Pre-surgical fMRI Data Analysis Using a Spatially Adaptive Conditionally Autoregressive Model. Bayesian Analysis, 2015. http://projecteuclid.org/euclid.ba/1440594946.

[15] Johnson, T.D., et al., A Bayesian non-parametric Potts model with application to pre-surgical FMRI data. Stat Methods Med Res, 2013. 22(4): p. 364-81.

[16] Haak, K., et al., Toward assessing language lateralization with resting-state fMRI, in Organization for Human Brain Mapping. 2015. p. 2304.

[17] Feinberg, D.A., et al., Multiplexed echo planar imaging for sub-second whole brain FMRI and fast diffusion imaging. PLoS ONE, 2010. 5(12).

[18] Smith, S., et al., The danger of systematic bias in group-level FMRI-lag-based causality estimation. NeuroImage, 2012. 59: p. 1228-1229.

[19] Hu, X. and E. Yacoub, The story of the initial dip in fMRI. NeuroImage, 2012. 62(2): p. 1103-1108.

[20] Salimi-Khorshidi, G., et al., Automatic denoising of functional MRI data: Combining independent component analysis and hierarchical fusion of classifiers. NeuroImage, 2014. 90: p. 449-468.

[21] Glover, G.H., T. Li, and D. Ress, Image-based method for retrospective correction of physiological motion effects in fMRI: RETROICOR. Magn Reson Med, 2000.

Contact
Karla Miller, Ph.D.
karla@fmrib.ox.ac.uk

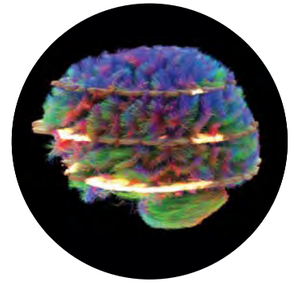

Simutaneous Multi-Slice

A new dimension in MRI speed for clinical routine

usa.siemens.com/sms

Accelerate brain diffusion and BOLD by up to 8x*

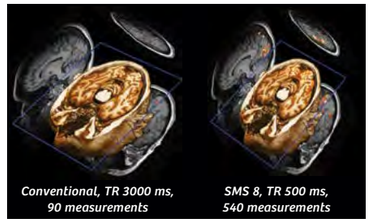

Checkerboard, TE 30, 2 mm iso,
48 slices, TA 4:30 mins
**MAGNETOM Prisma, Head/Neck 64*

Reduce exam time for body diffusion by up to 50%

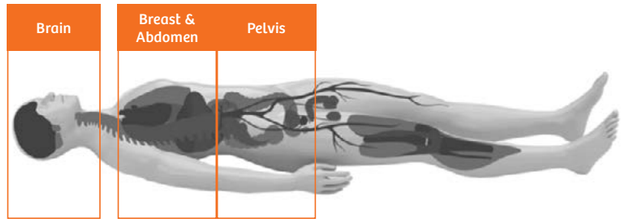

Accelerated exams for advanced neuro and free-breathing body DWI

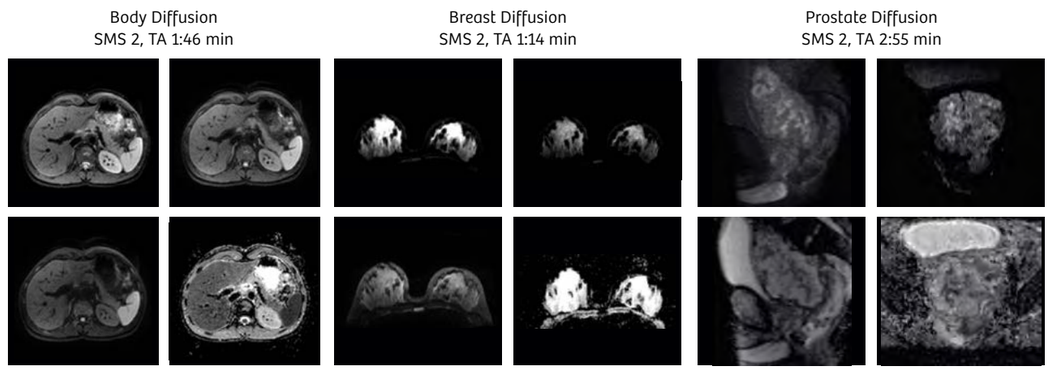

How SMS works

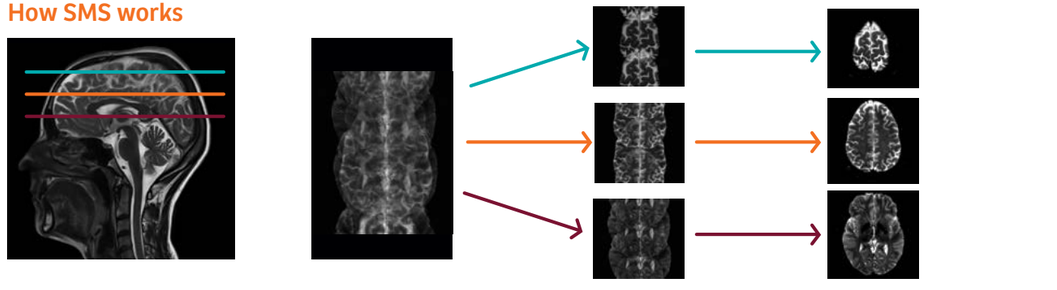

Overview of Magnetic Resonance Fingerprinting[1]

Simone Coppo[1]; Bhairav B. Mehta[1]; Debra McGivney[1]; Dan Ma[1]; Yong Chen[1]; Yun Jiang[2]; Jesse Hamilton[2]; Shivani Pahwa[1]; Chaitra Badve[1]; Nicole Seiberlich[1]; Mark Griswold1,2; Vikas Gulani[1]
Departments of Radiology (1) and Biomedical Engineering (2), Case Western Reserve University, University Hospitals Case Medical Center, Cleveland, OH, USA

Introduction

Magnetic Resonance Imaging (MRI) is a powerful diagnostic tool due to its versatile nature as compared to other imaging modalities, as MRI allows the user to probe and measure various kinds of information (T1, T2, B0, diffusion, perfusion, etc.). However, MRI has the drawback of being slow compared to other diagnostic tools, and is generally qualitative, where the contrast between tissues, rather than absolute measurements from single tissues, is the primary means of information that is used to characterize an underlying pathology.

To overcome this limitation, significant effort has been put into developing quantitative approaches that can measure tissue proprieties such as T1 and T2 relaxation times. Quantifying tissue proprieties allows physicians to better distinguish between healthy and pathological tissue [1] in an absolute sense, makes it easier to objectively compare different exams in follow-up studies [2], and could be more representative of the underlying changes at the cellular level [3, 4] than standard weighted imaging. Additionally, there are various settings in which multiple features such as T1, T2, diffusion, etc. warrant consideration. While quantitative imaging has been a long-standing goal of the MR community, a drawback encountered in early conventional quantitative imaging was the reduced time efficiency compared to qualitative imaging. Early conventional approaches for T1 and T2 mapping involved measuring one parameter at a time. These techniques relied on the acquisitions of several images, each with one specific acquisition parameter that varies for each image while the others were kept constant (Fig. 1A). The obtained images were subsequently fitted with a mathematical model to estimate the one parameter of interest, for example the relaxation time (T1) [8] or the time of signal decay (T2) [9] (Fig. 1B). This process had to be repeated for each parameter of interest. The need for keeping all except one sequence parameter and signal state constant and the limitation of assessing one parameter at a time made these approaches extremely time-inefficient because of the prolonged scan time and thus not suitable for a clinical environment where interscan motion can render such approaches infeasible. In recent times, several approaches have been proposed to shorten the acquisition time [10–13] or to provide combined T1 and T2 measurements [14–18] within a single acquisition. However, major barriers remain to clinical adoption, most notably a simultaneous need for rapid and accurate quantification.

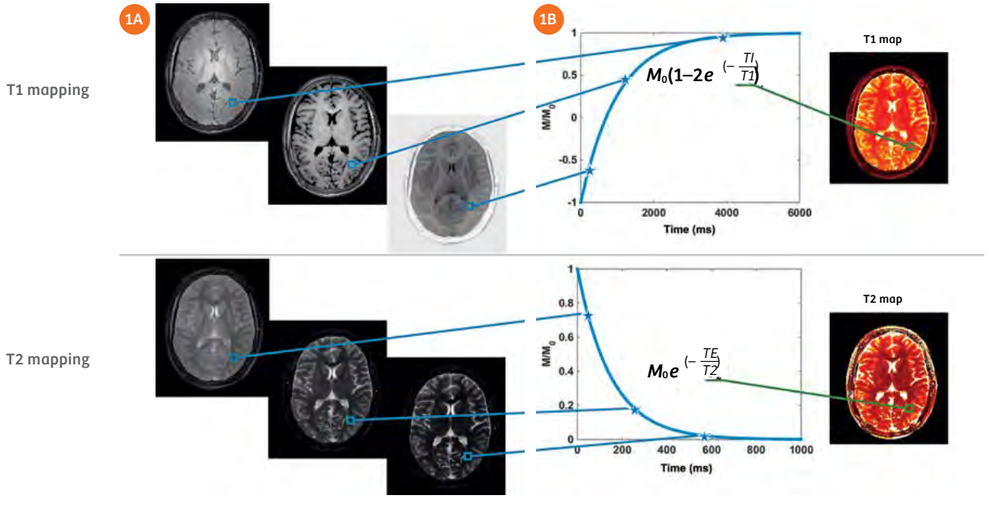

1 Conventional parametric mapping approaches. Example of conventional T1 (above) and T2 (below) mapping techniques. **(1A)** Several fully sampled images are acquired one after the other with different inversion time (for T1) or echo time (for T2). **(1B)** An exponential fitting is performed using the multiple values of each voxel and the relaxation or decay time is the one that provides the best fit.

To overcome the common drawbacks of quantitative imaging, Magnetic Resonance Fingerprinting (MRF)[1] [19–21] has been recently developed. This technique aims at providing simultaneous measurements of multiple parameters such as T1, T2, relative spin density,B0 inhomogeneity (off-resonance frequency), etc., using a single, time-efficient acquisition. MRF completely changes the way quantitative MRI is performed with an entirely different approach from that of conventional techniques. Instead of performing an acquisition with all but one sequence parameter constant, MRF relies on deliberately varying acquisition parameters in a pseudorandom fashion such that each tissue generates a unique signal evolution. It is possible to simulate signal evolutions from first principles using different physical models for a wide variety of tissue parameter combinations, which are collected together in a database called dictionary. After the acquisition, a pattern recognition algorithm is used to find the dictionary entry that best represents the acquired signal evolution of each voxel. The parameters that were used to simulate the resulting best match are then assigned to the voxel. This process is analogous to the fingerprinting identification process used by forensic experts to identify persons of interest. The acquired signal evolution is unique for each tissue and can be seen as the collected fingerprint that has to be identified. The dictionary is equivalent to the database where all the known fingerprints are stored, together with all the information relative to each person. In the forensic case, each fingerprint points to the feature identification of the associated person such as name, height, weight, eye color, date of birth, etc. Similarly, in the case of MRF, each fingerprint in the dictionary points to the MR related identification features of the associated tissue such as T1, T2, relative spin density, B0, diffusion, etc. After the acquisition, the fingerprint contained in a voxel is compared with all the entries in the dictionary. The dictionary entry that best matches the acquired fingerprint is considered a positive match, meaning that the tissue represented in the voxel has been identified. All the known parameters relative to that fingerprint can then be retrieved from the dictionary and assigned to the voxel. The uniqueness of the different signal components and the accuracy with which the dictionary is simulated are two crucial components for the correct estimation of the tissue parameters.

This paper attempts to describe the basic concepts of MRF and illustrate some clinical applications.

Acquisition sequence

Standard quantitative MR imaging approaches require several acquisitions, each one of which constantly repeats the same acquisition pattern, such as radiofrequency excitation angle (flip angle, FA), repetition time (TR) and gradient patterns, until all required data in the Fourier domain (also called k-space) are obtained. Each image is then reconstructed using the Fourier transform and a nonlinear fitting process is applied to each voxel. With MRF, instead, the flip angle, the TR and the trajectory

[1]The product is still under development and not commercially available yet. Its future availability cannot be ensured. As this is a research topic in predevelopment, all results shown are preliminary in nature and do not allow for generalizations or conclusions to be drawn. Product realization and features therein cannot be assured as the product may undergo futher design iterations.

(Fig. 2A, B) vary in a pseudorandom fashion throughout the acquisition; when implemented properly, this generates uncorrelated signals for each tissue, providing the unique fingerprints that are used to recognize the tissue. The initial implementation of MRF [19] was based on a balanced steady-state free-precession (bSSFP or TrueFISP) sequence because of its sensitivity to T1, T2 and off-resonance frequency, and because the steady-state signal generated by this sequence has been thoroughly studied [22]. The FA (Fig. 2A) varies in a sinusoidal fashion to smoothly vary the transient state of the magnetization, ranging from 0° to 60° and from 0° to 30° alternatively, with a period of 250 time points, or images. On top of this signal, a random variation is added to induce differences in the time evolutions from tissues with similar parameters. After each half period (250 images), 50 flip angles are set to 0° to allow for signal recovery. The TR variations, instead, are based on Perlin noise [23] which ranges from 9.34 ms to 12 ms. These are only examples of how the parameters can be randomly varied. Other random patterns have been tested [19, 24] showing that MRF is not limited to one specified set of parameters.

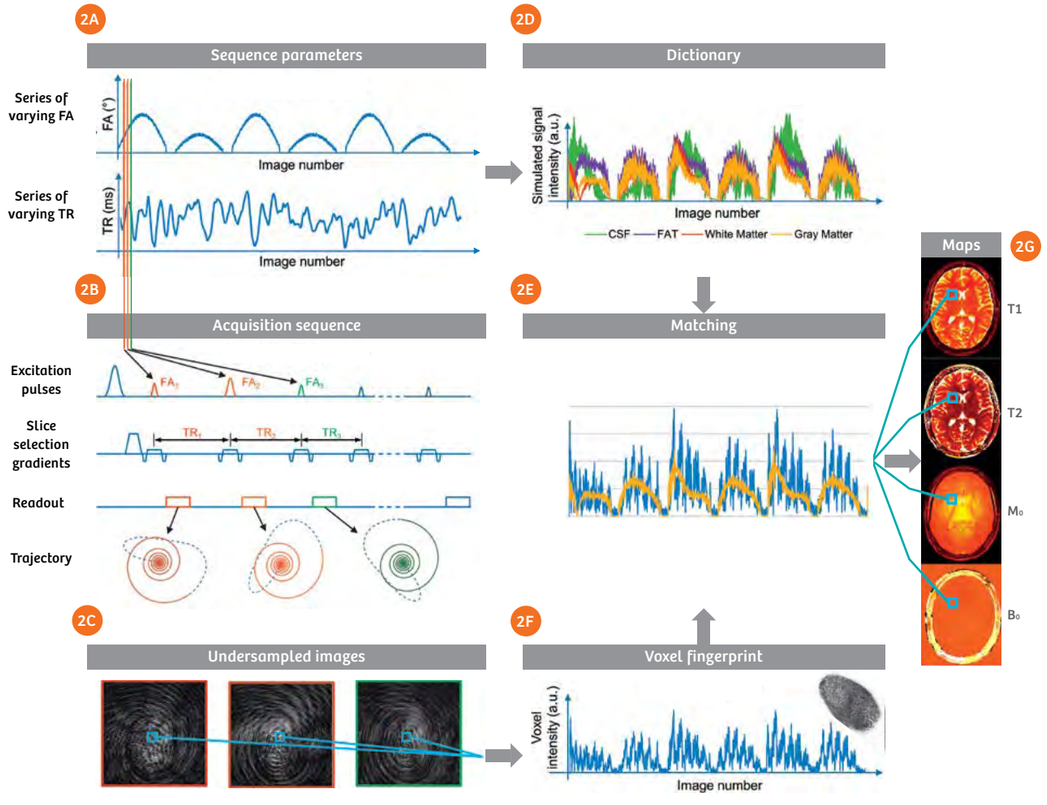

2 Flow chart of the MRF framework. **(2A)** Example of variable FA and TR used for a TrueFISP acquisition. **(2B)** Sequence diagram showing the excitation pulses, slice selection gradients, readout and *k*-space trajectory for each TR; **(2C)** Example of three undersampled images acquired in three different TR. **(2D)** Examples of four dictionary entries representing four main tissues: cerebrospinal fluid (CSF) (T1 = 5000 ms, T2 = 500 ms), fat (T1 = 400 ms, T2 = 53 ms), white matter (T1 = 850 ms, T2 = 50 ms), gray matter (T1 = 1300 ms, T2 = 85 ms); **(2E)** Matching of a voxel fingerprint with the closest entry in the dictionary, which allows to retrieve the tissue features represented by that voxel; **(2F)** intensity variation of a voxel across the undersampled images (fingerprint); **(2G)** parameter maps obtained repeating the matching process for each voxel.

Table 1: Ranges and step sizes used for the dictionary creation in case of a TrueFISP sequence (left) or FISP sequence (right).

	TrueFISP			FISP		
Parameter	**Min value**	**Max value**	**Step size**	**Min value**	**Max value**	**Step size**
T1 (ms)	100	2000	20	20	3000	10
	2000	5000	300	3000	5000	200
T2 (ms)	20	100	5	10	300	5
	100	200	10	300	500	50
	200	1900	200	500	900	200
Off-resonance (Hz)	-250	-190	20			
	-50	50	1			
	190	250	20			

An inversion recovery pulse is played out at the beginning of the acquisition sequence to enhance T1 differences between tissues (Fig. 2B). For each TR, a heavily undersampled image is reconstructed (Fig. 2C). It can be noticed how the base image series are not useful by themselves, but each voxel contains a signature fingerprint that will be used later on for the matching (identification). The total number of images acquired (also referred to as 'time points') can vary from acquisition to acquisition, ranging from 1000 [19] to 2500 [21] as function of the image resolution, the undersampling ratio, the matching approach used, etc. In most cases, we have used a variable-density spiral trajectory [25] designed to have a minimum time gradient and zero moment compensation for the acquisition. For example, we have successfully used a trajectory for a 128 x 128 matrix size that requires one interleaf to fully sample the center of k-space and 48 interleaves to fully sample the outer region of k-space. In the case of a 256 x 256 matrix, a trajectory requiring 24 interleaves to fully sample the inner region and 48 interleaves to fully sample the outer region can be used instead. Within each TR, one interleaf is acquired and used to reconstruct an image (or time point). The interleaf in the following TR is then rotated by 7.5° (≈ 2π/48) compared to the previous one.

The MRF framework is not only limited to a TrueFISP-based acquisition, but can be virtually applied to any kind of sequence. As an example, the MRF framework has been applied to a steady-state precession sequence (FISP) [20] to avoid the banding artifacts that can appear in wide field-of-view scans or in a high-field-strength scanner. The FISP sequence is still sensitive to T1 and T2 components but is less sensitive to off-resonance frequency. This is caused by the unbalanced gradient within every TR which results in the signal to be the sum of the spins within a voxel, making the sequence immune to banding artifacts. The unbalanced gradient, though, leads the FISP sequence to have a shorter transient state comparedto the TrueFISP. For this reason, the pseudorandom FA variation needs to be generated slightly differently than in the case of the TrueFISP sequence, in order to keep incoherence between the signal and under-sampling artifacts and to be able to identify the underlying fingerprint. The FA variation is thus generated based on sinusoidal variation in which the maximum reached FA for each half period randomly changes, ranging from 5° to 90°. The TR variation is always based on a Perlin noise pattern which ranges from 11.5 ms to 14 ms.

Dictionary generation

The dictionary can be seen as the heart of the MRF framework; it is the database that contains all physiologically possible signal evolutions that may be observed from the acquisition and that makes it possible to recognize the tissue within each voxel. MRF, like the forensic fingerprinting identification process, is effective only when a database large enough to contain all the potential candidates is available. In MRF, the dictionary is generated on a computer using algorithms that simulate the spin behavior during the acquisition

and thus predict the realistic signal evolution. In case of a TrueFISP-based acquisition, the Bloch equations [24] are used to simulate the various effects of the acquisition sequence on the spins, given a set of tissue parameters of interest (Fig. 2D). The information that can be retrieved with MRF is thus related to how and what physical effects are simulated. In the initial stages of development, MRF includes the simulation of T1, T2 and off-resonance, but more tissue features can be simulated and extracted, such as partial volume [19], diffusion [25] and perfusion [26].

A critical aspect of the dictionary is its size: to ensure the identification of any possible tissue parameter present in the acquisition, a wide combination of T1, T2 and off-resonance frequency need to be simulated. A standard TrueFISP dictionary with the parameter ranges as shown in Table 1 leads to a total of 363,624 possible combinations and includes the parameter values that are commonly found in the human body. The computation of such a dictionary for 1000 time points takes about 2.5 minutes on a standard desktop computer using a C++ based script and reaches 2.5 GB of memory size. A further increase in the dictionary size and/or resolution would increase the accuracy of the obtained maps at the expenses of an increase in the reconstruction time and memory requirements [19].

The simulation of a FISP acquisition is computed differently compared to the one described above. Since the FISP acquisition requires the simulation of multiple isochromats at different frequencies, which are then combined together, the simulation process through Bloch equations can be time consuming. An alternative time-efficient simulation is the extended phase graph (EPG) formalism [29], where a spin system affected by the sequence can be represented as discrete set of phase states, ideal to simulate the signal evolution of spins strongly dephased by unbalanced gradients. The FISP sequence is less sensitive to off-resonance effects compared to the TrueFISP acquisition, so the corresponding dictionary includes only the T1 and T2 relaxation times (Table 1) as the parameters of interest. This leads to 18,838 dictionary entries that can be computed in about 8 minutes on a standard desktop computer, and that generates a dictionary of about 1.2 GB.

Regardless of which sequence is used, the dictionary needs to be computed only once beforehand. It can then be used on the scanner, where it is used to reconstruct each MRF acquisition acquired with the sequence parameters that were simulated.

Matching

After the data acquisition, the fingerprint of each voxel (Fig. 2F) is normalized to unit norm and compared with all the normalized dictionary entries to identify the tissue in a given voxel (Fig. 2E). The simplest version of the matching is performed by taking the inner product between the voxel signal and each simulated fingerprint signal; the entry that returns the highest value is considered to be the one that best represents the tissue properties, and the respective T1, T2 and off-resonance values are assigned to the voxel (Fig. 2G). The relative spin density (M0) map, instead, is computed as the scaling factor between the acquired and the simulated fingerprints. The inner product has been demonstrated to be a robust operation and is able to correctly classify the tissues even in case of low SNR due to undersampling or even in the presence of a limited amount of motion artifacts [19].

This approach has also the potential of distinguishing different tissue components present within a single voxel (partial volume effect) thanks to the incoherence between different signal evolutions. The fingerprint (S) of a voxel containing different tissue can be seen as the weighted sum (w) of the different components (D): S = Dw. It has been shown [19] that,if the different components are known a priori, the appropriate inverse solution of the previous equation – (D)-1S = w, where (D)-1 represents the pseudoinverse of D – will provide the weight of each different tissue for each voxel [19,31].

The pattern recognition algorithm is performed on the scanner for every acquisition, so it is crucial for the clinical usefulness of the MR framework that this operation is performed in a reasonable time. While the direct matching using the inner product is accurate, it can take up to about 160 seconds to match a 2D slice of 128 x 128 base resolution, 1000 time points with a dictionary counting 363 624 entries. Similarly it takes about 30 seconds to match a 2D image with 256 x 256 voxels, 1000 time points and 18,838 dictionary entries for a FISP reconstruction.

The matching can be potentially accelerated by compressing the dictionary either in the time dimension or in the parameter combinations dimension, thus reducing the total number of comparisons that need to be performed. It has been shown [31] that the singular value decomposition (SVD) can be applied to compress the dictionary in the time dimension and reduce the matching time by a factor of 3.4 times for a TrueFISP dictionary and

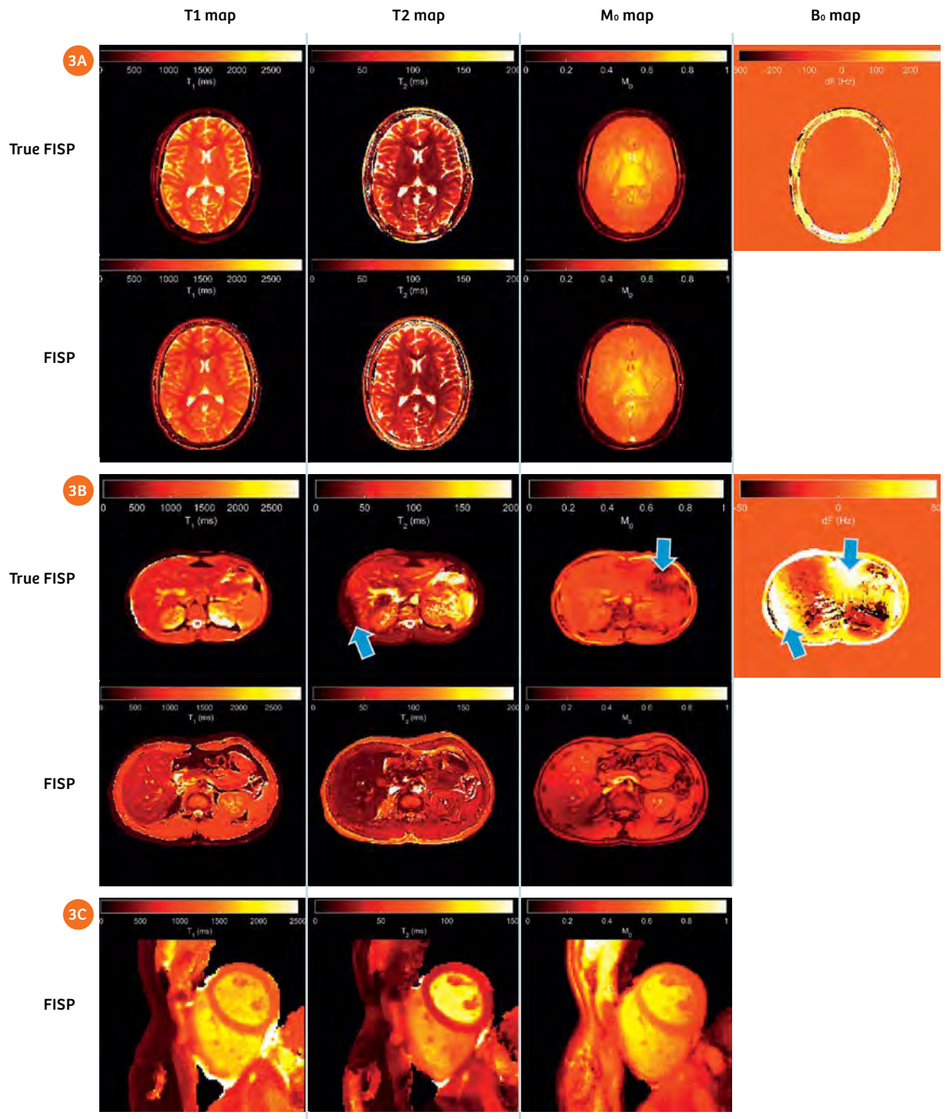

3 Examples of T1, T2, relative spin density (M_0) and off-resonance (B_0) maps acquired in two volunteers with a TrueFISP and a FISP acquisition. **(3A)** Single 2D slice of a head scan. **(3B)** Single 2D slice of an abdominal scan. **(3C)** Single 2D slice of diastolic cardiac scanin short axis view. In the T2 and B_0 map obtained from the TrueFISP acquisition, banding artifacts due to field inhomogeneity are visible (blue arrows).

Table 2: List of T1 and T2 relaxation times measured with MRF for different tissues and comparison with the value available in literature.

	T1 (ms)		T2 (ms)	
Tissue	**MRF**	**Literature**	**MRF**	**Literature**
White matter	685 ± 33 [19]	608–756 [34, 40–42]	65 ± 4 [19]	54–81 [34, 40–42]
	781 ± 61 [20]	788–898 [43]	65 ± 6 [20]	78–80 [43]
Gray matter	1180 ± 104 [19]	998–1304 [34, 40–42]	97 ± 5.9 [19]	78–98 [34, 40–42]
	1193 ± 65 [20]	1286–1393 [43]	109 ± 11 [20]	99–117 [43]
Cerebrospinal fluid	4880 ± 379 [19]	4103–5400 [34, 40–42]	550 ± 251 [19]	1800–2460 [34, 40–42]
Liver	745 ± 65 [21]	809 ± 71 [44]	31 ± 6 [21]	34 ± 4 [44]
Kidney medulla	1702 ± 205 [21]	1545 ± 142 [44]	60 ± 21 [21]	81 ± 8 [44]
Kidney cortex	1314 ± 77 [21]	1142 ± 154 [44]	47 ± 10 [21]	76 ± 7 [44]
Skeletal muscle	1100 ± 59 [21]	1017 ± 78 [45]	44 ± 9 [21]	50 ± 4 [46]
Fat	253 ± 42 [21]	343 ± 37 [45]	77 ± 16 [21]	68 ± 4 [44]

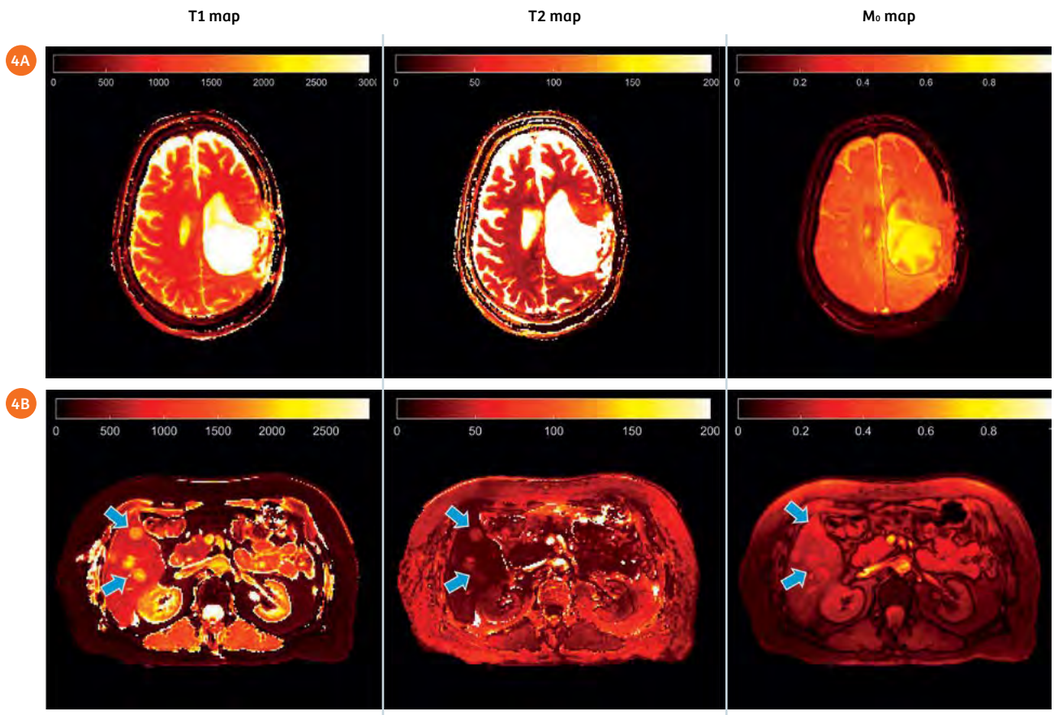

4 Example of patient results. Quantitative T1, T2 and relative spin density (M_0) maps obtained using the FISP protocol for brain [16] and abdomen acquisitions [20]. **(4A)** Maps of a patient with a brain tumor; **(4B)** 69-year-old patient with metastatic breast cancer. The metastasis (blue arrows) presents an increase in all tissue parameters, compared to the surrounding tissues.

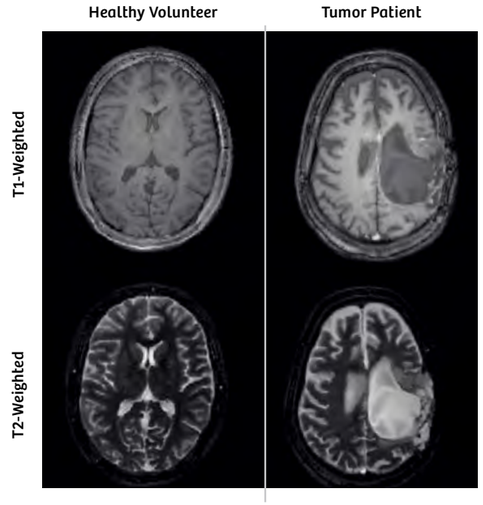

5 Synthetic generation of conventional images. Example of T1-weighted and T2-weighed images from a healthy volunteer and a patient with brain tumor, reconstructed starting from the T1, T2 and M_0 maps obtained from the FISP MRF maps of Figure 3 and 4.

up to a factor of 4.8 times for a FISP dictionary. The SVD-based dictionary compression has less than 2% of reduction in the accuracy of the estimated parameters. In this approach, the dictionary is projected into a subspace of lower dimension spanned by the first 25-200 singular vectors obtained from the SVD. The acquired fingerprint is projected onto the same subspace, and the matching is performed using the projected signal and the compressed dictionary. This framework reduces the number of calculations, thus reducing the final computation time despite the added operation of data projection on the subspace.

An alternative approach for reducing computational time for matching is by reducing the parameter combination dimension. A fast group matching algorithm [32] has been developed, where dictionary entries that have strong correlations are grouped together and a new signal that best represents the group is generated. The matching is thus subdivided in two steps; at first the acquired fingerprint is matched with the representing signal of each group, and only groups that return the highest correlation are kept in consideration. Then matching is used to find the best fit between the fingerprint and the remaining dictionary entries for the assignment of the parameters. This algorithm reduces the matching computation speed of one order of magnitude compared to the SVD compression and two orders of magnitude compared to the direct matching with no significant loss in the quality of the match. Techniques such as this make it feasible to implement MRF in a clinical manner.

Undersampling and motion

In MRF, the obtained parameter maps are the result of a pattern recognition algorithm as opposed to conventional reconstruction techniques, which allows MRF to be more robust to various image artifacts. This effect is strengthened by the random variation of FA, TR and trajectory which not only aim at differentiating the fingerprints from different tissues, but also aim at increasing the incoherence between the fingerprints. The matching can recognize the underlying signal evolutions even in low signal-to-noise or accelerated conditions as long as the noise or undersampling artifacts are incoherent with the signal. Additionally, just like in forensic fingerprinting, a correct identification is possibleeven with the use of blurry or partial fingerprints, the MR counterpart is also capable of providing parametric maps without any residual motion artifacts in case of a fingerprint partially corrupted by motion [19].

Volunteer acquisitions

MRF acquisitions have been tested in volunteers in 2D brain, abdominal, and cardiac scans. All in vivo experiments were performed under the Institutional Review Board guidelines and each subject signed informed consent prior to the data acquisition. The scans were performed on a 3T MAGNETOM Skyra system with a 20-channel head coil or a phased array 18-channel body coil plus spine coil. For the brain scans, the variable acquisition parameters (FA and TR) were set as described above and 3000 time points were acquired; the FOV was 300 x 300 mm, the slice thickness was 5 mm and the matrix size was 256 x 256. The acquisition time was 38 s for a 2D TrueFISP slice and 41 s for the FISP acquisition.

The cardiac MRF scans were acquired using a modified pulse sequence with ECG triggering to restrict data collection to mid-diastole [35]. A total of 768 time points were acquired over a 16-heartbeats breath-hold using a scan window of 250 ms with FOV 300 x 300 mm, slice thickness 8 mm, and matrix size 192 x 192 [35]. For the abdominal and cardiac imaging, the trajectory and acquisition protocols were adapted as described in references [21, 35] respectively. The dictionaries were computed as described above and SVD based matching was used for parameter estimation.

Figure 3 shows the maps obtained from volunteer scans in the brain (Fig. 3A), abdomen (Fig. 3B), and heart (Fig. 3C). Both FISP and TrueFISP MRF provide comparable high resolution multiparametric tissue maps. The FISP acquisition has the drawback of not providing the off-resonance information, but it has the advantage of being insensitive to banding artifacts. Therefore, FISP MRF is advantageous for body imaging, where the sharp susceptibility transitions and the need for a large field-of-view would lead to banding artifacts with a balanced SSFP acquisition.

The values obtained with MRF maps are generally in good agreement with the standard mapping techniques [20] and with the literature value of tissue parameters [19, 24], as shown in Table 2. It can be noticed, though, that there is a mismatch in the values of CSF and fat. The CSF T2 discrepancy between MRF and literature value can be explained by through-plane motion of the fluid that was not taken into account in the dictionary simulation [19]. The fat T1 discrepancy, instead, is mainly due to the intentionally low T1 dictionary resolution (100 ms) for the range 100–600 ms used for that study [21].

The MRF efficiency is designed to be extremely high in comparison to traditional mapping approaches [19–21] as well as rapid combined T1 and T2 mapping methods like DESPOT [19, 36]. The planned high efficiency and accuracy of the MRF framework may allow parametric mapping to be performed in a clinically relevant acquisition time without loss of information. In this way, multiparametric mapping can be translated to the clinical environment.

Patient acquisitions

The MRF framework has also been successfully tested on patients. Figure 4 shows the feasibility of brain and abdominal MRF in a clinical environment. Data were acquired with the previously described FISP acquisitions on patients with a brain tumor and breast cancer metastatic to the liver (Fig. 4). Longer T1 relaxation time can be observed in the metastatic lesions compared to the surrounding tissues. It has been shown in six patients with metastatic adenocarcinoma that the mean T1 and T2 values in the metastatic adenocarcinoma were on the order of 1673 ± 331 ms and 43 ± 13 ms, respectively. Those values are significantly higher than the ones of the surrounding tissues (840 ± 113 ms and 28 ± 3 ms, respectively) [21]. Recent studies investigate the possibility of predicting response of tumor to treatment using tissue relaxation times; e.g. the T1 relaxation time can potentially be an indicator of chemotherapy response [35, 36]. Fast multiparametric mapping can thus open the path to the creation of a multiproperty space that might allow a deeper characterization and understanding of the conditions and evolutions of determined pathologies.

Synthetic weighted images

It is also possible to retrospectively calculate and estimate 'standard' weighted images from the multiple parameter maps obtained from an MRF scan. Figure 5 shows an example of T1-weighted and T2-weighted acquisition calculated from the FISP T1 and T2 maps of the volunteer and patient head scan shown above.

Conclusions

Magnetic resonance fingerprinting is a novel framework for MRI, where the pulse sequence design is not aimed at acquiring images, but at directly measuring tissue properties. In MRF, the sequence generates unique signal evolutions, or fingerprints, for each different tissue and matches it with a set of theoretical signal evolutions to measure several tissue properties within a single acquisition. Once the tissue features are measured, it is possible to directly know several tissue-specific properties that can provide information. In this work, only two MRF implementations have been shown, but the MRF framework has the potential to allow more freedom in the sequence design compared to standard MRI sequences, since the parameters can be randomly varied. Thanks to this freedom, a whole new world of possibilities of acquisition and reconstruction strategies that can probe and measure new features have been opened up for our community to explore.

This paper focused on T1, T2, M0 and B0 characterization, but the MRF is not limited to that. Several work are being performed to exploit the potential of MRF including: diffusion [27], arterial spin labeling [28, 42, 43] and chemical exchange [44].

The pattern recognition nature of MRF makes the acquisition robust to artifacts like undersampling and motion, yielding high efficiency, accuracy and robustness that are critical for the successful integration of a multiparametric mapping technique into the clinical environment. Moreover, the increased efficiency and robustness to artifacts compared to standard MR imaging approaches could potentially reduce the time and thus the costs of MRI exams, making it more affordable and more competitive in comparison to other imaging modalities.

References

[1] Larsson H, Frederiksen J. Assessment of demyelination, edema, and gliosis by in vivo determination of T1 and T2 in the brain of patients with acute attack of multiple sclerosis. Magn Reson Med [Internet]. 1989;348:337–48. Available from: http://onlinelibrary.wiley.com/doi/10.1002/mrm.1910110308/abstract

[2] Usman AA, Taimen K, Wasielewski M, et al. Cardiac magnetic resonance T2 mapping in the monitoring and follow-up of acute cardiac transplant rejection: a pilot study. Circ Cardiovasc Imaging [Internet]. 2012;5(6):782–90. Available from: http://www.ncbi.nlm.nih.gov/pubmed/23071145

[3] Payne AR, Berry C, Kellman P, et al. Bright-blood T 2-weighted MRI has high diagnostic accuracy for myocardial hemorrhage in myocardial infarction a preclinical validation study in swine. Circ Cardiovasc Imaging. 2011;4(6):738–45.

[4] Van Heeswijk RB, Feliciano H, Bongard C, et al. Free-breathing 3 T magnetic resonance T2-mapping of the heart. JACC Cardiovasc Imaging [Internet]. 2012 Dec;5(12):1231–9. Available from: http://www.ncbi.nlm.nih.gov/pubmed/23236973

[8] Look DC, Locker DR. Time saving in measurement of NMR and EPR relaxation times. Rev Sci Instrum. 1970;41(2):250–1.

[9] Huang TY, Liu YJ, Stemmer A, Poncelet BP. T2 measurement of the human myocardium using a T 2-prepared transient-state trueFISP sequence. Magn Reson Med. 2007;57:960–6.

[10] Mehta BB, Chen X, Bilchick KC, Salerno M, Epstein FH. Accelerated and navigator-gated look-locker imaging for cardiac T1 estimation (ANGIE): Development and application to T1 mapping of the right ventricle. Magn Reson Med. 2015;73(1):150–60.

[11] Zhu DC, Penn RD. Full-brain T1 mapping through inversion recovery fast spin echo imaging with time-efficient slice ordering. Magn Reson Med. 2005;54(3):725–31.

[12] Cheng H-LM, Wright GA. Rapid High-Resolution T1 Mapping by Variable Flip Angles: Accurate and Precise Measurements in the Presence of Radiofrequency Field Inhomogeneity. Magn Reson Med. 2006;55:566–76.

[13] Doneva M, Börnert P, Eggers H, Stehning C, Sénégas J, Mertins A. Compressed sensing reconstruction for magnetic resonance parameter mapping. Magn Reson Med. 2010;64(4):1114–20.

[14]Deoni SCL, Rutt BK, Peters TM. Rapid combined T1 and T2 mapping using gradient recalled acquisition in the steady state. Magn Reson Med. 2003;49(3):515–26.

[15]Blume U, Lockie T, Stehning C, et al. Interleaved T1 and T2 relaxation time mapping for cardiac applications. J Magn Reson Imaging. 2009;29:480–7.

[16]Warntjes JBM, Dahlqvist O, Lundberg P. Novel method for rapid, simultaneous T1, T2*, and proton density quantification. Magn Reson Med. 2007;57(3):528–37.

[17]Schmitt P, Griswold MA, Jakob PM, et al. Inversion recovery TrueFISP: quantification of T(1), T(2), and spin density. Magn Reson Med. 2004;51(4):661–7.

[18]Ehses P, Seiberlich N, Ma D, et al. IR TrueFISP with a golden-ratio-based radial readout: Fast quantification of T1, T2, and proton density. Magn Reson Med. 2013;69(1):71–81.

[19]Ma D, Gulani V, Liu K, et al. Magnetic resonance fingerprinting. Nature [Internet]. 2013;495(7440):187–92.

[20]Jiang Y, Ma D, Seiberlich N, Gulani V, Griswold M a. MR fingerprinting using fast imaging with steady state precession (FISP) with spiral readout. Magn Reson Med [Internet]. 2014;. Available from: http://www.ncbi.nlm.nih.gov/pubmed/25491018

[21]Chen Y, Jiang Y, Pahva Shivani, et al. MR Fingerprinting for Rapid Quantitative Abdominal Imaging. Radiology. 2016;000(0):1–9.

[22]Schmitt P, Griswold MA, Gulani V, Haase A, Flentje M, Jakob PM. A simple geometrical description of the TrueFISP ideal transient and steady-state signal. Magn Reson Med. 2006;55(1):177–86.

[23]Perlin K. An image synthesizer. ACM SIGGRAPH Comput Graph. 1985;19(3):287–96.

[24]Ma D, Pierre EY, Jiang Y, et al. Music-based magnetic resonance fingerprinting to improve patient comfort during MRI examinations. Magn Reson Med [Internet]. 2015; Available from: http://doi.wiley.com/10.1002/mrm.25818

[25]Lee JH, Hargreaves B a., Hu BS, Nishimura DG. Fast 3D Imaging Using Variable-Density Spiral Trajectories with Applications to Limb Perfusion. Magn Reson Med. 2003;50(6):1276–85.

[26]Bloch F. Nuclear induction. Phys Rev. 1946;70:460–85.

[27]Jiang Y, Wright KL, Seiberlich N, Gulani V, Griswold MA. Simultaneous T1, T2, diffusion and proton density quantification with MR fingerprinting. In: In proceedings of the 22nd annual meeting of ISMRM meeting & exhibition in Milan, Italy. 2014. p. 28.

[28]Wright KL, Ma D, Jiang Y, Gulani V, Griswold MA, Luis H-G. Theoretical framework for MR fingerprinting with ASL: simultaneous quantification of CBF, transit time, and T1. In: In proceedings of the 22nd annual meeting of ISMRM meeting & exhibition in Milan, Italy. 2014. p. 417.

[29]Weigel M, Schwenk S, Kiselev VG, Scheffler K, Hennig J. Extended phase graphs with anisotropic diffusion. J Magn Reson. 2010;205(2):276–85.

[30]Deshmane AV, Ma D, Jiang Y, et al. Validation of Tissue Characterization in Mixed Voxels Using MR Fingerprinting. In: In proceedings of the 22nd annual meeting of ISMRM meeting & exhibition in Milan, Italy. 2014. p. 0094.

[31]McGivney D, Pierre E, Ma D, et al. SVD Compression for Magnetic Resonance Fingerprinting in the Time Domain. IEEE Trans Med Imaging. 2014;0062(12):1–13.

[32]Cauley SF, Setsompop K, Ma D, et al. Fast group matching for MR fingerprinting reconstruction. Magn Reson Med [Internet]. 2014;00. Available from: http://dx.doi.org/10.1002/mrm.25439

[33]Hamilton JI, Jiang Y, Chen Y, et al. MRF for Rapid Quantification of Myocardial T1, T2, and Proton Spin Density. Magn Reson Med. 2016;In press.

[34]Deoni SCL, Peters TM, Rutt BK. High-resolution T1 and T2 mapping of the brain in a clinically acceptable time with DESPOT1 and DESPOT2. Magn Reson Med. 2005;53(1):237–41.

[35]Jamin Y, Tucker ER, Poon ES, et al. Evaluation of Clinically Translatable MR Imaging Biomarkers of Therapeutic Response in the TH- MYCN Transgenic Mouse Model of Neuroblastoma. Radiology. 2012.

[36]Weidensteiner C, Allegrini PR, Sticker-Jantscheff M, Romanet V, Ferretti S, McSheehy PM. Tumour T1 changes in vivo are highly predictive of response to chemotherapy and reflect the number of viable tumour cells - a preclinical MR study in mice. BMC Cancer. 2014;14(1):88.

[37]Christen T, Pannetier NA, Ni WW, et al. MR vascular fingerprinting: A new approach to compute cerebral blood volume, mean vessel radius, and oxygenation maps in the human brain. Neuroimage [Internet]. 2014 Apr 1 [cited 2015 Nov 19];89:262–70. Available from: http://www.pubmedcentral.nih.gov/articlerender.fcgi?artid=3940168&tool=pmcentrez&rendertype=abstract

[38]Pan S, Mao D, Peiying L, Yang L, Babu W, Hanzhang L. Arterial Spin Labeling without control/label pairing and post-labeling delay: an MR fingerprinting implementation. In: In proceedings of the 23rd annual meeting of ISMRM meeting & exhibition in Toronto, Canada. 2015. p. 0276.

[39]Hamilton JI, Deshmane AV, Stephanie H, Griswold MA, Seiberlich N. Magnetic Resonance Fingerprinting with Chemical Exchange (MRF-X) for Quantification of Subvoxel T1, T2, Volume Fraction, and Exchange Rate. In: In proceedings of the 23rd annual meeting of ISMRM meeting & exhibition in Toronto, Canada. 2015. p. 0329.

[40]Vymazal J, Righini A, Brooks RA, et al. T1 and T2 in the Brain of Healthy Subjects, Patients with Parkinson Disease, and Patients with Multiple System Atrophy: Relation to Iron Content. Radiology. 1999;211(2):489–95.

[41]Whittall KP, MacKay AL, Graeb DA, Nugent RA, Li DK, Paty DW. In vivo measurement of T2 distributions and water contents in normal human brain. Magn Reson Med. 1997;37(1):34–43.

[42]Poon CS, Henkelman RM. Practical T2 quantitation for clinical applications. J Magn Reson Imaging. 1992;2(5):541–53.

[43]Wansapura JP, Holland SK, Dunn RS, Ball WS. NMR relaxation times in the human brain at 3.0 tesla. J Magn Reson Imaging. 1999;9(4):531–8.

[44]de Bazelaire CM, Duhamel GD, Rofsky NM, Alsop DC. MR imaging relaxation times of abdominal and pelvic tissues measured in vivo at 3.0 T: preliminary results. Radiology. 2004;230(3):652–9.

[45]Chen Y, Lee GR, Aandal G, et al. Rapid volumetric t1 mapping of the abdomen using three-dimensional through-time spiral GRAPPA. Magnetic Resonance in Medicine. 2016 Apr;75(4):1457-65.

[46]Stanisz GJ, Odrobina EE, Pun J, et al. T1, T2 relaxation and magnetization transfer in tissue at 3T. Magn Reson Med [Internet]. 2005/08/09 ed. 2005;54(3):507–12. Available from: http://www.ncbi.nlm.nih.gov/pubmed/16086319.

Contact
Vikas Gulani, M.D.
vxg46@case.edu

On account of certain regional limitations of sales rights and service availability, we cannot guarantee that all products included in this brochure are available through the Siemens sales organization worldwide. Availability and packaging may vary by country and is subject to change without prior notice. Some/All of the features and products described herein may not be available in the United States.

The information in this document contains general technical descriptions of specifications and options as well as standard and optional features, which do not always have to be present in individual cases.

Siemens reserves the right to modify the design, packaging, specifications, and options described herein without prior notice. For the most current information, please contact your local sales representative from Siemens.

Note: Any technical data contained in this document may vary within defined tolerances. Original images always lose a certain amount of detail when reproduced.

Siemens Healthineers Headquarters
Siemens Healthcare GmbH
Henkestr. 127
91052 Erlangen, Germany
Phone: +49 9131 84-0
siemens-healthineers.com

Local Contact Information
Siemens Medical Solutions USA, Inc.
40 Liberty Boulevard
Malvern, PA 19355-9998, USA
Phone: 1-888-826-9702
usa.siemens.com/healthineers

Order No. A91DI-MR-171342-P1-4A00 · Printed in USA · 11-2017 ·